



UNIVERSITÀ DEGLI STUDI DI PALERMO

Corso di Dottorato in Ingegneria dell'Innovazione Tecnologica

Dipartimento di Ingegneria

ING-IND/16 - Tecnologie e Sistemi di lavorazione

**LIGHTWEIGHT ALLOYS RECYCLING AND PROCESSING
THROUGH INNOVATIVE FRICTION BASED
DIRECT TECHNOLOGIES**

**IL DOTTORE
ING. DARIO BAFFARI**

**IL COORDINATORE
CHIA.MO PROF. ANTONIO CHELLA**

**IL TUTOR
CHIA.MO PROF. LIVAN FRATINI**

**CICLO XXXI
ANNO CONSEGUIMENTO TITOLO 2017-2018**

Table of contents

Table of contents	2
Acknowledgements	5
Abstract	6
List of abbreviations	7
1. Introduction	9
1.1 Secondary production: challenges and opportunities.....	9
1.2 Dissertation structure	14
2. Metal scraps recycling: state of the art	18
2.1 Conventional processes.....	18
2.1.1 Scrap Preparation.....	19
2.1.2 Smelting and Refining	21
2.1.3 Recycled alloys quality	23
2.2 Innovative direct processes.....	26
2.2.1 Hot Extrusion.....	27
2.2.2 Equal channel angular pressing (ECAP).....	30
2.2.3 Cyclic Extrusion Compression (CEC)	32
2.2.4 Screw extrusion.....	33
2.2.5 High Press Torsion (HPT)	34
2.2.6 Powder Metallurgy (P/M)	35
2.2.7 Spark Plasma Sintering (SPS).....	36
2.3 Summary and perspective of solid-state recycling	37
3. Friction Stir Extrusion	39
3.1 Historical background and process description.....	39
3.1.1 State of the art	40
3.1.2 Process parameters	43
3.2 Experimental campaigns.....	45
3.2.1 Experimental setups	45

3.2.2	<i>Materials</i>	48
3.3	Numerical FEM model	49
3.3.1	<i>Governing Equations</i>	49
3.3.2	<i>Model setup</i>	51
3.3.3	<i>Model calibration</i>	55
3.4	Process mechanics	57
3.4.1	<i>Extrudate quality</i>	58
3.4.2	<i>Extrusion rate</i>	60
3.4.3	<i>Extrusion temperature</i>	63
3.4.4	<i>Material flow tracking</i>	64
3.5	Extrudates integrity and microstructure prediction	71
3.5.1	<i>FEM model results</i>	71
3.5.2	<i>Microstructure prediction</i>	75
3.5.3	<i>Extrudates integrity prediction</i>	77
3.6	Material properties influence	82
3.6.1	<i>Extrudates quality</i>	83
3.6.2	<i>Torque analysis</i>	88
3.6.3	<i>Extrusion rate analysis</i>	89
3.7	MMC fabrication	92
3.8	Process Energy Demands.....	96
3.8.1	<i>System boundary and major assumptions</i>	96
3.8.2	<i>Life Cycle Inventory</i>	97
3.8.3	<i>Power measurements</i>	98
3.8.4	<i>Energy demands comparison</i>	99
3.9	FSE as a primary manufacturing process	102
3.10	Process development outlook	104
3.10.1	<i>Continuous machine design development</i>	104
4.	Friction Stir Consolidation	108
4.1	Historical background and process description.....	108
4.1.1	<i>Process parameters</i>	109
4.2	Experimental campaigns.....	110
4.2.1	<i>Experimental setup</i>	110
4.2.2	<i>Materials</i>	111

4.3	Process mechanics	112
4.4	Numerical FEM model	116
4.4.1	<i>Governing equations</i>	116
4.4.2	<i>Model setup and calibration</i>	116
4.5	Bonding Prediction	120
4.5.1	<i>FEM results</i>	120
4.5.2	<i>Bonding criteria</i>	122
4.6	Process energy demands	125
4.6.1	<i>System boundary and major assumptions</i>	125
4.6.2	<i>Life Cycle Inventory</i>	126
4.6.2	<i>Power measurements</i>	127
4.6.3	<i>Energy demands comparison</i>	128
5.	Conclusions	131
5.1	Summary	131
5.2	Outlook and future developments	134
	References	135
	Curriculum Vitae	147
	Publications List	148

Acknowledgements

This dissertation is the outcome of my research carried out during the last three years at the Department of Digital and Industrial Innovation of the University of Palermo. First, I would like to thank my advisor, prof. Livan Fratini, who supported me through my doctoral studies with his mentoring and guidance. I also gratefully thank prof. Anthony Reynolds, who hosted and helped me during my stay at the University of South Carolina. Thanks to all my colleagues and co-workers from the MTG and the USC-FSW groups that assisted and accompanied me in this journey. Finally, many thanks to my family and friends who always supported and encouraged me.

Abstract

In the last decades, the use of lightweight alloys has been spreading in almost any industrial field thanks to the relevant weight reduction allowed by the use of such materials. On the other hand, aluminium alloys are characterized by high-energy demands primary production cycles that are responsible for a relevant share of the global CO₂ emissions. In order to limit and reverse such phenomenon, putting in place strategies to keep the material in the circle over multiple life cycles is mandatory and the concepts of circular economy, closed loop society and industrial symbiosis are progressively gathering more and more pace. Nevertheless, metal scraps are often mainly composed of chips resulting from machining operations and sheet metal coming from trimming after forming processes. This kind of wastes is between the most difficult kind of scraps to be recycled as they are characterized by high surface/volume ratio and they are usually oxidized and covered by different types of contaminants. Due to these features, conventional melting recycling technologies may lead to different drawbacks the overall energy efficiency is quite low and, more importantly, permanent material losses occur during remelting because of oxidation. In order to overcome such issue, researchers started investigating solid-state recycling approaches; in fact, by avoiding the remelting step, both energy and material can be saved. In this dissertation, the Friction Stir Extrusion and Friction Stir Consolidation processes capabilities for lightweight alloys recycling and processing are investigated with a particular focus on the influence of the process parameters on the mechanical properties of the processed materials. Numerical models to predict the processes evolutions are described and the environmental impact of these technologies are evaluated.

List of abbreviations

AA	Aluminium alloys
AM	Additive Manufacturing
CDRX	Continuous Dynamic Recrystallization
CEC	Cyclic Extrusion Compression
d	Extrudate diameter
D	Die external diameter
DRX	Dynamic Recrystallization
ECAP	Equal Channel Angular Pressing
F	Extrusion force
FEM	Finite Elements Method
FSC	Friction Stir Consolidation
FSE	Friction Stir Extrusion
FSP	Friction Stir Processing
GHG	Greenhouse gases
HPT	High Press Torsion
iECAP	Integrated extrusion and Equal Channel Angular Pressing
LCA	Life Cycle Assessment
LCI	Life Cycle Inventory

MMC	Metal Matrix Composites
p	Reinforce percentage in MMC
P/M	Powder Metallurgy
R	Die rotational speed
r	Extrusion ratio
SPD	Severe Plastic Deformation
SPS	Spark Plasma Sintering
SSR	Solid State Recycling
t	Consolidation time
WAAM	Wire Arc Additive Manufacturing
Z	Zener-Hollomon parameter

1. Introduction

1.1 Secondary production: challenges and opportunities

The development of environmentally sustainable manufacturing processes is becoming one of the main challenges of the modern age. In particular, many international agreements, such as the Kyoto Protocol, are binding the signing countries to reduce gradually the greenhouse gas emissions in the next years. It is worth noticing that a relevant share of the annual global greenhouse gases (GHG) emissions is caused by raw materials production. Worrell et al. [1] state that material production activities cause about 25% of global CO₂ emissions. Such environmental burden is actually dominated by only few materials: steel, cement, paper, aluminium alloys, and aggregated plastics [2]. Furthermore, Figure 1.1 shows how these materials are collectively responsible for over 80% of the annual energy consumption.

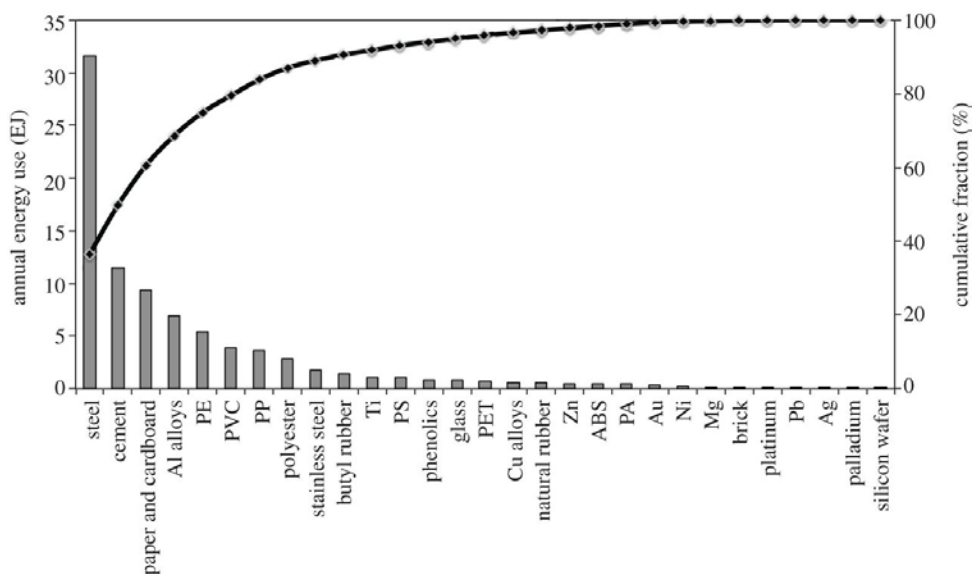


Figure 1.1. Annual primary energy used for the production of 29 materials worldwide, cumulative scale on the right (Source: [3]).

Gutowski et al. [2] state that, from 2005 to 2050, the demand for aluminium is expected to grow by a factor of between 2.6 and 3.5, while the demand for steel between 1.8 and 2.2 (Figure 1.2). In order to limit and reverse such phenomenon, putting in place strategies to keep the material in the circle over multiple life cycles is mandatory. In particular, longer life, intense use, product repair and upgrades, modularity, remanufacturing, industrial symbiosis, and open/closed loop recycling are some of the strategies that have to be put in place to reduce the environmental impact of raw material production. The whole concept of a circular economy is progressively gathering more and more pace [4].

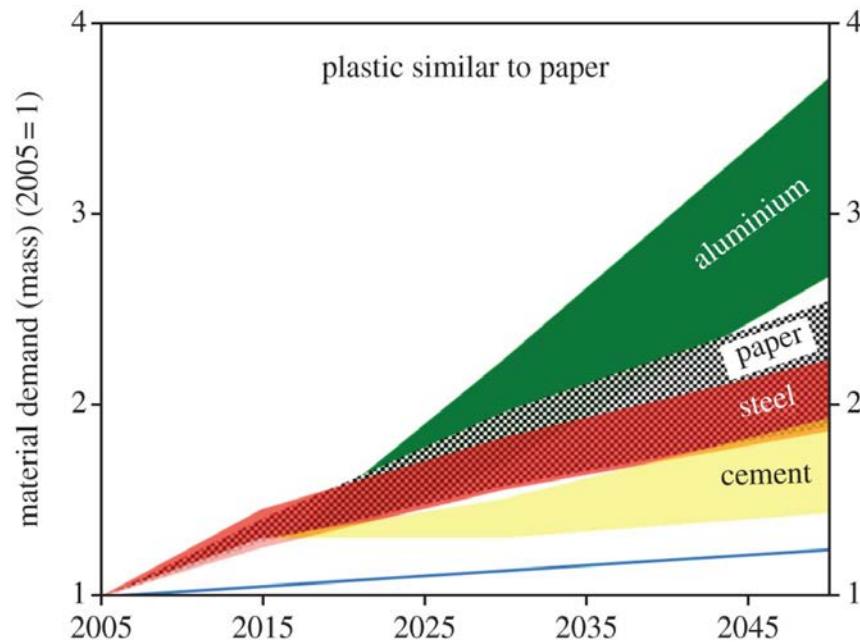


Figure 1.2. The range of future demand for aluminium, paper, steel, plastic and cement (Source [2]).

Currently, conventional recycling is the most applied technique for metals since it offers many technical and environmental advantages with respect to other strategies. As far as lightweight alloys are concerned, primary energy savings as high as 90% can be obtained [5], making the recycling even more convenient also on the energy usage point of view (Figure 1.3). Recycling of lightweight alloys has, hence, far-reaching economic, ecological, and social implications that many industrialized countries cannot face with the limited domestic primary productions, especially considering the growth of the demands of such materials. Unfortunately,

the conventional remelting based recycling routes for lightweight alloys are still energy-intensive. As a matter of facts, the overall energy efficiency is quite low and permanent material losses may occur. Moreover, metal scraps are often composed of chips resulting from machining operations and sheet metal coming from trimming after forming processes (Figure 1.4). This variety of wastes are classified as “process scrap” or “new scrap” by the European standards [6] and are composed of surplus material coming from production or fabrication of metal goods up to the point they are sold to the consumers. This kind of wastes is among the most difficult to be recycled as they are characterized by high surface/volume ratio and they are usually covered by oxides formations or other contaminants. Due to these peculiar features, the permanent material losses for light-gauge scraps processed through remelting can be as high as 15-20% [7]. Conventional recycling techniques usually also require several intermediate operations as well as high energy demand (cleaning, drying, chopping, compacting, etc.) that concur to reduce the process overall efficiency. Actually, also “old scraps” (i.e. the end of life scraps, see Figure 1.4b)) coming to the recollection of used products can be converted into a similar state as the processed scrap with proper cleaning, segregation and chopping stages.

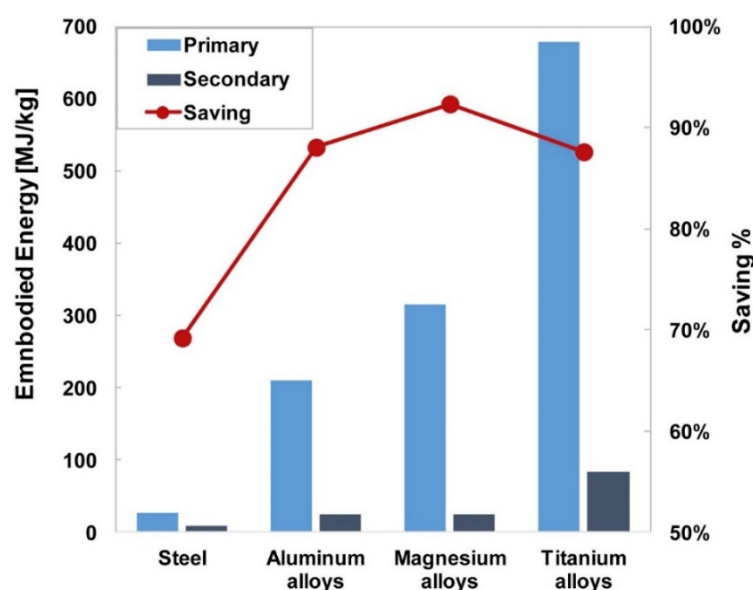


Figure 1.3. Embodied energy comparison for primary and secondary production of different metals alloys, savings scale on the right (Source: [5]).

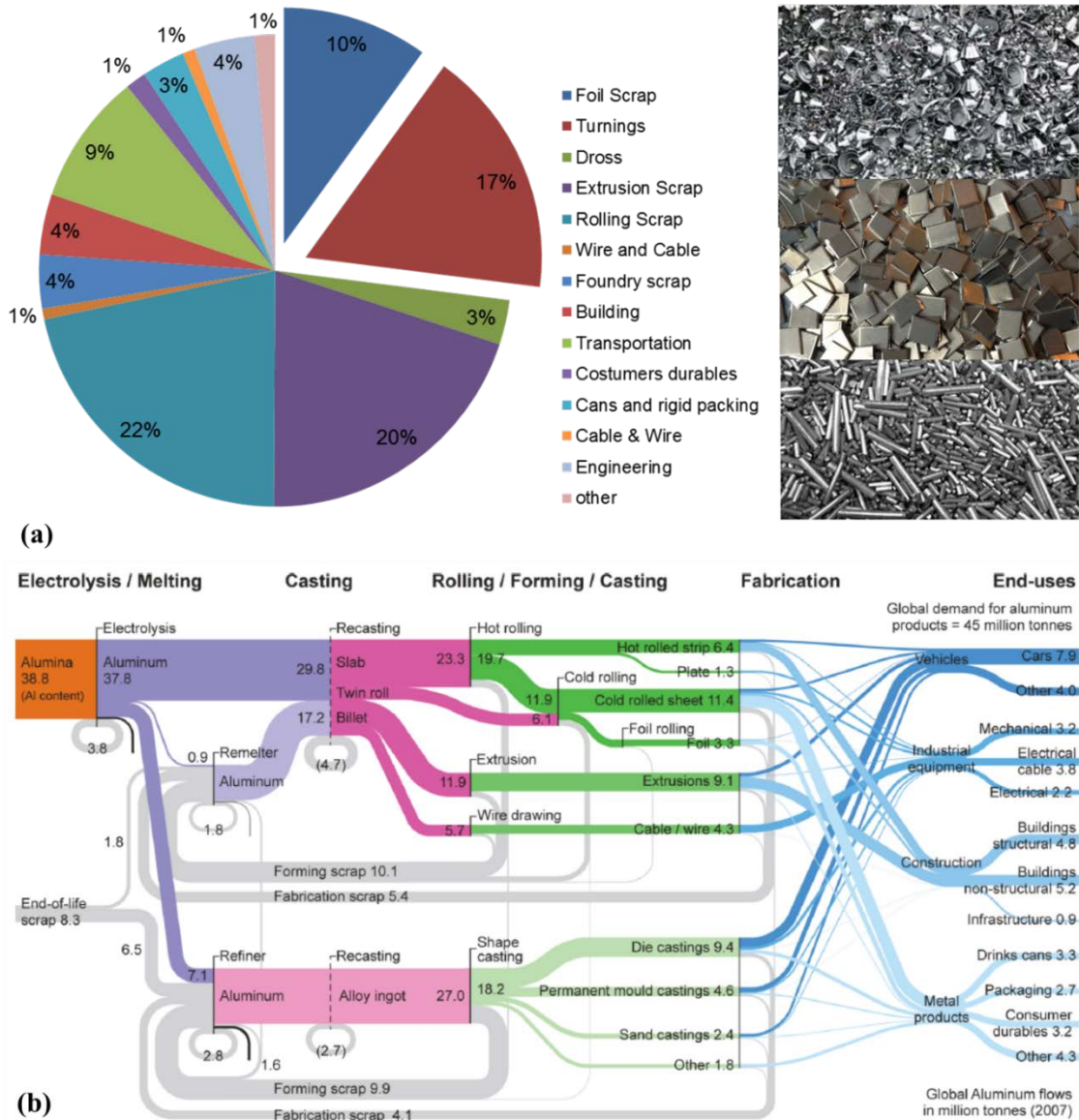


Figure 1.4. (a) Metal scrap sources and (b) Sankey diagram for aluminium flows (Adapted from:[3]).

In order to overcome such issues, many researchers in the last years started investigating solid-state recycling approaches. Avoiding the remelting step alone during the recycling route both energy and material can be saved enhancing the convenience of the secondary production of raw material under any point of view. Due to the limited intermediate operations needed to complete the material processing, these recycling processes are often known as “direct conversion methods”. Samuel [8] state that of one of the early proposed direct conversion route allowed to recycle almost 96% of the processed scrap with very low losses (Figure 1.5).

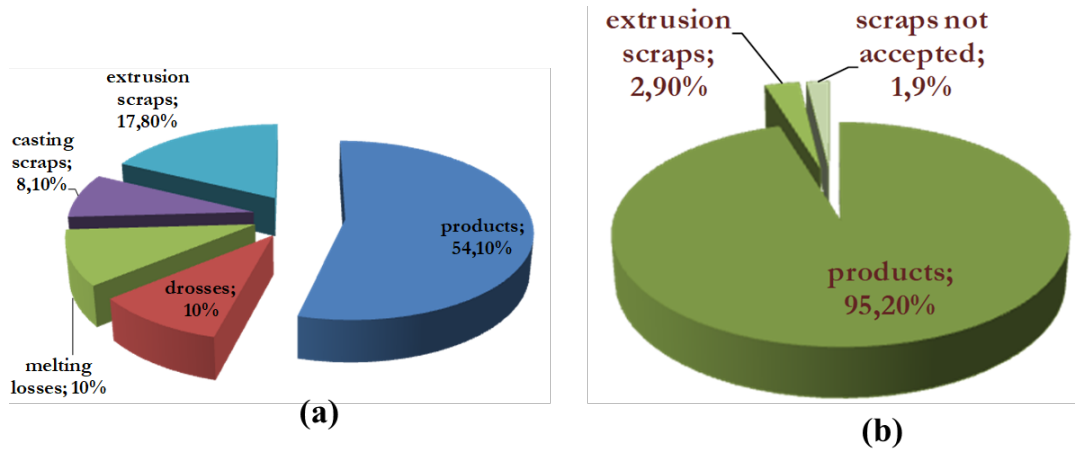


Figure 1.5. Comparison between (a) conventional recycling process and (b) solid state recycling processes (Adapted from [8]).

In the next pages, the main conventional and innovative technologies to recycle metal scrap are described to hence focus on the Friction Stir Extrusion (FSE) and the Friction Stir Consolidation (FSC) processes. These techniques belong to the Friction Stir Processing technologies and are among the newest solid-state recycling process being investigated. Many experimental campaigns have been carried out using both processes in order to investigate the influence of the main process parameters and of the material being processed on the products quality. Numerical models have been implemented to give better insight into the processes mechanics and to predict defect formation. Finally, the energetic efficiency of the processes with respect to other recycling route has been investigated using LCI techniques.

1.2 Dissertation structure

This paragraph provide an overview of the general structure this dissertation in order to provide the links between the different sections and their respective contents. This dissertation is composed by five main chapter and each of them is further divided into paragraphs and subparagraphs numbered accordingly. He topics covered by each of these sections is briefly described in the following lines.

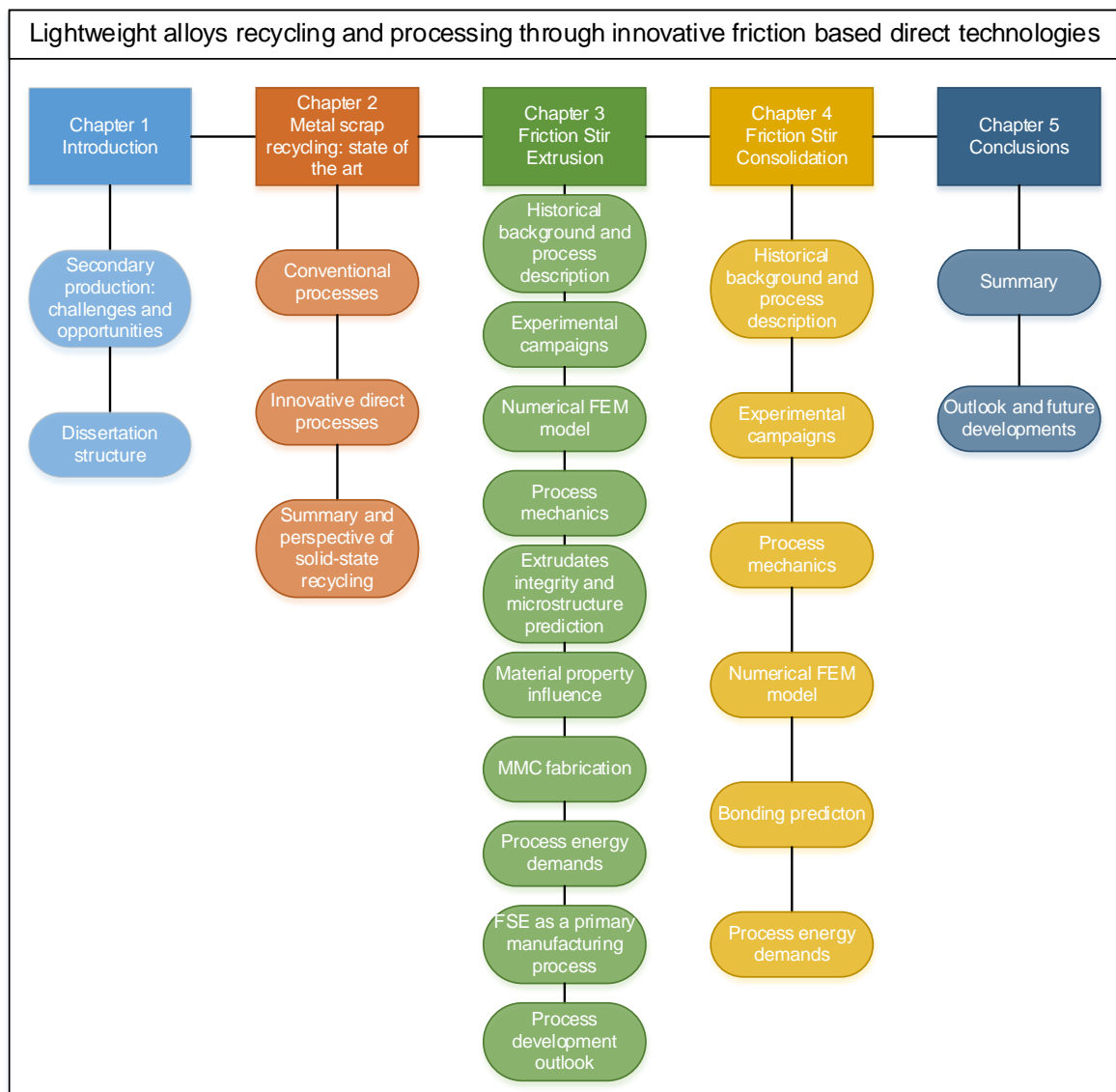


Figure 1.5. Dissertation structure scheme.

Chapter 1, namely “Introduction”, deals with the general introduction to the metal recycling issues and capabilities, with particular focus on the lightweight alloys. It also contains the dissertation structure summary.

Chapter 2, namely “Metal scrap recycling: state of the art”, contains the analysis of the state of the art of the secondary production, dealing with both conventional remelting technologies (*Paragraph 2.1*) and innovative direct processes (*Paragraph 2.2*), finally focusing on the limitations affecting these recycling strategies (*Paragraph 2.3*).

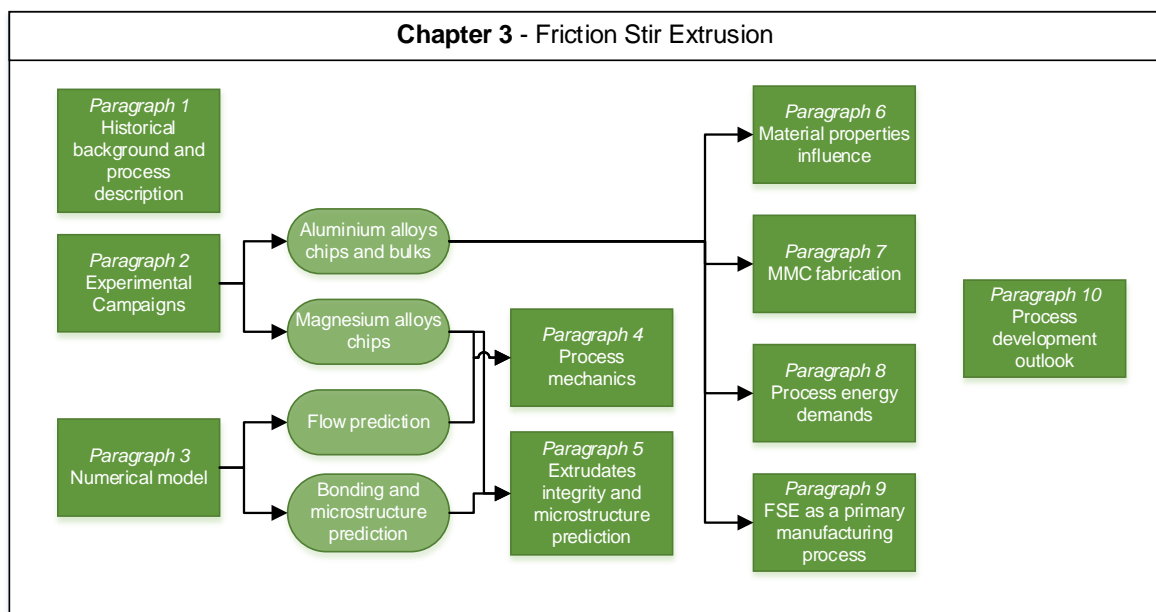


Figure 1.6. Chapter 3 structure scheme.

Chapter 3, namely “Friction Stir Extrusion”, focuses on the first of the innovative SSR strategies being analysed: Friction Stir Extrusion. After presenting the literature review, the process parameters of this technology are described in *Paragraph 3.1*. The experimental campaigns carried out to investigate the FSE process are hence described in *Paragraph 3.2*, while *Paragraph 3.3* describes the FEM numerical model implemented to simulate the process itself. In *Paragraph 3.4* the process mechanics, with particular focus on the material flow, are described using both experimental and numerical results on AZ31B magnesium alloys. *Paragraph 3.5* deals with AZ31B extrudates microstructure and defects using the numerical model

to predict them, while the influence of different AA mechanical properties on the process variables is investigated in *Paragraph 3.6*. The capabilities of FSE for MMC manufacturing and primary wire production are investigated in *Paragraph 3.7* and *Paragraph 3.9* respectively. *Paragraph 3.8* deals with the environmental impact of the FSE process compared to other recycling routes. Finally, in *Paragraph 3.10* the FSE process key factors and outlooks are summarized.

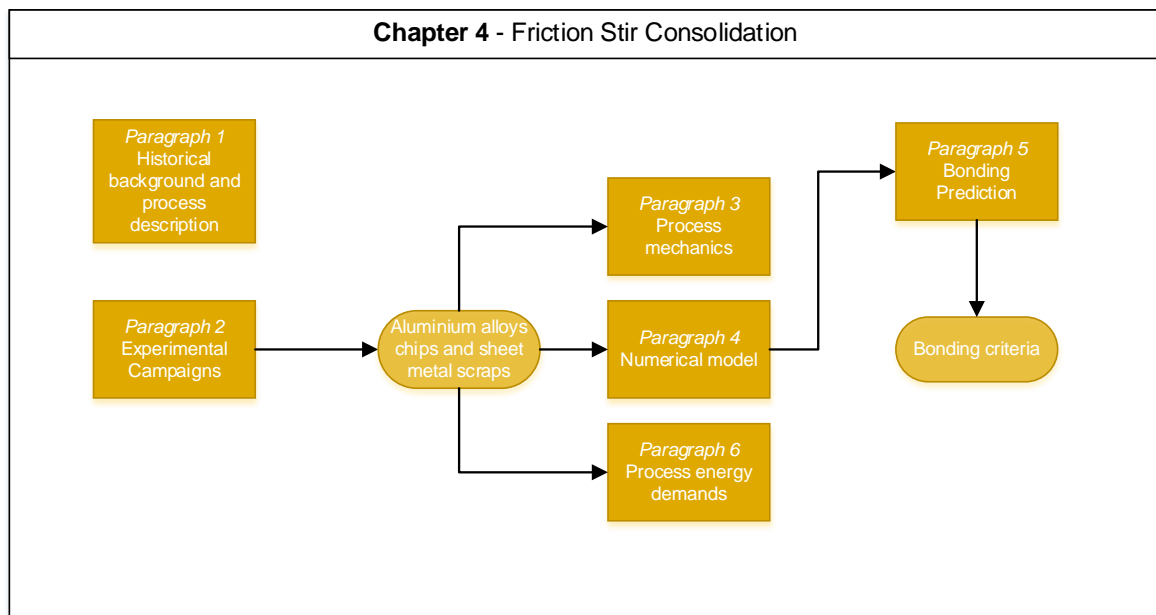


Figure 1.7. Chapter 4 structure scheme.

Chapter 4, namely “Friction Stir Consolidation”, has structure and aims similar to the previous chapter, but focusing on the Friction Stir Consolidation process. In *Paragraph 4.1* and *Paragraph 4.2* the literature analysis, process parameters and the utilised experimental setup are presented. *Paragraph 4.3* presents the analysis of the process mechanics, with particular focus on the consolidation evolution and a numerical model to simulate the FSC is described in *Paragraph 4.4* with the proposition of a dedicated bonding criteria in *Paragraph 4.5*. Finally, the energy demands of the FSC processes are compared to other analogous technique using experimental measurements and LCI techniques in *Paragraph 4.5*.

Chapter 5, namely “Conclusion”, provides a summary of the general results obtained for both FSE and FSC consolidation processes, highlighting the advances of the state of the art enabled by the research presented in this dissertation (*Paragraph 5.1*). *Paragraph 5.2* finally provides a general outlook of the investigated process, focusing on the possible future developments of this work.

2. Metal scraps recycling: state of the art

2.1 Conventional processes

The economic relevance of metal scraps recycling has been acknowledged long before the environmental implications. Technical reports specifically covering the lightweight alloys chip recovery can be dated back to the early 20th century [9]. The highly intrinsic commercial value of lightweight alloy made remelting economically attractive also considering that recycling required much less energy and effort with respect to primary production (Figure 2.1). Of course, all the conventional recycling routes included the remelting of the scraps, preceded by intermediate operation aimed at minimizing the dross formations.

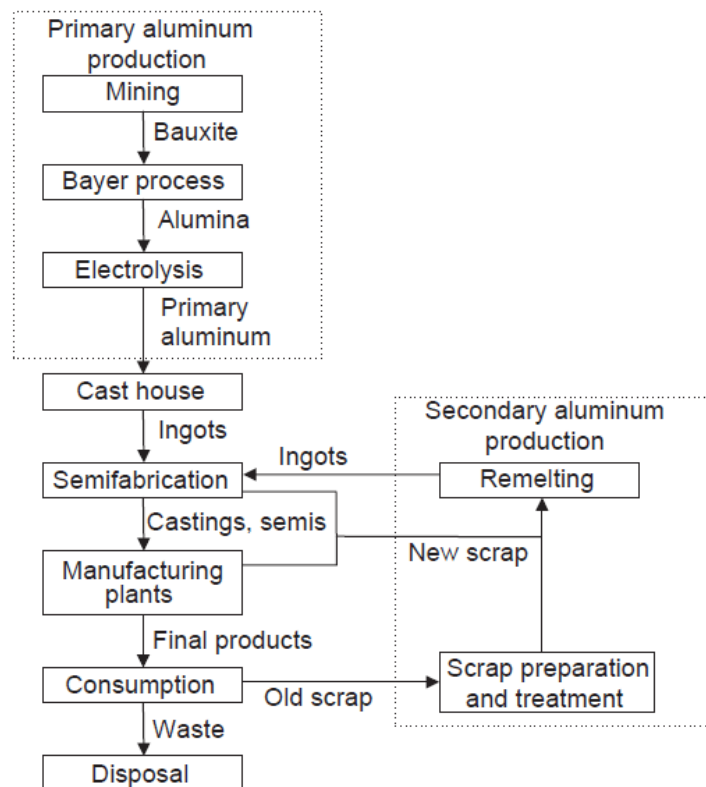


Figure 2.1. Material flow of aluminium production (Source: [10]).

The specific recycling route may vary significantly depending on which kind of scrap is being processed but can be globally grouped into pre-processing operations and actual melting of the scraps. Figure 2.2 shows some of the most common strategies for different kind of aluminium scrap.

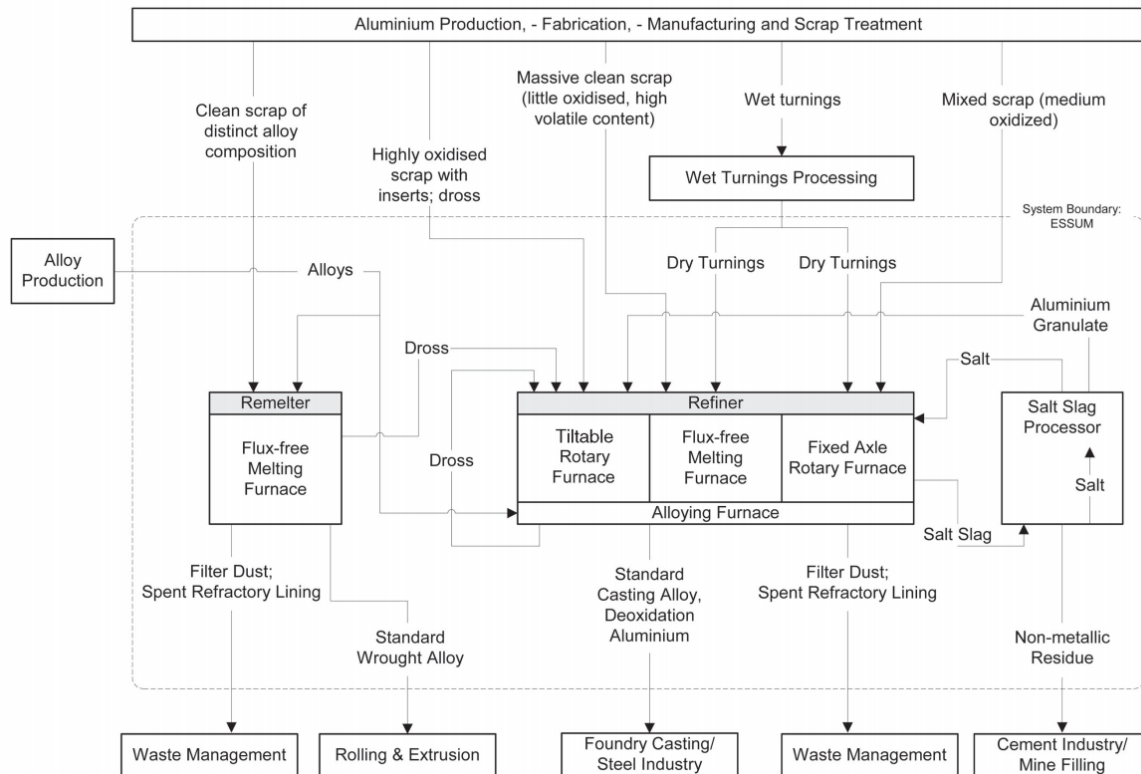


Figure 2.2. Common material flows into the aluminium scrap recycling industry (Source:[11]).

2.1.1 Scrap Preparation

Metal scraps are always characterized by a thin layer of oxide (about 10 nm for most lightweight alloys) but that amount may drastically increase during the remelting due to further oxidation prompted by high temperatures. Furthermore, machining chips and sheet metal scrap may be covered by lubricant and other contaminants that can produce both slug and hazardous fumes if added into a furnace without previous treatments. Grayson [12] states that each unit of cutting fluid burned off during remelting of contaminated chips produces two units of additional dross in the molten bath. In order to face that issue the metal scraps to be recycled usually undergo a deep cleaning with a proper degreaser before being

further processed. In Table 1.1 some of the cleaning processes available in literature are presented [13]. After the cleaning, a drying step is hence necessary in order to reduce the moisture level of the scrap. Chip drying system usually combine centrifuge and a thermal drying station that heats the wastes up to 300-350°C [12] to lower the moisture level to about 0.2% vol. Most new scrap comes into the recycling route directly from the industries that produced them. Because of that, they are uncoated (except for the normal oxide layer) and should be characterized by known and uniform composition if properly sorted by the producer. Other common pre-processing operations include cutting, baling, or shredding [10] in order to uniform also the shape and the dimension of the scrap before melting them. Briquetting (Figure 2.3) by light compaction of the loose chips in order to ease transport and handling is a common strategy but can be detrimental in terms of recycling efficiency. This is because the briquettes are lighter than the solid metal and tend to float on the melting bath prompting further scrap oxidation [12]. Magnetic separators are often used to extract any ferrous residual that may contaminate the scrap.



Figure 2.3. Metal chips briquettes (Source: Pyrotek).

Table 2.1. Cleaning process proposed in literature.

Source	Process	Material	Degree of cleaning
Dutra et al. (2007)	Washing (solvent)	Aluminium	100%
Gronostajski and Chmura, 2000	Washing (water)	Iron, aluminium, copper	N/A
Von Hohendorff and Junior (2007)	Decantation, centrifuging	Cast iron, brass	60%, 90%
Giacaglia and Guimaraes (2012)	Segregation and compaction	Aluminium	N/A
Fu et al. (1998)	Washing (solvent), heating under high pressure	Steel	86%
Khamis et al. (2015)	Washing (acetone)	Aluminium	N/A
Lucci et al. (2015)	Washing (water and detergent)	Magnesium	N/A
Torkar et al. (2010)	Washing (solvent) Heating in muffle furnaces	Steel	100%

2.1.2 Smelting and Refining

Several melting techniques can be applied to recycling depending on the nature of the scrap. If processing scrap with well-known composition and segregation are processed, they are collected into the so-called “remelter” composed of flux-free reverberatory furnaces. The direct remelting does not require any refining operations and produces new wrought alloys together with some dross that can be further recycled. Scrap characterized by higher levels of contaminants and oxides have to be further refined after the melting that happens in rotary furnaces with the adding of salt fluxes. These additives are necessary to clean the melt collecting contaminants that are trapped into the so-called “salt slag”. The salt slag resulting as waste at the end of the remelting are still rich in metals (up to 20% of the material being recycled) and needs to be processed again to recover as much material as possible and to regenerate the salt flux.

This further processing of recycling route wastes was actually introduced in the last decade in order to reduce the usage and the disposal of such expensive and dangerous substance [14]. The metals obtained by such techniques have imprecise and variable compositions; they can be used directly only as casting alloys. In fact, cast materials are usually characterized by wider alloying elements concentration tolerance with respect to standard wrought alloys. Alternatively, the moulded bath needs to be further refined in an alloying furnace to correct the chemical composition. This tuning may be carried out adding alloying elements or primary material aimed at diluting other elements concentration (Figure 2.5).



Figure 2.4. LOTUSS vortex furnace (Source: Pyrotek).

The furnaces used for the remelting process may vary a lot with as well with the remelting technique being adopted. The main aim of every specific configuration is to prevent the floating of the wastes on the surface by inducing moulded metal vortices that submerge them as soon as possible.

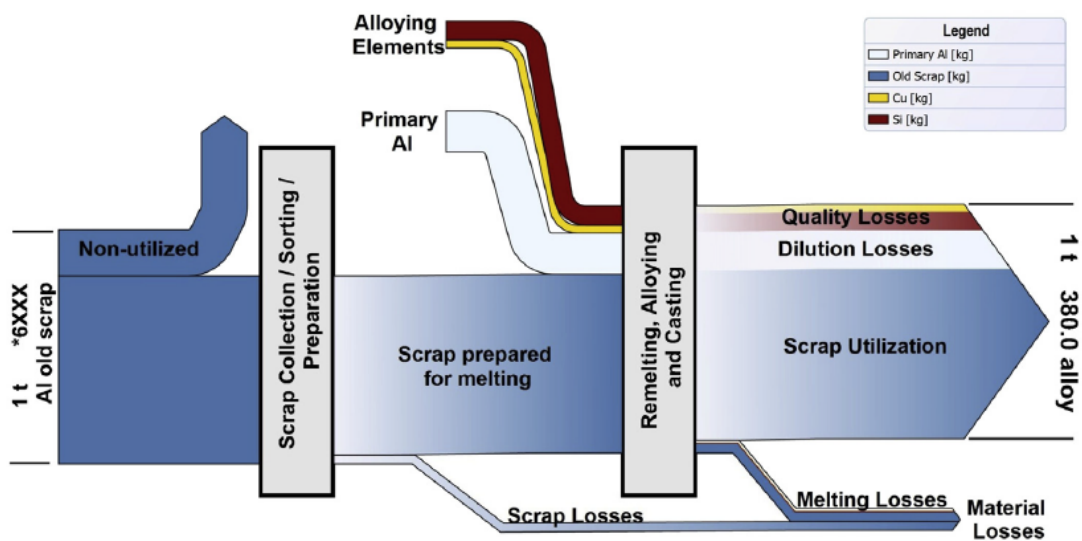


Figure 2.5. Sankey diagram illustrating material, quality and dilution losses during recycling of old scrap from the 6XXX series to produce 1 ton of 380.0 alloy (Source:[15]).

In Table 2.2 the main furnaces available for different kind of scraps are presented. It is worth noticing that most of these furnaces are highly expensive and remain rare [16] favouring centralized recycling facilities and many concerns are reported by researchers concerning workers safety. In fact, highly intense electromagnetic fields are produced by this kind of furnace in order to induce the moulded metal vortex that characterizes their efficiency.

Table 2.2. Furnace types and specifications [16]

Furnace type	Variations	Principal application	Specificities / features	Comments
Reverberatory	Standard	Melting larger volumes of clean scrap and primary feedstock	<ul style="list-style-type: none"> - Large metal capacity ($\leq 100t$). - Few restrictions on feed stock sizes. - Low or no salt flux use - Main co-products: mainly dross 	<ul style="list-style-type: none"> - High yields due to quality of feedstock - Molten metal pumps sometimes used
	Side Well	As above, but enables efficient recovery of some finer feedstocks.	<ul style="list-style-type: none"> - Large metal capacity. - Wide range of feedstock possible. - Main co-products: dross only 	<ul style="list-style-type: none"> - High yields possible depending upon quality of feedstock - Molten metal pumps sometimes used
	Sloping Hearth	Separation of Al from higher melting point metal contamination (i.e. iron/steel)	<ul style="list-style-type: none"> - Very efficient at removing high melting point contaminants. - Lower thermal efficiency - Main co-product: mainly dross 	<ul style="list-style-type: none"> - Sometimes incorporated into other furnace types. - Yield dependent on level of contamination.
Rotary	Fixed Axis	Recycling a wide range of feedstocks	<ul style="list-style-type: none"> - No feedstock restrictions - Large charge volumes possible ($< 50t$) - Feedstock size may be restricted - Relatively high usage of salt flux. - Main co-product: salt slag 	<ul style="list-style-type: none"> - Resultant salt slags can be reprocessed.
	Tilting	As above	<ul style="list-style-type: none"> - As above, but lower use of salt flux. - Feedstock size may be restricted - Main co-product: salt slag 	<ul style="list-style-type: none"> - Tends to be used for lower scrap grades.
Induction (not used in models)	Coreless	Melting of cleaner scrap or primary feedstock	<ul style="list-style-type: none"> - High yields obtained. - No salt flux required. - Flexible use (batch and continuous processing possible) - Relatively small load ($< 10t$) - Restricted feedstock type - Feedstock size may be restricted 	High cost (electricity)
	Channel	As above.	<ul style="list-style-type: none"> - High yields obtained. - No combustion gases - No salt flux required - As above, but able to have larger capacities ($\sim 20-25t$) 	High cost (electricity)

2.1.3 Recycled alloys quality

As already mentioned, one of the main challenge to be faced recycling metals is the scrap segregation. Despite the high metal potential for systematic recycling, the precise designation required for many wrought alloys impose many quality

constraints of the recycling process. Processing new scrap only usually allows meeting these requirements by enrolling closed-loop recycling strategies, based on a single alloy that requires very few “tuning” of the secondary material composition by adding alloying elements or primary diluent. On the other hand, the open recycle loop allows collecting different kind of metal wastes obtaining in cascade by down-cycling lower quality secondary alloys (i.e. cast alloys), while the recovery of higher quality alloys (i.e. wrought alloys or even unalloyed materials) obviously requires dilution (sweetening) and subsequent refining processes. The flowcharts of these different recycling pathways for aluminium alloys are depicted in Figure 2.6.

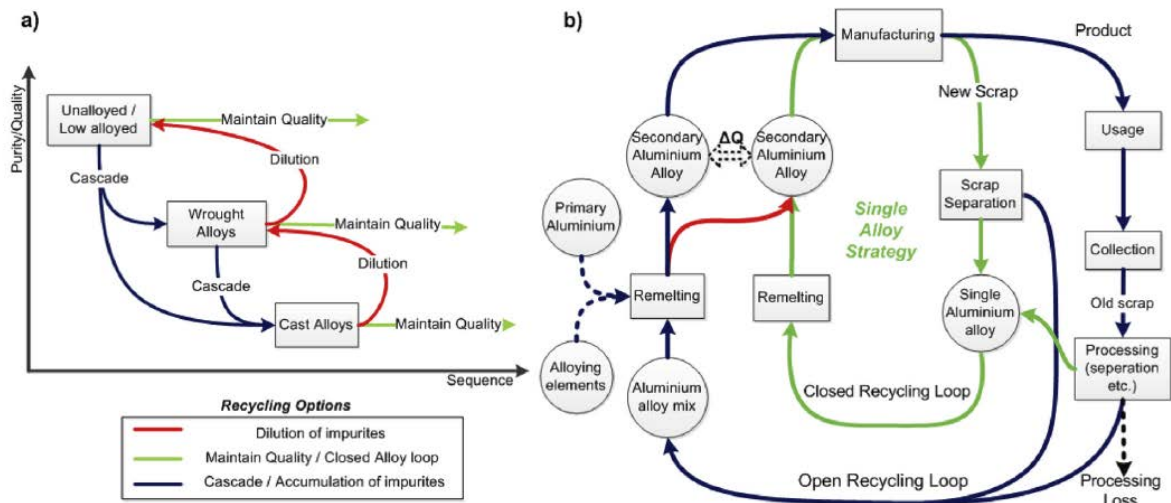


Figure 2.6. (a) Aluminium cascade recycling chain and (b) corresponding pathways (Source:[17]).

Unfortunately, recent studies based on thermodynamical analysis showed that the refining and purification options for lightweight alloy, with particular reference to aluminium, are definitively limited. Nakajima et al. [18] investigated the removability of 45 alloying elements from aluminium alloys with varying melting conditions (oxygen partial pressure and temperature). Results showed that only six of the examined elements can be removed effectively by the alloy through evaporation and/or oxidation in the slug, and only two of them are typical alloying elements present in standard wrought alloys designations (Mg, Zn). Refining of other elements is, hence, technically difficult and economically not convenient.

Magnesium and titanium alloys are characterized by similar issues regarding refining processes [19,20] and a comprehensive overview of the refining limits for most alloys is presented in Figure 2.7. Considering the limits of the refining processes, proper process planning and scrap selection result to be crucial factors to keep the recycling chain as sustainable as possible.

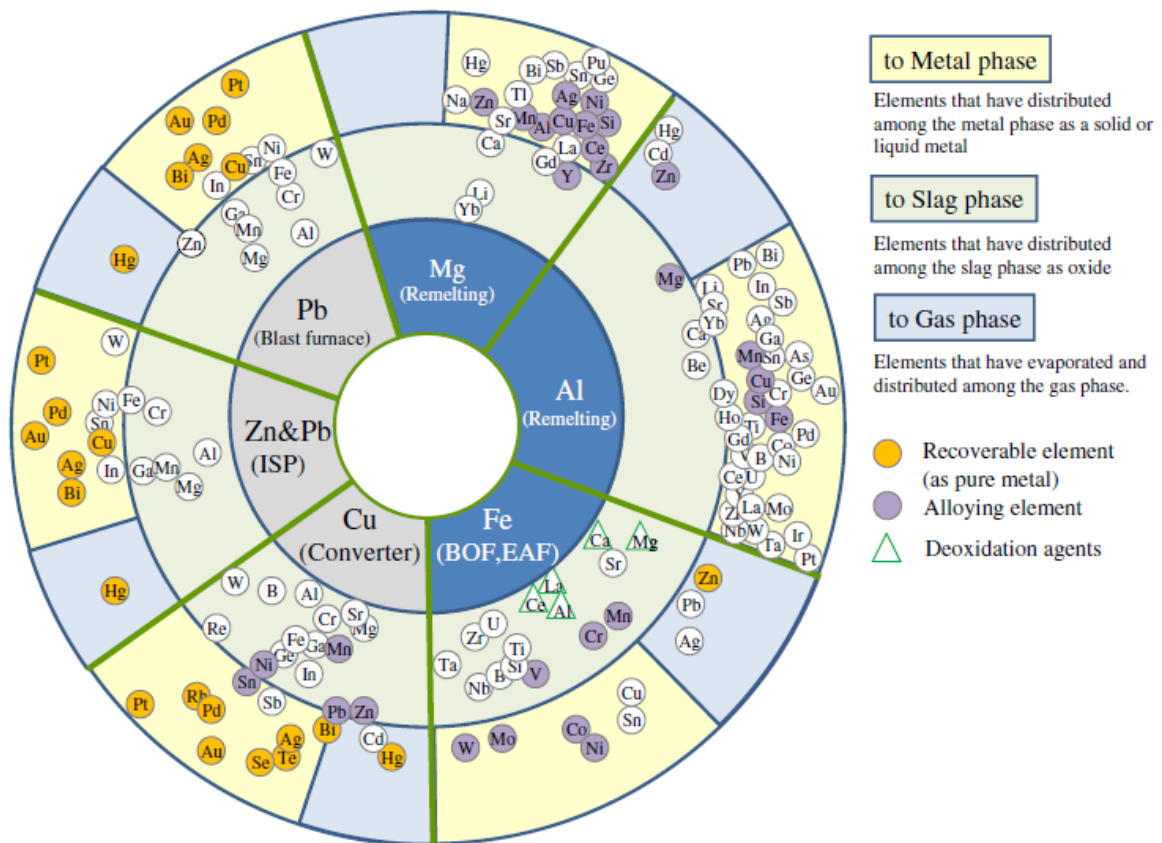


Figure 2.7. Element radar chart for the recycling of Fe, Cu, Zn, Pb, Al and Mg into the metal phase (Source:[19]).

Most of the data proposed in the last chapter have been referred to aluminium alloys, whose recycling know-how in literature is the widest available between the lightweight alloys. Although, most of the considerations can be easily extended to magnesium alloys, that are characterized by similar mechanical and chemical properties and share with the AA most of the recycling techniques and critical issues.

2.2 Innovative direct processes

Irrespective of the recycling route adopted, some dross will result from the melting based recycling process, containing about 40-80% of metals; subsequent treatment of the slug allows to reduce that amount, but likely 15-20% of the initial charge of scrap will be permanently lost into the slug itself [7]. In order to overcome that issue, many researchers started investigating new recycling technologies capable of reducing the permanent material losses by avoiding the melting step. Stern [21] first proposed and patented the hot extrusion as a recycling process (Figure 2.8) to be applied to metal chips in 1944 [22] and 1945 [21]. In 1951, Stern further developed the idea of proposing a continuous hot extrusion process based on a rotary furnace heating the scrap to the processing temperature [23].

In 1977 Sharma et al. [24] further developed these studies producing aluminium bar and cans from metal swarfs through backward extrusion. Nevertheless, only in 1999 Gronostajski and Matuszak [25] formerly defined the direct conversion method as a comprehensive recycling route capable of remanufacturing metal scrap into secondary produced raw materials. Most of the meltless processes that have been hence developed are based on Severe Plastic Deformation (SPD) of the scrap to be recycled. By imposing large plastic strain, those processes allow breaking the oxide layers between the particle, while the combination of temperature, pressure and process time prompt solid bonding phenomena between the distinct material flows [26]. Furthermore, SPD processes are known to produce ultra-fine microstructures on the products that usually shows better mechanical properties than the ingots [27]. These peculiar characteristics of SPD technologies allow to set-up recycling strategies free of the remelting-linked issues while also reducing the secondary energy and the environmental impact of raw materials production [28]. Many researchers has investigated the feasibility of such processes to recycle

lightweight alloys (i.e. aluminium [29] or magnesium [30] alloys) highlighting the advantages over the conventional techniques. In the next paragraphs, some of the most important direct recycling techniques are described, with a particular focus on the SPD and solid bonding based processes.

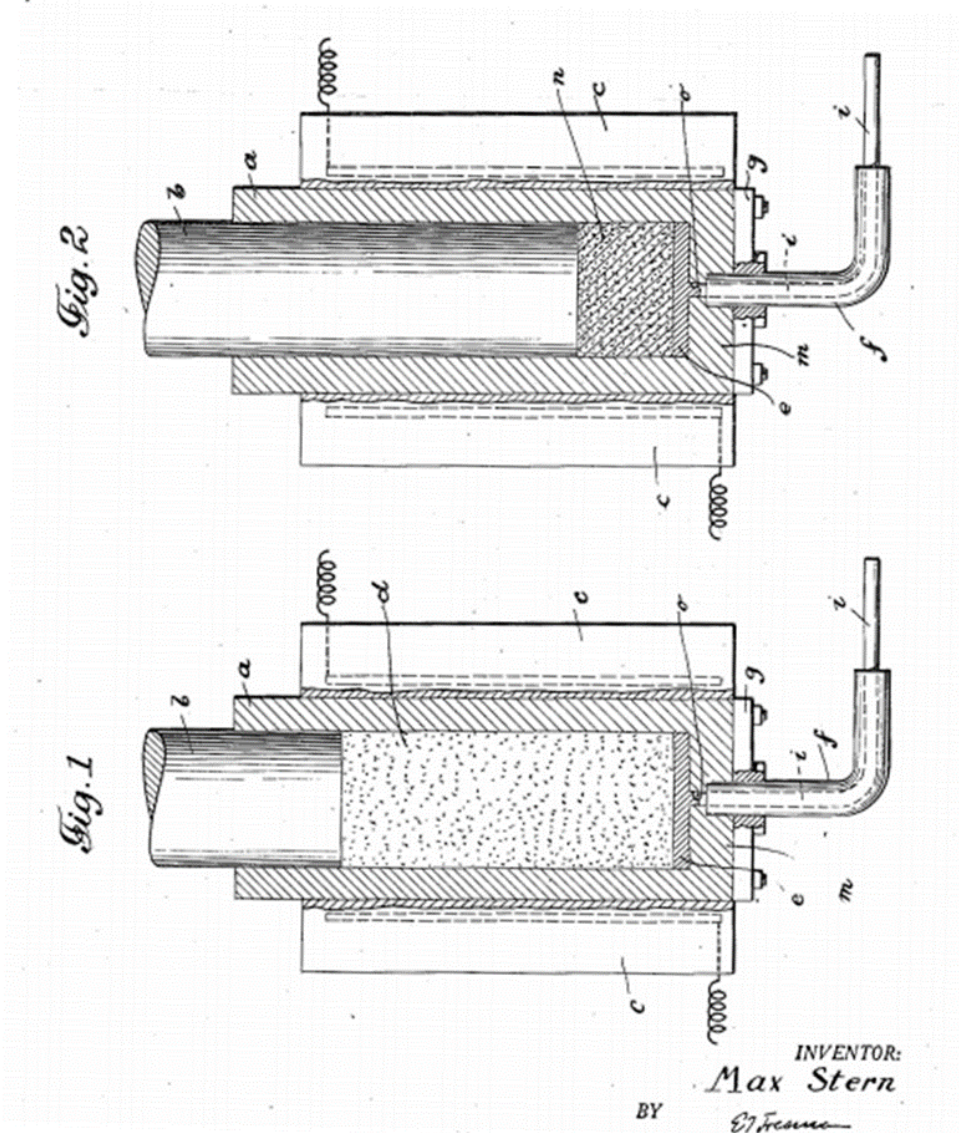


Figure 2.8. Scheme of the hot extrusion recycle process from the original 1945 patent by Stern [21].

2.2.1 Hot Extrusion

Recycling by hot extrusion of metal scrap is one of the first direct strategy being proposed and consists in three major phases. Chips to be recycled are cleaned and dried, then cold compacted and finally hot extruded (Figure 2.9a,b) into the desired shape [25]. In 2005, Ji et al. [31] investigated the feasibility of that recycling route on

simple direct extrusion of magnesium alloy scrap, while Tekkaya et al. [32] dealt with the hot extrusion of AA6060 scraps using a complex extrusion chamber (Figure 2.9c,d) to enhance material deformation. In the same paper, the authors investigate the feasibility of the hot extrusion of a mixture of aluminium scrap and silicon carbide (SiC) to directly produce metal matrix composites (MMC). This MMC production strategy has been investigated by distinct researchers [33–36] on many different hardeners and lightweight alloys.

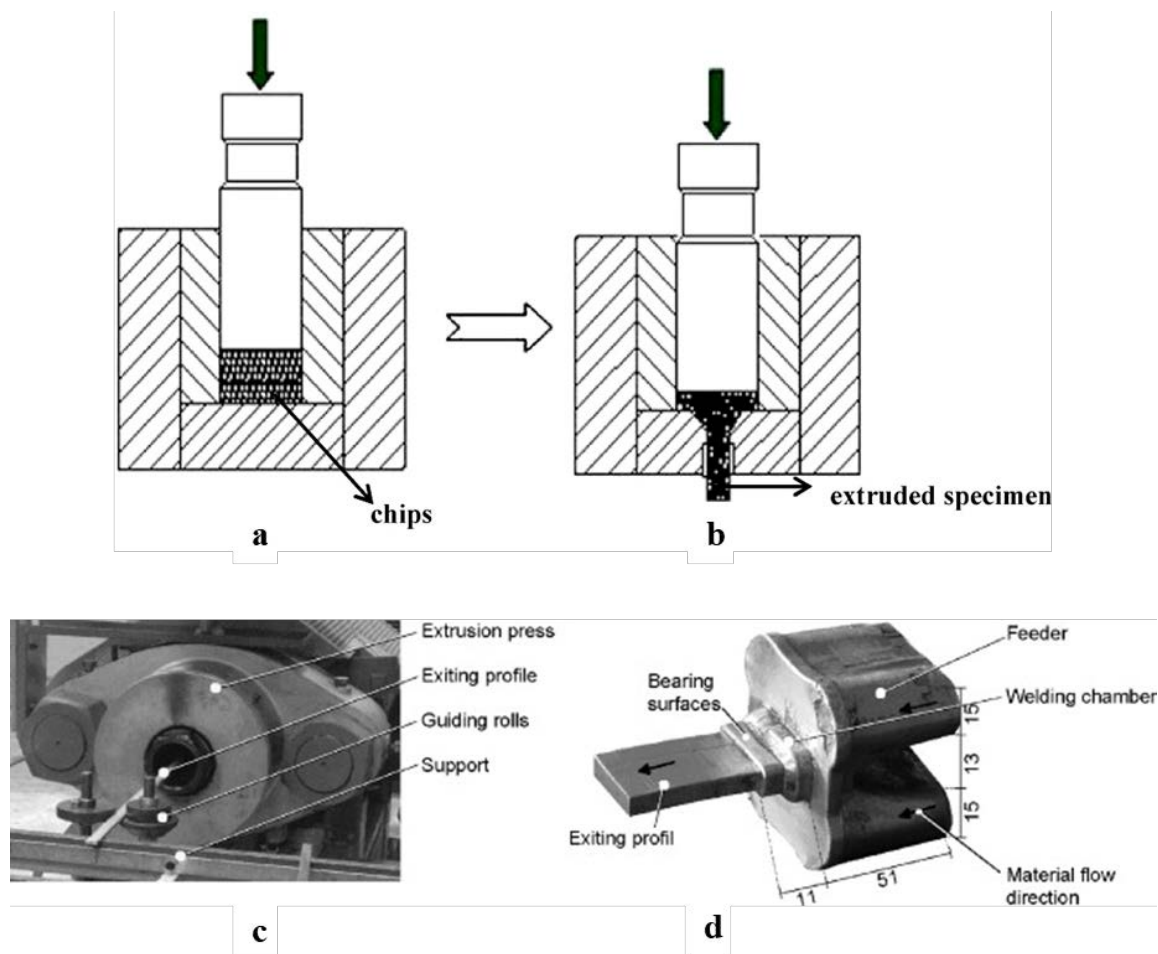


Figure 2.9. Scheme of the hot extrusion recycle process (a) col compacting, (b) hot extrusion (Source:[31]). (c) Extruded chips exiting the die and (d) view on the material flow inside the die based on exemplary press rest of a casted billet (Source:[32]).

As observed by Guley et al. [29,37] the usage of a porthole extrusion die allows to dramatically improve the recycled material mechanical properties with respect to direct extrusion; the increased deformation and shear the material undergoes during the process enable effective oxide layers breakage, resulting in better

welding of the particles. Figure 2.10 shows the enhancement in ductility that the die choice allows.

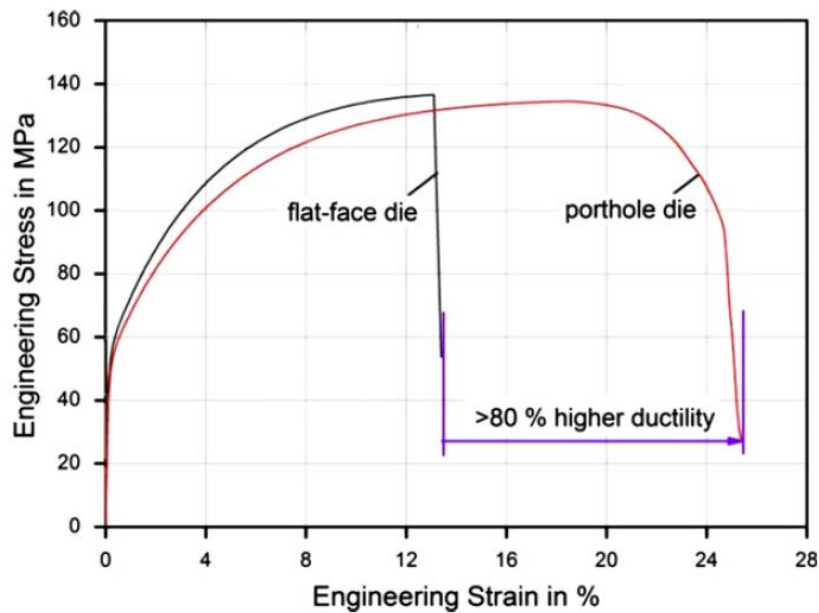


Figure 2.10. Tensile test results of aluminium profiles extruded from chips through the flat-face and porthole die. (Source:[29]).

Some of the same authors [38] demonstrate the feasibility of this direct recycling technology to process mixtures of scraps; cold compacted billets of AA6060 chips and AA1050 pins have been effectively extruded into rectangular profiles. The properties of this material were characterized by intermediate strength with respect to both parent alloys. This kind of application is particularly relevant in the perspective of open loops recycling strategy that could need adjustments of the secondary material compositions by dilution.

The hot extrusion process was demonstrated to be a very effective technology to direct recycle many different materials. The main process parameters that affect final product quality are extrusion ratio, temperature and die shape. An overview of the lightweight alloys and process parameters being investigated in literature is available in Table 2.3. The energy requirements of the process are definitely lower than the conventional remelting route [17] but the overall efficiency is affected by the preprocessing operations (particularly the cold compaction).

Table 2.3. Summary of extrusion parameters investigated in literature (Source: [39]).

No	Parameter	Author														Conclusion/ Remark						
		Material	V.Guley (2013)	M.Haase (2012)	Cunsheng Z (2012)	Hu Moe-liang (2012)	Wojcitech Z. (2012)	Tietei Zhang (2011)	Hu Moe-liang (2010)	A.E. Tekkaya (2009)	Shuyan Wu (2009)	M. Schikorra (2008)	Hu Moe-liang (2008)	Yasumasa C. (2006)	Yasumasa C. (2005)		Yasumasa C. (2004)	J.B. Fogagnolo (2003)	J.Z. Cronostajski (1997)	Mamoru M. (1995)	Parameter Summary	
1.	Preheat Temp. (°C)	300																				
		350																				
		400																				
		450					√	√	√				√								√	Temperature Frequently/ Increase UTS
		500	√							√												
2.	Process Temp. (°C)	300				√									√				√			
		350				√					√											
		400				√					√			√	√				√			
		450	√	√	√					√	√					√			√		Temperature Frequently/ Increase UTS	
		500		√													√		√	√		
3.	Preheat Time (min@hour)	20 min						√		√		√								√	Common Preheat Time	
		50 min														√						
		1 hour																				
		2 hours	√																			
		3 hours																				
		6 hours	√																			
4.	Ram Speed (mm/s)	0.1					√															
		0.15			√			√														
		1	√	√	√		√		√		√							√	√	√		Common Speed/ Good surface
		1.2			√	√																
		2																				
											√											

2.2.2 Equal channel angular pressing (ECAP)

Equal channel angular pressing (ECAP) processes are currently used to produce ultrafine high angle grain boundaries through pure shear [40]. This process allows producing on bulk solids large unidirectional deformation with relatively low loads [41]. This technique has been successfully applied to consolidate metal powder [42–44] and manufacture MMC with different metal alloys and reinforces [45–48]. The high deformations imposed by this process are ideal in order to enhance the desired oxide breakage effect. In fact, many researchers proposed the ECAP route as a modification of the chip hot extrusion to achieve solid-state recycling.

Haase et al [49–52] used ECAP die set to directly perform hot extrusion (integrated extrusion and equal channel angular pressing, iECAP) while Luo et al. [53–56] developed a single die to process titanium chips with subsequent ECAP

passages. In the last scenario, a certain backpressure had to be applied during the extrusion process in order to restrict the chip to flow easily through the ECAP die without undergoing proper deformation. This strategy has been demonstrated to be particularly effective to achieve better particles bonding [57–59]. Schemes of the experimental set-up used to investigate these different ECAP-based recycling strategies are shown in Figure 2.11.

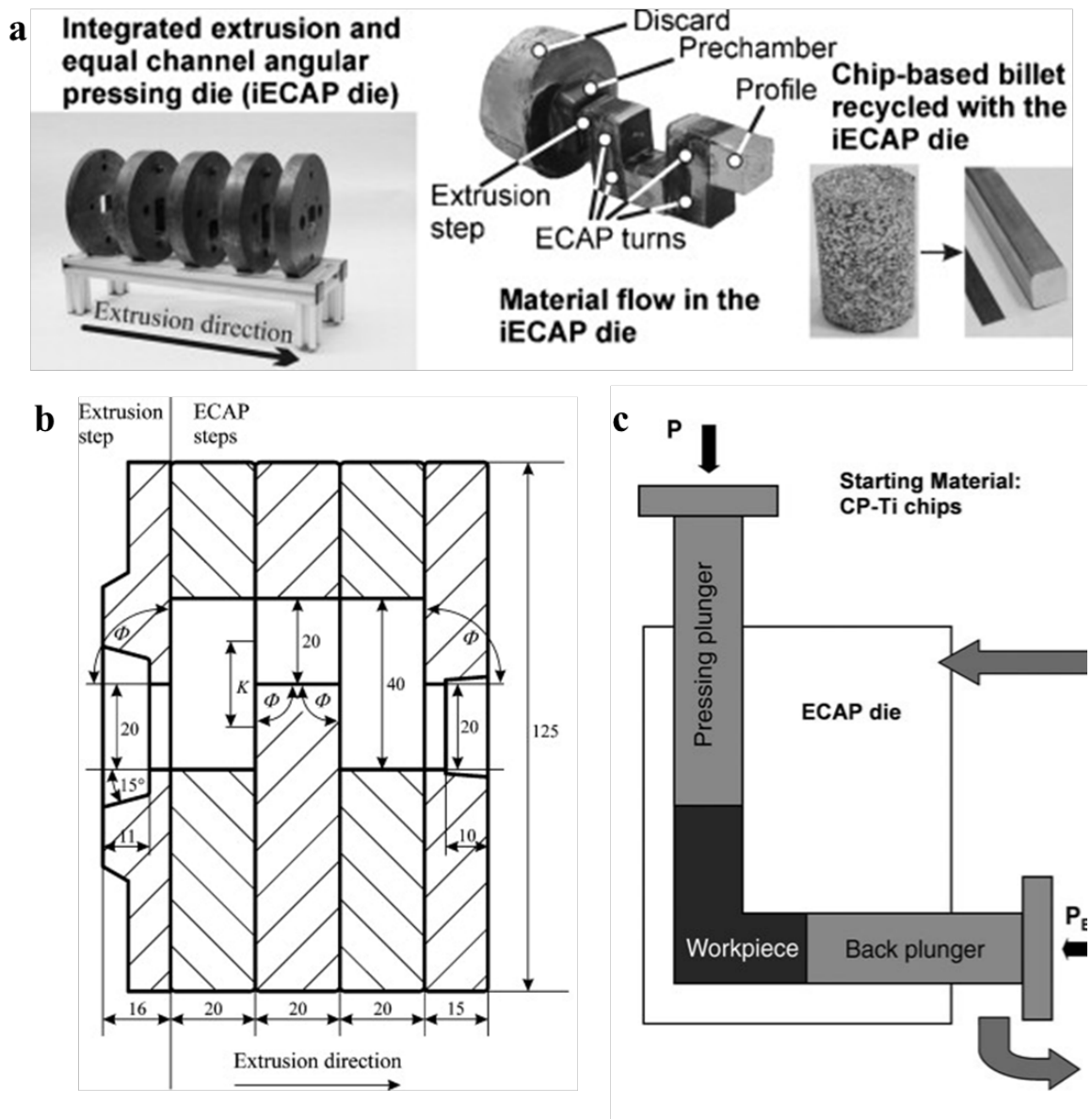


Figure 2.11. (a) iECAP process flow, (b) iECAP die geometry, and (c) back pressure ECAP process sketch (adapted from [52,56]).

2.2.3 Cyclic Extrusion Compression (CEC)

In 1985, Richert et al. [60,61] introduced the cyclic extrusion compression technique to induce very large strain into solid billet through subsequent extrusion and compression passages. The scheme of the CEC process is presented in Figure 2.12. The billet to be processed (diameter D) was pushed through an extrusion die (diameter d) into a chamber having the same diameter of the initial billet (D). Similarly to the ECAP process, CEC was initially developed to produce ultrafine-grained materials [62,63] to be hence applied to chip recycling. Peng et al. [64] applied the CEC route to magnesium alloys, demonstrating that the interface decohesion between the particle ceases to happen after 6 passages at 673 K. The process was also successfully applied to aluminium alloys [65,66]. The number of passages and the process temperature resulted to be the most influent parameters to take into account during the CEC recycling route [67].

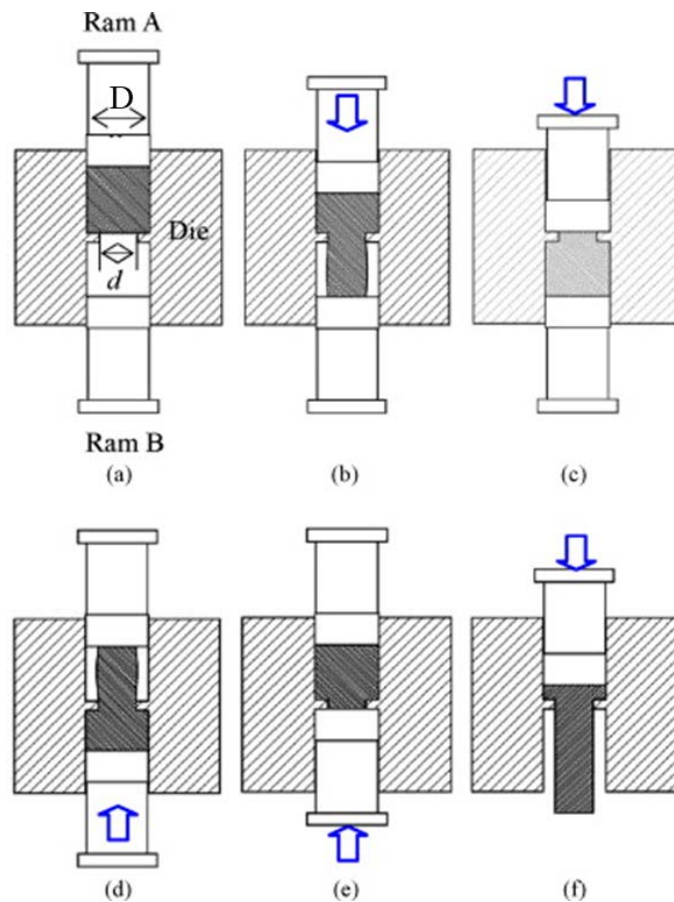


Figure 2.12. From (a) to (f) CEC process steps sketches (adapted from [68]).

2.2.4 Screw extrusion

The screw extrusion process is widely applied to extrude thermoplastic polymers starting from granulated material [69]. In 2007, Werenskiold et al. [70] patented a screw extruder dedicated to materials with high-viscosity such as metals. Figure 2.13 shows the section of the patented extruder, which works similarly to a conventional screw extruder with granulated material being fed through an inlet and fed to the die by the driving screw. The whole process is carried out at high temperature in order to allow material softening.

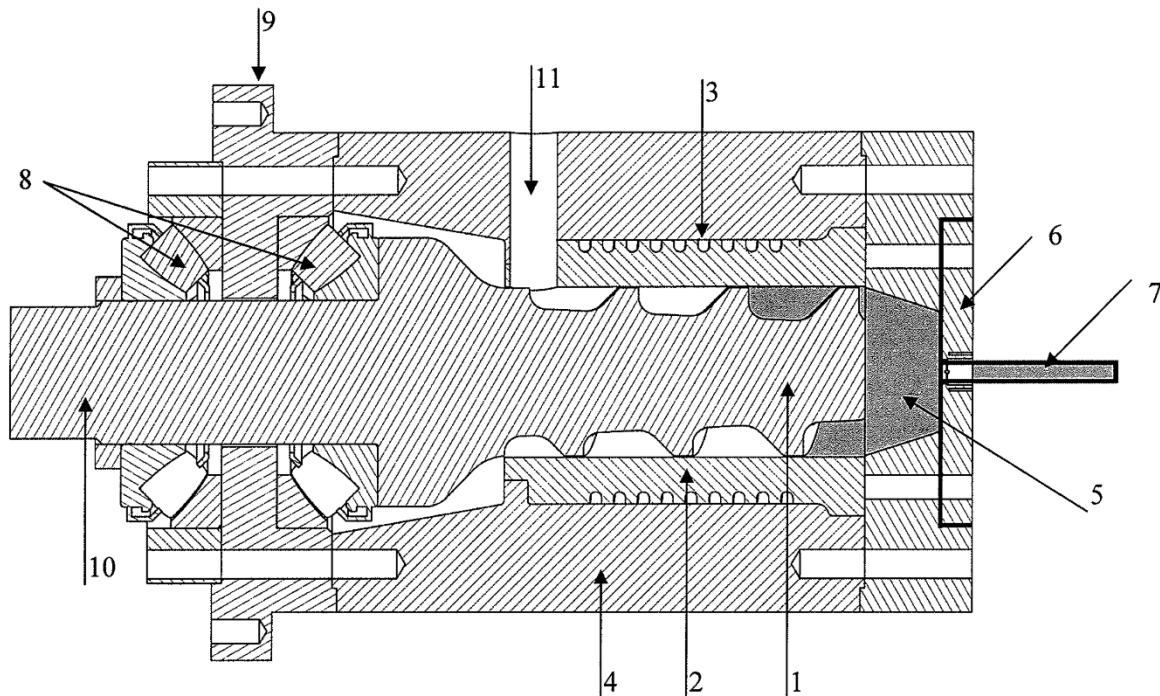


Figure 2.13. Schematic illustration of the cross-sectional view of an extruder. (1) screw, (2) liner, (3) cooling channel, (4) screw housing, (5) extrusion chamber, (6) die, (7) extruded product, (8) thrust bearing, (9) support plate, (10) screw shaft, (11) inlet (source [70]).

Wideroe et al. [71] applied the proposed extruder to AA6060 granulates, highlighting how the rotational movement highly affects the axial load of the screw. The same authors also investigated the material flow during compaction and extrusion providing insight on the extrusion pressure generation [72].

2.2.5 High Press Torsion (HPT)

As the previously described technologies, also the High Press Torsion process (HPT) was developed as a grain refinement technique. The material to be processed is held between two anvils (Figure 2.14) that apply high pressure (several GPa) while the lower anvil concurrently applies torsional deformation rotating on her vertical axes [73]. The process was initially meant to be unconstrained (Figure 2.14a) causing the processed disc to be very thin (about 1 mm of thickness) due to the radial outward flow. Different constrained versions of the process have been subsequently developed [74] allowing the manufacturing of thicker disks [75] of about 8 mm of height.

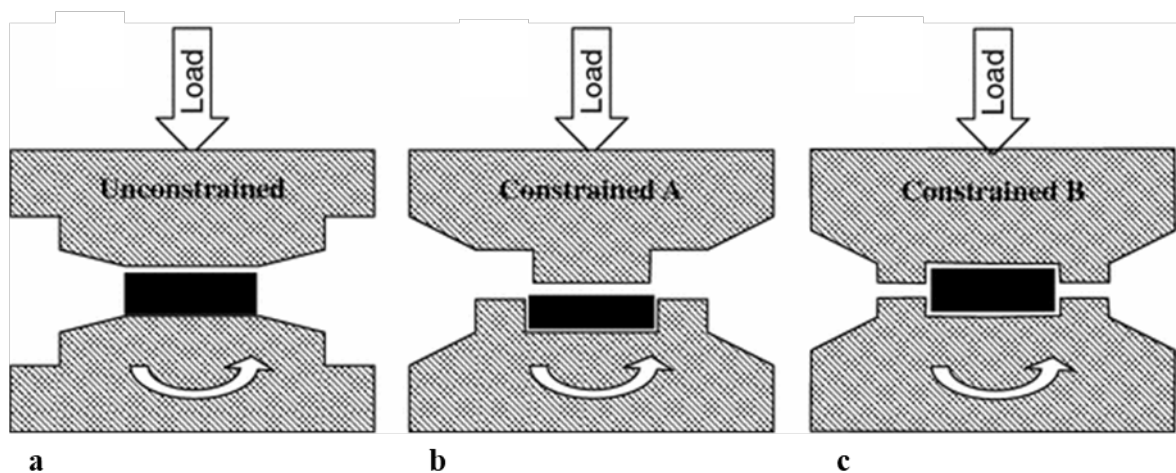


Figure 2.14. Principles of HPT for (a) unconstrained and (b, c) two types of constrained conditions (source [74]).

The HPT process was then applied to powder consolidation of different materials such as copper [76] or nickel [77] and, finally, to solid state metal chip recycling. Zhilyaev et al. [78] consolidated copper chip into ultrafine grained discs while Takahashi et al. and El Aal et al. [79,80] processed aluminium chips obtaining solid disks after 10 revolutions under 8 GPa of pressure. The obtained specimens exhibited higher mechanical resistance with respect to the parent material thanks to high-angle grains that characterized the new microstructure [80].

2.2.6 Powder Metallurgy (P/M)

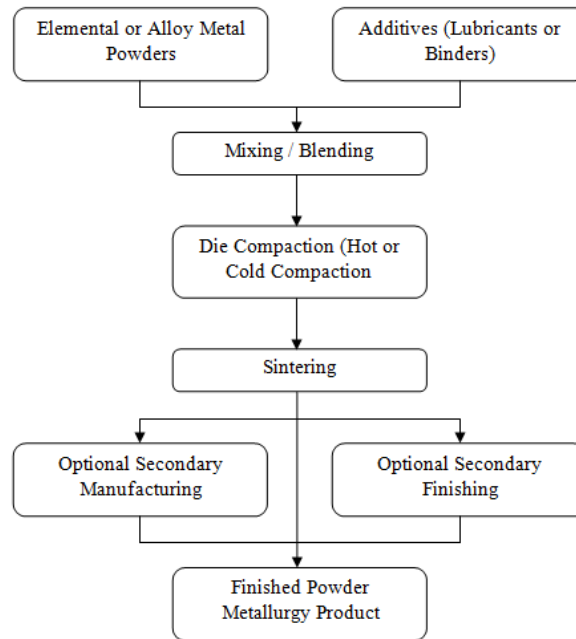


Figure 2.15. Simple process flow chart of powder metallurgy (source [81]).

Powder metallurgy has been known since 1950 as a near-net shape manufacturing technique to process metallic and nonmetallic powder through sintering [82]. In the last decade, P/M has been also successfully used for metal chips recycling. Since the process can only be applied to relatively fine powders, metal scrap to be sintered need to undergo proper preparation. While the very first applications required remelting steps to produce by centrifugal atomization the powders, mechanical chopping or milling can also be used to obtain properly even and fine scrap dimension. For example, Hong et al. [83,84] obtained flake powder by dry (under an inert atmosphere) and wet milling of aluminium foils. These preprocessing operation to obtain the powder are the main disadvantages of such process since they drastically lower the overall energy efficiency of the P/M.

In case of MMC production, the powder preparation may be bypassed directly milling the chip with the reinforce: Susniak et al. [85] achieved mechanical alloying adding SiC powder to Al-Si-Cu alloy chips while Sherafat et al. [86,87] used pure Al powder as a matrix to produce composites with the chip being recycled.

2.2.7 Spark Plasma Sintering (SPS)

The Spark Plasma Sintering (SPS) is a P/M based process that has recently been introduced and investigated as a solid-state recycling process. It is also referred as pulsed electric current sintering (PECS) and it uses the combined effect of a current (i.e. pulsed DC) and a forging pressure to break the oxide layer between particles being consolidated [88]. This sintering technique is characterized by many advantages with respect to other P/M processes, including low process time, low sintering temperature, and high reproducibility [89].

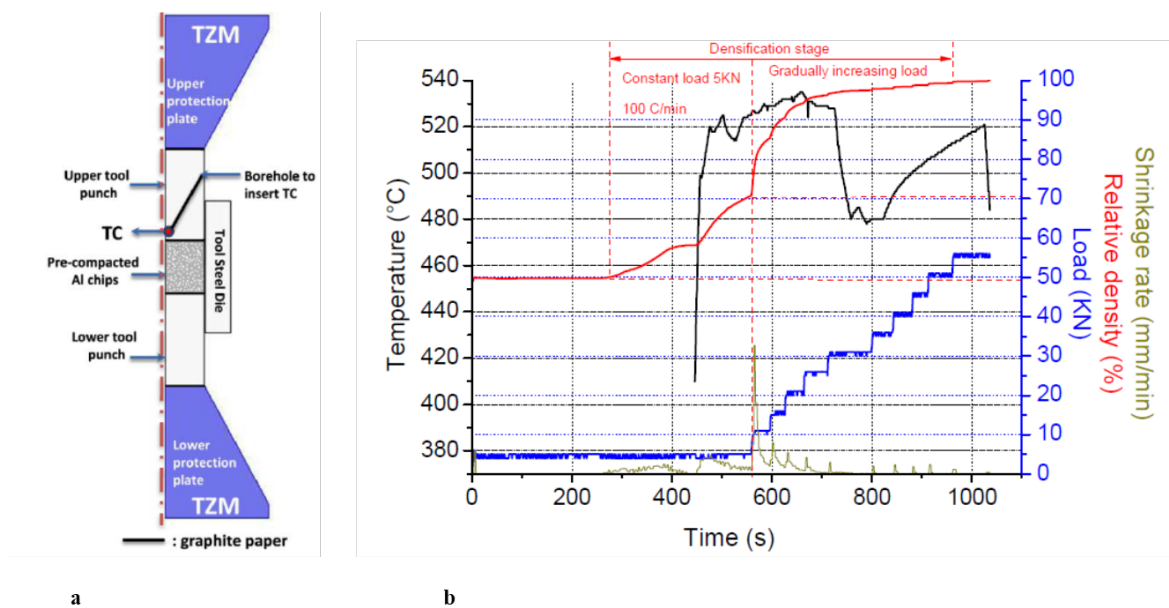


Figure 2.16. (a) SPS process scheme and (b) SPS process cycle parameters: temperature, load, shrinkage rate and sample's relative density versus time (adapted from [15,90]).

SPS has been applied for the first time to recycling routes by Paraskevas et al. [15,90,91] that managed to consolidate aluminium alloy chips, sheet metal scrap and magnesium chips. The particle to be processed were cold compacted and placed into the sealed hollow matrix (see Figure 2.16) between two graphite electrodes that apply the pulsed direct current (pulse time 10 ms, pause time 5 ms, 4000 pulses/min). The sintering process was carried out under low vacuum condition applying a constant load of 5 kN up to 520°C. After that threshold, the load was gradually increased up to 55kN. The process allowed to obtain fully dense and consolidated disks with good mechanical properties.

2.3 Summary and perspective of solid-state recycling

Most of the previously described direct recycling strategies have been developed in the last decade as specific applications of pre-existing technologies. The growth of such research trend proves the importance of metal scrap recycling to face new challenges for the development of a sustainable and effective manufacturing industry. The recycling strategies here described mainly apply to aluminium and magnesium alloys since they are characterized by similar mechanical and chemical properties. On the other hand, some process has also been applied to titanium alloys [53,55,56,92] that have much higher mechanical resistance and melting temperature.

These recycling process usually allow to drastically reduce the permanent material losses typical of conventional recycling processes but some drawback have limited their diffusion; they often require special and complex equipment and intermediate preparation on the material being processed while the actual energy efficiency and environmental impact of the whole route remain often unclear. In fact, very few papers can be found in literature dealing with proper analysis of these factors (LCA, LCI, etc.). In the next chapters, two direct recycling technique will be presented. FSE and FSC are meant to process incoherent material into solid wires and disks respectively. The relative simplicity of these process and the reduced amount of intermediate operation make them a promising option for direct recycling of metal scraps.

The aim of this dissertation is to reduce the lack of knowledge present in literature regarding the above cited processes. The influence of the process parameters on the extrudates quality needs to be properly investigated. On the other hand, it is necessary to deal with the influence of the mechanical properties of

the metals being recycled on the process variables. Furthermore, the actual environmental impact of these SSR processes have to be properly assessed, also in comparison with similar techniques. To achieve that results, extensive experimental campaigns have been carried out, developing dedicated numerical tools aimed at easing processes investigation and engineering.

3. Friction Stir Extrusion

3.1 Historical background and process description

In 1993, The Welding Institute (TWI) of Cambridge patented a new recycling process to be applied to metal chips, named Friction Stir Extrusion (FSE). This technique belongs to the Friction Stir Processing (FSP) technologies, developed following up the Friction Stir Welding (FSW). A rotating die is used to produce heat and plastic deformation through friction between the die itself and the chips to be recycled (into a hollow cylindrical matrix) by compacting, stirring and extruding the material.

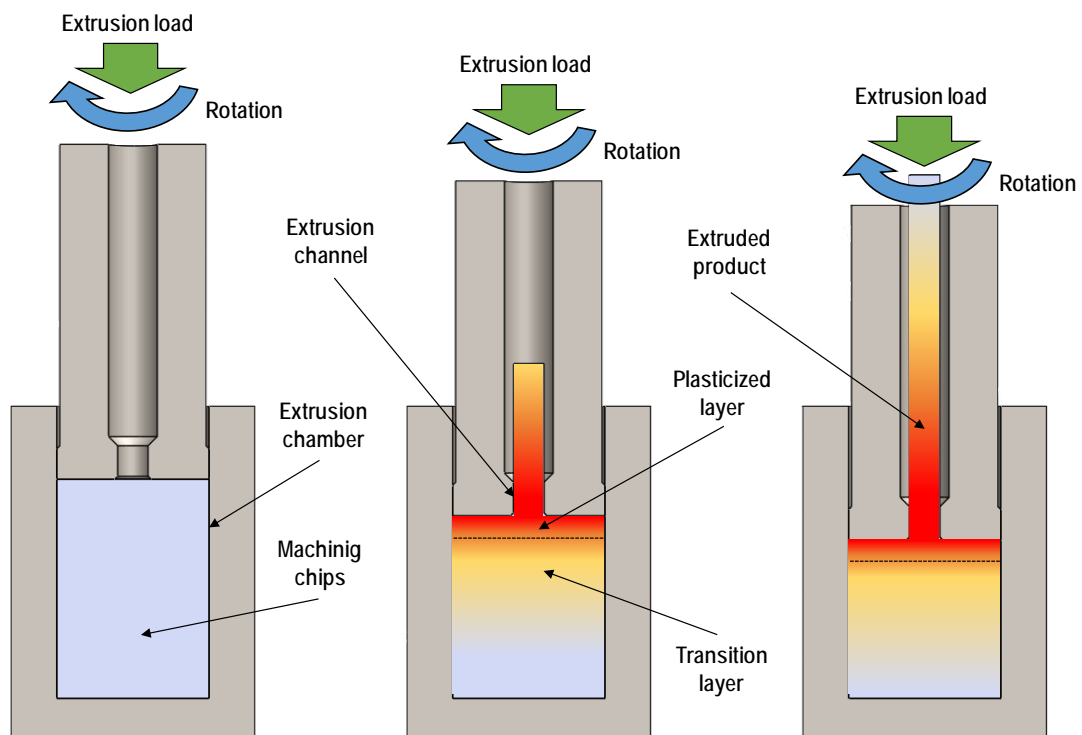


Figure 3.1. Sketch of the Friction Stir Extrusion process (source [93]).

In this way, the recycling process takes place in a unique operation, resulting in significant cost, energy and labour saving with respect to both the conventional method and the direct method. For this reason, the FSE technique appears very attractive to industry for the recycling of machining chips.

Figure 3.1 shows a sketch of the process. The chip closer to the die, i.e. closer to the heat source, rotates together with the tool and plasticizes due to the combined effect of high temperature and stirring. Moving far from the die interface, a transition layer is encountered, in which the chip is heated but has not been homogenized as a continuum material. The extrusion starts from the rotating plasticized layer and is influenced by the combined action of tool rotation and force on the tool. At the end of the process, the extruded material returns to room temperature by calm air cooling.

3.1.1 State of the art

After the TWI patent expiration due to failure to pay maintenance fee in 2002, only very few papers have been published on the process. In particular, Tang and Reynolds [94] produced AA2050 and AA2195 wires from chips using fixed extrusion force and varying tool rotation. The microstructure of the extruded wires is characterized by small equiaxial grains resulting in good mechanical properties of the wires in terms of microhardness and bend ductility. Buffa et al. [95] carried out an experimental campaign on the FSE of AZ31 Mg alloy imposing the extrusion speed through the control of rotating tool vertical displacement. The obtained results show that the process is feasible and mechanical resistance of about 80% of the base material can be reached. Tool rotation is key process parameter for the effectiveness of the process. With low rotation values, corresponding to low heat input, no extrusion is obtained. On the contrary, the combination of large rotation values and high strain can result in swirl defects compromising the specimen mechanical properties.



Figure 3.2. (a) AA6061 chips and (b) wires (source [94]).

A complex 3D helical material flow is generated by the tool action, and distinct areas are observed in the cross section of the extruded parts, with heavily stretched grain in the periphery and recrystallized grain in the centre.

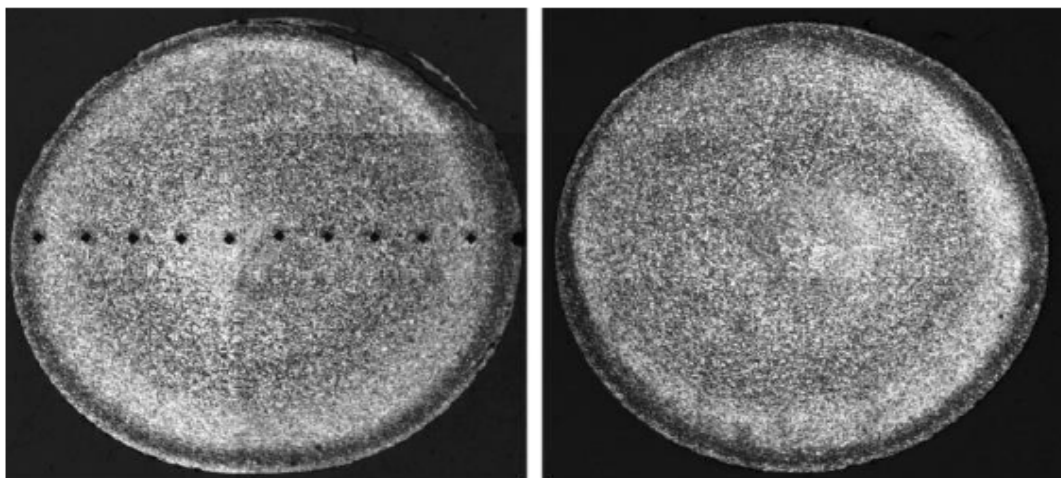


Figure 3.3. Extrudates etched cross sections (source [94]).

Although FSE can be considered extremely competitive even compared to the direct method, the real potential of the process has not been still highlighted due to the significant knowledge gap in literature, especially regarding FEM simulation which can be effective in order to have a deeper insight in the process mechanics.

Analysing and isolating the effects of each of the different technological parameters on the mechanical properties of the produced rod can be quite difficult. This problem results to be much more relevant when the extrusion is carried out assigning the extrusion force instead of the extrusion rate: in a force-controlled FSE process, the extrusion rate depends on the extrusion force and the material flow stress which is in turn influenced by temperature and flow stress varying with tool rotation. On the other hand, the temperature of the process is also dependent on the extrusion rate, vertical force and tool rotation. Hence, the problem of isolating a single parameter influence on the process results to be quite a complex task requiring a large experimental campaign in order to select the best parameters for each material. To reduce the amount of the experiments a numerical model able to predict the main fields variable as well as the extrudes quality can represent a useful design tool, usually applied in other Friction Stir process i.e. FSW [96].

Only a very limited number of papers can be found in literature based on numerical simulation on FSE. Ansari et al. [97] optimized the process parameters of FSE applied to commercially pure magnesium using statistical tools while Behnagh et al. [98] investigated the metallurgical transformation during FSE of pure magnesium through a thermo-mechanical 2D analysis. The ALE model was implemented on Abaqus and allows the prediction of Dynamic Recrystallization (DRX) during the extrusion, also providing an evaluation of the microhardness profiles along the radius of the rods. Zhang et al. [99] proposed a CFD numerical model able to provide insights into the material flow occurring in FSE of aluminium alloys. The 3D CFD model is able to predict the velocity field and it has been validated using experiments with marker particles.

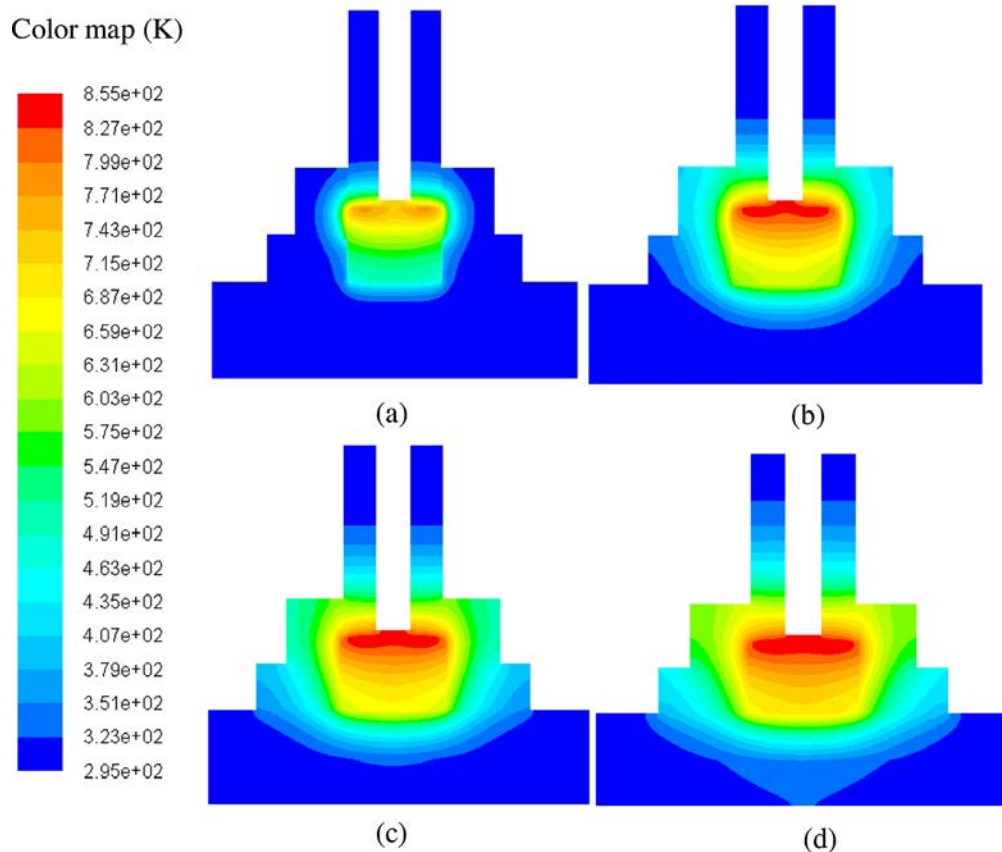


Figure 3.4. Predicted temperature contours at (a) $t = 7$ s, (b) $t = 14$ s, (c) $t = 21$ s, and (d) $t = 27.7$ s (source [100]).

The same authors furthermore investigated FSE proposing a two-dimensional axial symmetric model [100] based on ANSYS FLUENT aimed at modelling heat transfer (Figure 3.4) during the process using as input the experimentally measured mechanical power. Nevertheless, none of these models is able to predict the extruded product integrity via a unique 3D FEM simulation.

3.1.2 Process parameters

The main parameters affecting the FSE process are obviously the geometrical one. The extrusion ratio (i.e. the ration between the chamber inner diameter and the extrusion channel diameter) is probably the most influent, together with the extrusion channel length and the die shoulder geometry. In fact, in some cases, the shoulder may be manufactured with a scroll-like envy in order to enhance both radial flow toward the extrusion channel and die stirring action. The extrusion channel itself is usually countersunk in order to easy material flow.

As far as the technological parameters are concerned, extrusion force and die rotational speed are the most relevant parameter to be chosen. The FSE process is usually force controlled since the extrusion speed varies adapting to the material response. In this way, the extrusion occurs only when the raw material reaches proper levels of temperature and strain.

3.2 Experimental campaigns

3.2.1 Experimental setups

Two different dedicated experimental set ups were designed and manufactured to carry out the experimental campaigns that will be presented in the next paragraphs. The first set -up was composed by a rotating die and a chamber made in AISI H13 steel quenched at 1020°C and characterized by 52 HRc hardness (Figure 3.5). The rotating tool was characterized by outer diameter equal to 25 mm and a 10° conical concave surface in order to increase the contact area between the tool and the material to be extruded and to convey the material flow toward the tool centre, i.e. the extrusion channel. Temperature in the matrix close to the extrusion chamber, where the chips were processed, was acquired through two K-type embedded thermocouples whose position is highlighted in Figure 3.5.

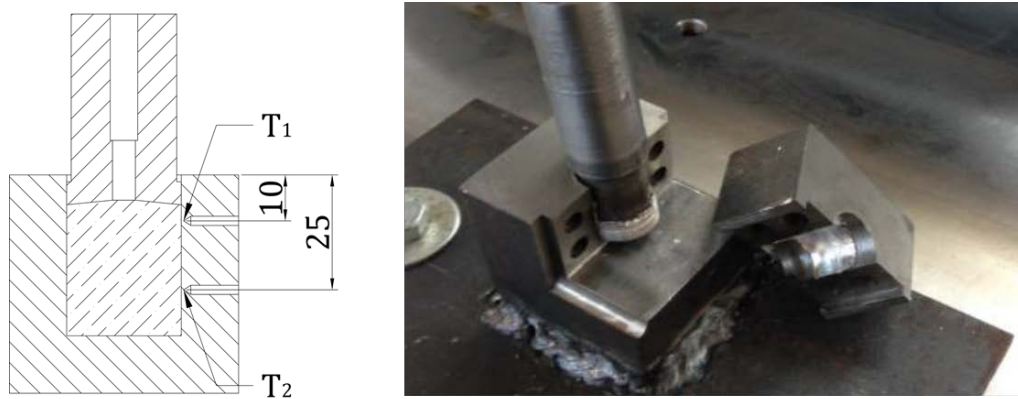


Figure 3.5. Experimental set-up #1.

This toolset was mounted on a Friction Stir Welding machine ESAB LEGIO FSW 3ST (Figure 3.6) capable of imposing the die rotation and extrusion force. The main process variables, such as extrusion rate, spindle torque etc., were monitored during the experiments by the integrated control system of the welder with a 1 Hz sampling

rate. A dedicated system to monitor the energy consumption was hence mounted on the main electric power inlet of the machine.



Figure 3.6. ESAB LEGIO FSW 3ST.

The second dedicated toolset was manufactured from H13 steel. The rotating die has an external diameter of 38.1 mm and central through extrusion channel of 4 mm in diameter and 1 mm of height before widening to 8 mm in diameter. The die shoulder presents a twin clockwise scroll of 8.9 mm (Figure 3.7a) pitch and a second through hole 8 mm far from the extrusion channel in order to house a thermocouple for temperature acquisition. The die was rotated in counter-clockwise direction in order to enhance material flow toward the central extrusion hole while the small thermocouple hole was quickly covered and obstructed by plasticized metal creating excellent contact between the charge and the sensor. The chamber (Figure 3.7b) has an inner diameter of 39.1 mm and presents four embedded thermocouples, 0.5 mm from the inner surface and with 1 mm spacing starting from the top of the billet housed inside. The chamber is clamped to a stainless steel backing plate and a small pin is placed on it to prevent billet rotation.

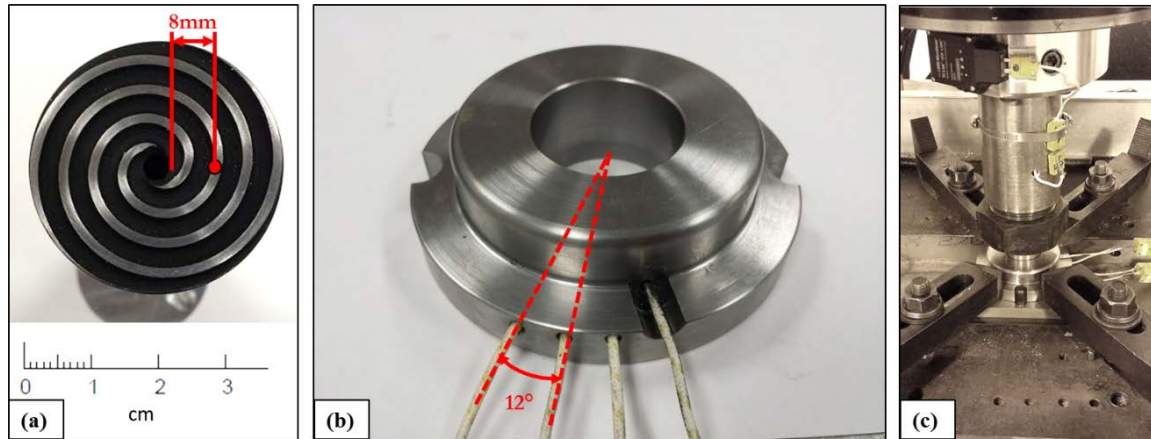


Figure 3.7. Experimental set-up #2 (a) Die scrolled shoulder, (b) Chamber and (c) assembly of the FSE setup.

Toolset #2 was mounted on a Friction Stir Welding machine operated in Z-axis force control mode (MTS Process Development System), allowing to impose a constant extrusion pressure while extrusion rate varies according to process conditions. During the extrusion, the rotational speed, die vertical movement and extrusion force were recorded by the MTS controller with a sampling rate of 10 Hz, while torque and power were recorded by a torque transducer mounted on the MTS spindle with 50 Hz sampling rate. Temperature data were acquired using K-type thermocouples embedded into the matrix and the die and recorded with dedicated National Instrument board and Bluetooth transducer respectively, with a sampling rate of 8 Hz.

The quality of obtained extrudates was evaluated under multiple points of view: micro and macro observations have been carried out, together with microhardness and tensile tests to assess material properties. Tensile tests were carried out according to ASTM E8M standards (see Figure 3.8) and Digital Image Correlation (DIC, see Figure 3.8b-3.8d) software by Correlated Solution was used in order to track the specimens' deformation during the tests using the virtual extensometer function. Cross and longitudinal sections of the extrudates were cold mounted, polished and etched with proper reagents order to highlight grain structures.

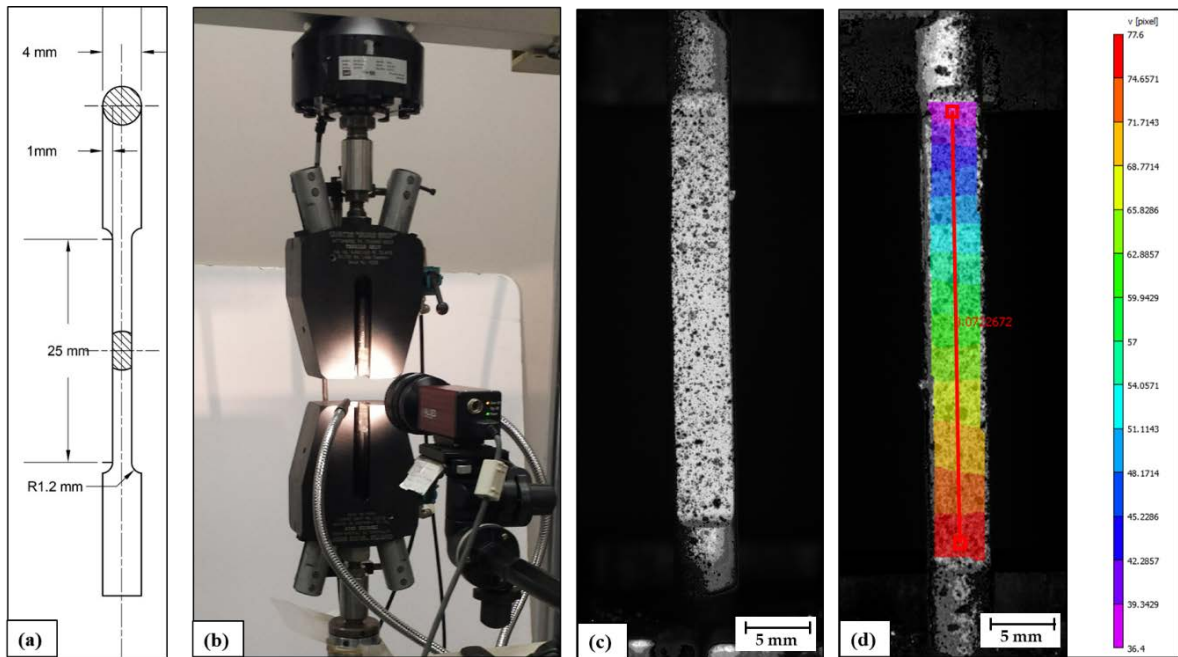


Figure 3.8. (a) Tensile specimen geometry, (b) DIC setup, (c) Speckle pattern on a tensile specimen, and (d) DIC displacement contour plot with virtual extensometer.

3.2.2 Materials

The feasibility of the FSE process for chip recycling has been investigated on different lightweight alloy; in particular extensive experimental campaigns have been carried out on AZ31B magnesium alloy, 2000, and 6000 series aluminium alloys. The experimental campaigns were aimed both at investigating the effect of the main process parameter and parent material properties on the extrudates quality and on the unconstrained process variable (i.e. extrusion rate, temperature, torque, etc.). As highlighted in the introduction, most solid-state technologies allow producing MMC within the recycling process. In order to investigate the FSE capabilities in that area, experiments have been carried out extruding a mixture of aluminium alloys chip and Silicon Carbide (SiC) micro-powder.

All the processed raw material was received in plates and milled or turned with no lubricants in order to produce a regular and clean chip. The results of all these experimental campaigns will be presented in the following chapters describing the aspects of the FSE the concurred investigating.

3.3 Numerical FEM model

In order to investigate the process mechanics of the FSE process a “single block” 3D FEM model for FSE, based on a Lagrangian implicit solver was developed [93,101]. The numerical model is thermo-mechanically coupled, with rigid-viscoplastic material behaviour. Additionally, a “bonding criterion” is developed and embedded in order to evaluate extrudes integrity and allow the insurgence of defects prediction. The numerical model was calibrated and validated using temperature data measured during a dedicated experimental campaign.

3.3.1 Governing Equations

The numerical model was developed using the commercial FEA software DEFORM-3D, Lagrangian implicit code designed for metal forming processes. The implemented FEM formulation is based on the variational approach according to which the actual velocity (the desired solution), among all admissible velocities u_i that satisfy the compatibility conditions, incompressibility and the boundary conditions, causes the following π functional to assume a stationary value

$$\pi = \int_V E(\dot{\epsilon}_{ij})dV - \int_{S_v} F_i u_i dS \quad (1)$$

Where E is the work function, which gives $\sigma_{ij} = \partial E / \partial \epsilon_{ij}$. The incompressibility constraint on admissible velocity fields is resolved by introducing a penalized form of the incompressibility in the variation of the functional. Hence, the actual velocity field is determined from the stationary value of the variation as follows,

$$\delta\pi = \int_V \bar{\sigma} \delta \epsilon dV + K \int_V \dot{\epsilon}_v \delta \dot{\epsilon}_v dV - \int_{S_F} F_i u_i dS \quad (2)$$

Where $\bar{\sigma} = \bar{\sigma}(\bar{\epsilon}, \bar{\dot{\epsilon}})$, and $\dot{\epsilon}_v = \dot{\epsilon}_{ii}$ is the volumetric strain-rate. The penalty constant K should be very large positive constant for incompressibility so that

$$\lim_{K \rightarrow \infty} \int_V \dot{\epsilon}_v \delta \dot{\epsilon}_v dV = \lim_{K \rightarrow \infty} \frac{1}{K} \left(\int_{S_F} F_i \delta u_i dS - \int_V \bar{\sigma} \delta \dot{\epsilon} dV \right) = 0 \quad (3)$$

The heat flux generated during the FSE process is caused by the decaying into heat of friction forces work and the plastic deformation work. Temperature variation can be expressed as:

$$k_1 T_{ii} + \dot{r} - \rho c \dot{T} = 0 \quad (4)$$

Where $k_1 T_{ii}$ is the heat transfer rate, r the heat generation rate and $\rho c \dot{T}$ the internal energy rate. Inside the workpiece, the heat generation rate can be expressed as:

$$\dot{r} = k \sigma_{ij} \dot{\epsilon}_{ij} \quad (5)$$

Where k is the fraction of mechanical energy transformed into heat (assumed to be 90%). The remaining part of the deformation energy stored in the body causes microstructural changes such as variation of dislocation density, grain boundaries, phases, etc. The energy balance can be written as

$$\int_V k_1 T_i \delta T dV + \int_V \rho c \dot{T} \delta T - \int_V k \sigma_{ij} \dot{\epsilon}_{ij} \delta T dV - \int_{S_q} q_n \delta T dS = 0 \quad (6)$$

Where q_n is the heat flux across the boundary surface S_q , and

$$q_n = k_q T_n \quad (7)$$

The temperature field has to satisfy the prescribed boundary conditions and the previous equation for arbitrary perturbation. The FEM formulation can be hence expressed as

$$[C]\{\dot{T}\} + [K_C]\{T\} = \{Q\} \quad (8)$$

The theory necessary to integrate the previous can be found in various numerical analysis textbooks. The new temperature is found by the finite difference approximation

$$T_{t+\Delta t} = T_t + \Delta t[(1 - \beta)\dot{T}_t + \beta\dot{T}_{t+\Delta t}] \quad (9)$$

The convergence of the time marching scheme depends on the choice of the parameter β . It is usually considered that β should be larger than 0.5 to ensure an unconditional stability and a value of 0.75 is usually selected.

3.3.2 Model setup

Three different objects were modelled (Figure 3.9): the matrix and the rotating punch were modelled as rigid bodies and meshed with 6000 elements each in order to solve the thermal problem considering heat transfer. The workpiece, representing the compacted chips, was modelled as a unique cylinder. The matrix was fixed in space, while the punch rotated around his longitudinal axe and was plunged into the matrix. The vertical speed of the punch was assigned as a time-dependent law obtained from experimental measurements during force controlled trials. It is worth noticing that this expedient was needed to simulate force-controlled extrusion in order to save CPU time, which can be significantly higher when force controlled boundary conditions are assigned.

The “single-block” workpiece, whose geometry is shown in Figure Fig. 2c is characterized by a mesh of 80000 tetrahedral elements of variable size. The area of the workpiece close to the contact interface with the rotating tool meshed with elements 10 times smaller than the largest one, i.e. about 1 mm in edge.

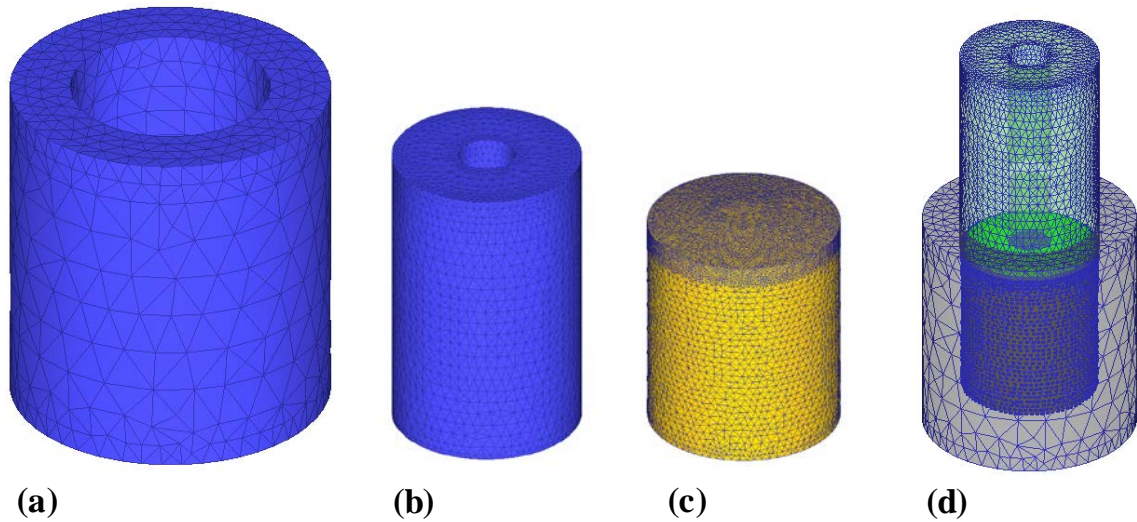


Figure 3.9. Sketch of the model: (a) matrix, (b) rotating tool, (c) compacted chips billet and (d) assembled model highlighting contact nodes.

One of the main issues to deal with during the development of this model was the definition of the material model. The model should take into account the discrete nature of metals chips, considering that it would be extremely time-consuming to correctly model them in their real form. Firstly, the Shima and Oyane formulation for porous material was tested. Metal chips are usually compacted into the matrix before the beginning of the extrusion process due to the action of the tool. This billet of compacted metal scraps can be considered a single porous object, allowing the identification of defects and voids in the extruded wires through the analysis of the relative density variation, namely the ratio between the compacted billet density and base material density. The yield surface implemented by this model is based on a corrected Von Mises criterion that takes into account the presence of microvoids in the material matrix. The formulation is presented in equation 10 where R_0 is the relative density of the porous material (namely of the billet of compacted chips), R is the actual (instantaneous) relative density and Δ_{ε_V} the deformation due to volume

variation of microvoids (whose number does not change according to the base hypothesis of this formulation).

$$A \left\{ \frac{1}{6} \left[(\sigma_x - \sigma_y)^2 + (\sigma_y - \sigma_z)^2 + (\sigma_z - \sigma_x)^2 \right] + (\tau_{xy}^2 + \tau_{yz}^2 + \tau_{zx}^2) \right\} + \left(1 - \frac{A}{3} \right) (\sigma_x + \sigma_y + \sigma_z)^2 = \delta \sigma_0$$

$$A = 2 + R^2 \quad \delta = 2R^2 - 1 \quad R \cong R_0(1 - \Delta\varepsilon_v) \quad (10)$$

The results of preliminary simulations showed that the density of the chips billet rapidly increased to 1 during the very first instants of the process, i.e. before the extrusion process took place. Hence, a rigid-visco-plastic model with Von Mises yield criterion and associated flow rule was used to model the workpiece. This assumption, i.e. considering the material in the die as a continuous metal, is analogous to the one made in [18]. The temperature, strain and strain rate dependent material flow was obtained by both the material database JMatPro demo and in-house experiments. Equation 11 depicts a typical material model for the AZ31 case studies.

$$\sigma = 11.3(-0.19 + \varepsilon)^{0.011} \dot{\varepsilon}^{0.14} \exp(1604.8/T_{abs}) \quad (11)$$

The associated equations are:

$$\bar{\sigma} = \sqrt{\frac{3}{2} (\sigma'_{ij} \sigma'_{ij})} \quad \dot{\bar{\varepsilon}} = \sqrt{\frac{3}{2} (\dot{\varepsilon}_{ij} \dot{\varepsilon}_{ij})} \quad (12)$$

Figure 3.10 shows three different phases of the beginning of the process during which the relative density increases from the initial value of 0.7, experimentally

measured before the process, to the fully shrink state. The density measurements were carried out considering the decreasing height of the compacted chips billet, knowing the mass of the loaded material.

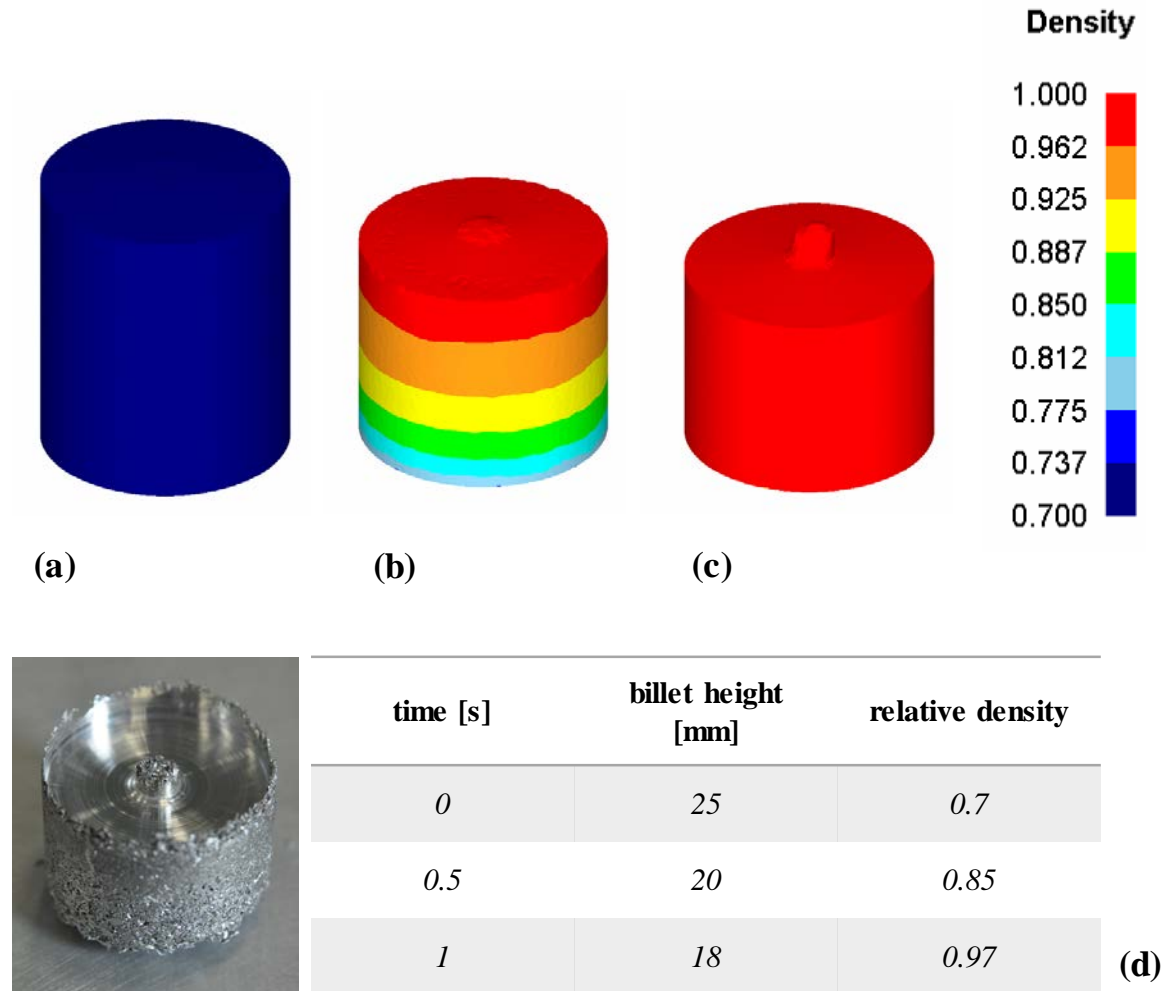


Figure 3.10. Relative density in different stage of compaction: numerical (a) 0 sec, (b) 0.5 sec, (c) 1 sec and experimental measurements (d).

It is worth noticing that the contact area between tool and material to be processed is constituted by a plasticized coherent layer, thus allowing to model the tribological condition at the interface as a common rigid-deformable contact. Constant thermal conductivity and thermal capacity, equal to 96 N/(sK) and 1.77 N/(mm²K), respectively, were used. This assumption linearizes the thermal problem speeding up the simulation. The contact between the tool and the workpiece was modelled through a shear model, with constant friction factor equal to 0.18 and heat exchange coefficient equal to 11 N/(mmKs). These values were obtained during

previous numerical campaigns on FSW of AZ31 [102]. A dedicate DEFORM post-processing routine was developed to calculate the temperature compensated strain rate parameter, i.e. the Zener-Hollomon parameter (Equation 13). The activation energy $Q=135$ kJ/mol for lattice diffusion of the considered material was taken from literature [103].

$$Z = \dot{\epsilon} \exp(Q/RT) \quad (13)$$

3.3.3 Model calibration

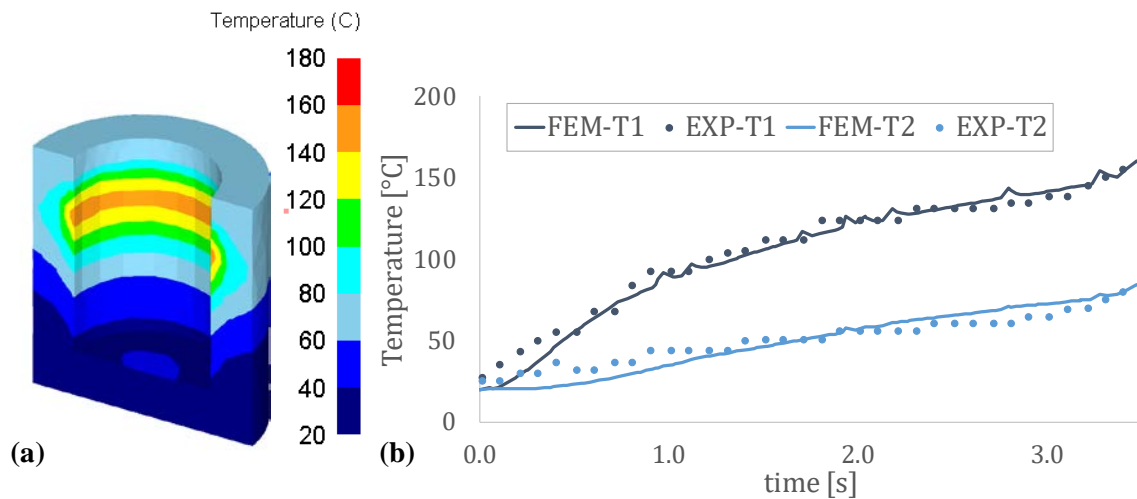


Figure 3.11. (a) Temperature distribution in the matrix and (b) comparison between temperature acquired by thermocouples T1 and T2 and numerical prediction - $R=900$ rpm, $F=14$ kN, $d=5$ mm.

The numerical model was validated against the temperature prediction. Figure 3.11a shows a 3D view of the cross-section of the matrix during the process obtained for the case study characterized by $R=900$ rpm, $F=14$ kN and $d=5$ mm. It can be seen that maximum temperature in the matrix is reached in correspondence of the thermocouple T1, where the predicted value is about 150°C when the extrusion process is activated. The experimental temperature-time curves were compared to the numerical ones obtained by tracking the corresponding location of the thermocouples in the modelled matrix (Figure 3.11b).

It should be observed that, for the above curves, $t=0$ corresponds to the onset of the extrusion phase. This is due to the choice to simulate the process when compaction phase was over, i.e. when the local density of the Shima and Oyane material model was equal to 1 in all the elements of the workpiece. As the accuracy of the temperature prediction is regarded, satisfying agreement is found with experimental data.

3.4 Process mechanics

An experimental campaign [104] was carried out on one of the most common magnesium alloy, AZ31B, in order to investigate the effect of the main process parameter on the extrudates quality and on the unconstrained process variable. Part of this experiment was also used to calibrate and validate the numerical model described in *Paragraph 3.4*. The characteristics of the utilized alloy are summarized in Table 3.1. The raw material was received in plates and milled with no lubricants in order to produce a regular and clean chip. The produced chip has an average dimension of 5 mm length, 2 mm width, and 0.2 mm thickness (Figure 3.12). The experiments whose results are described in that chapter have been carried out with the tooling set #1 (see *Paragraph 3.2.1*).

Table 3.1 Composition and mechanical properties of AZ31B.

YS [MPa]			UTS [MPa]				HV		
150			250				80		
<i>Chemical composition % w/w</i>									
<i>Al</i>	<i>Zn</i>	<i>Mn</i>	<i>Si</i>	<i>Cu</i>	<i>Fe</i>	<i>Mg</i>	<i>Ti</i>	<i>Cr</i>	<i>Ni</i>
3.0	2.0	≥0.20	0.1	0.05	0.005	bal.	-	-	0.005



Figure 3.12. AZ31B milled chip used for the experimental campaigns.

Variable tool rotation, extrusion force and extrusion ratio were used. In particular, three different values were used for each process parameter, namely 300, 500, and 700 rpm for the tool rotation R , 14, 18 and 22 kN for the extrusion force F and 0.2, 0.28 and 0.36 for the extrusion ratio r , i.e. the ratio between the wire diameter and the matrix diameter, corresponding to a final diameter of the extruded wires (d) of 5, 7 and 9 mm, respectively. In this way, a total of 27 different case studies were investigated. Each test was repeated three times and, from each rod, specimens were cut for tensile tests and macrographic analysis.

3.4.1 Extrudate quality

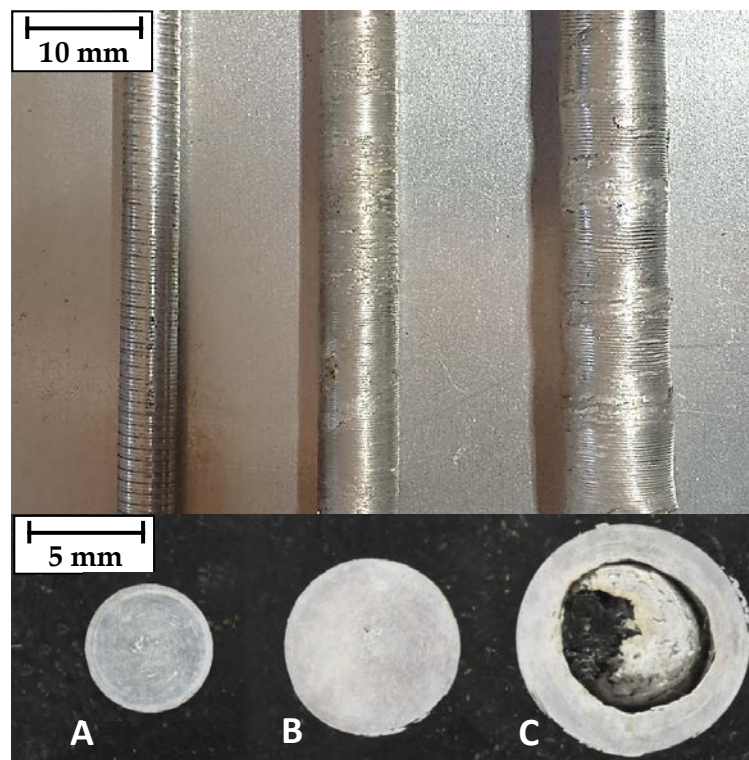
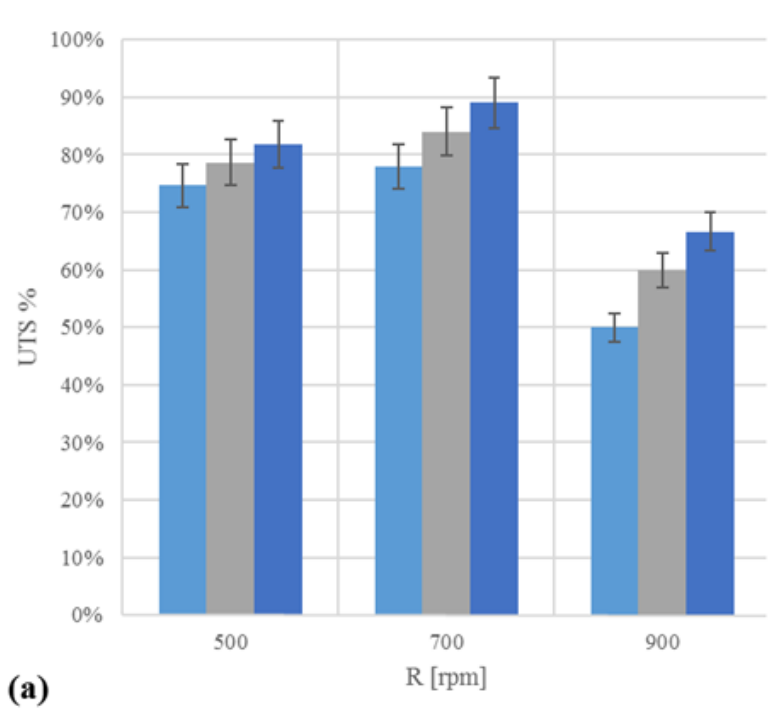


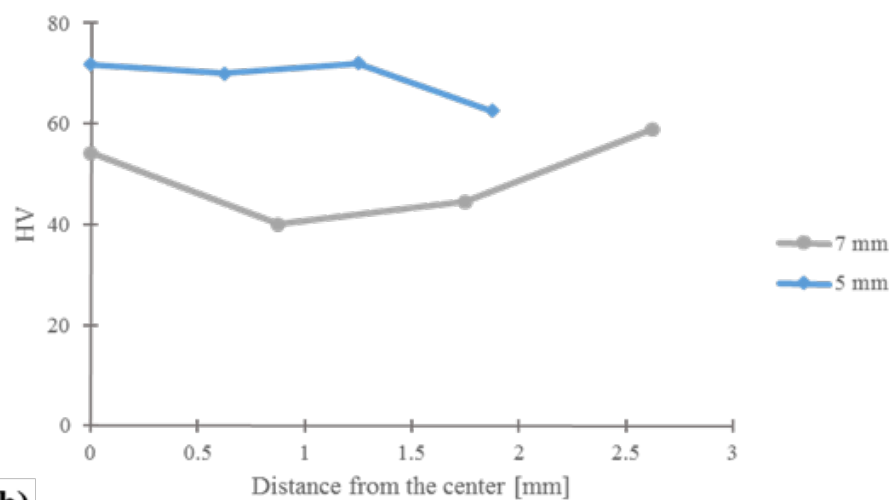
Figure 3.13. Cross section and lateral view of the wires produced with rotation $R=700$ rpm and $F=14$ kN: (a) 5 mm, (b) 7 mm and (c) 9 mm.

A preliminary assessment of the soundness of the produced wires was carried out. Figure 3.13 shows the wires produced with rotation $R=700$ rpm and $F=14$ kN. As it can be observed, cross-section integrity is obtained for wire diameters of 5 mm and 7 mm. On the contrary, a large central void area is observed for the case study corresponding to $d=9$ mm, although the external surface of the wire did not present

any defect. This could be explained considering that larger extrusion ratio results in lower pressure in the extrusion chamber and lower strain in the central area of the extruded itself preventing proper condition for solid bonding to be reached. This aspect will be further discussed analysing numerical results (see *Paragraph 3.5*) and it was found also when different rotation and force were selected, indicating that the extrusion ratio of 0.36 represents a process limit for the analysed force and rotation ranges.



(a)



(b)

Figure 3.14. (a) Extrudes efficiency for the $d=5$ mm ($r=0.2$) case studies and (b) microhardness profiles for the $R=900$ rpm, $F=22$ kN, $d=5$ mm and $d=7$ mm case studies.

As the mechanical resistance of the wires is concerned, efficiency, namely the ratio between the UTS (according to ASTM A931 – 08) of the wire and the one of the base material, ranging between 77% and 90% were obtained for the case studies characterized by wire diameter of 5 mm. UTS% between 55% and 65% was found when $d=7$ mm. Finally, as expected, poor resistance, lower than 20%, was obtained for the $d=9$ mm case studies due to the large voids at the centre of the cross-section. The results for the 5 mm specimens presented in Figure 3.14a highlight that mechanical resistance increases with extrusion force for a given rotation. Additionally, a maximum is observed for the 700 rpm case studies. This results can be explained considering the heat input to the material. On the one hand, temperature increases with tool rotation because of the increased friction forces work. On the other hand, the enhanced material softening produces, for a given constant extrusion force, higher extrusion rate with consequent lower temperature. This phenomenon will be pointed out from the experimental temperature measurement discussed in the following. It is worth noticing that higher temperature assures that proper solid bonding between the chips are reached. Microhardness measurement performed along the radius of the cross section of two different specimens are shown in Figure 3.14b. The analysed profiles were approximately constant and they highlight how the minor extrusion ratio allows obtaining higher hardness thus implying a higher percentage on fine recrystallized grain in the correspondent extrudes.

3.4.2 Extrusion rate

In order to analyse the process mechanics, the tool vertical velocity v was recorded during each test. Figure 3.15 shows the curves, as a function of process time, obtained with $R=900$ rpm and $F=14$ kN, and diameters of 5 mm and 9 mm. The curve obtained for the case study characterized by $d=5$ mm has a similar trend to the ones obtained with $d=7$ mm, i.e. the case studies resulting in sound wires, for all the combinations of force and rotation. The steep increase in the very first seconds

of the process is due to the compaction of the voids between the chips and the beginning of the solid bonding process. When the peak value is reached, the tool velocity starts decreasing. In this phase of the process (phase A in Figure 3.15), the extrusion has begun but the central area of the cross section is still not welded and has a shape similar to the one shown in Figure 3.13 for $d=9$ mm. When phase B begins, the process has reached its steady state, velocity is almost constant and wire integrity is obtained. On the other hand, a completely different trend is observed when $d=9$ mm. In this case phase B, i.e. a steady state value for the tool vertical velocity, is not reached and full consistency of the cross section of the wire is not obtained. It is worth noticing that the above observation allows the analysis of the tool vertical velocity curve to be used as a preliminary assessment of the quality of the final product. It is worth noticing that the void produced in the 9 mm case studies are actually filled with non-coherent metal scrap after the extrusion process took place.

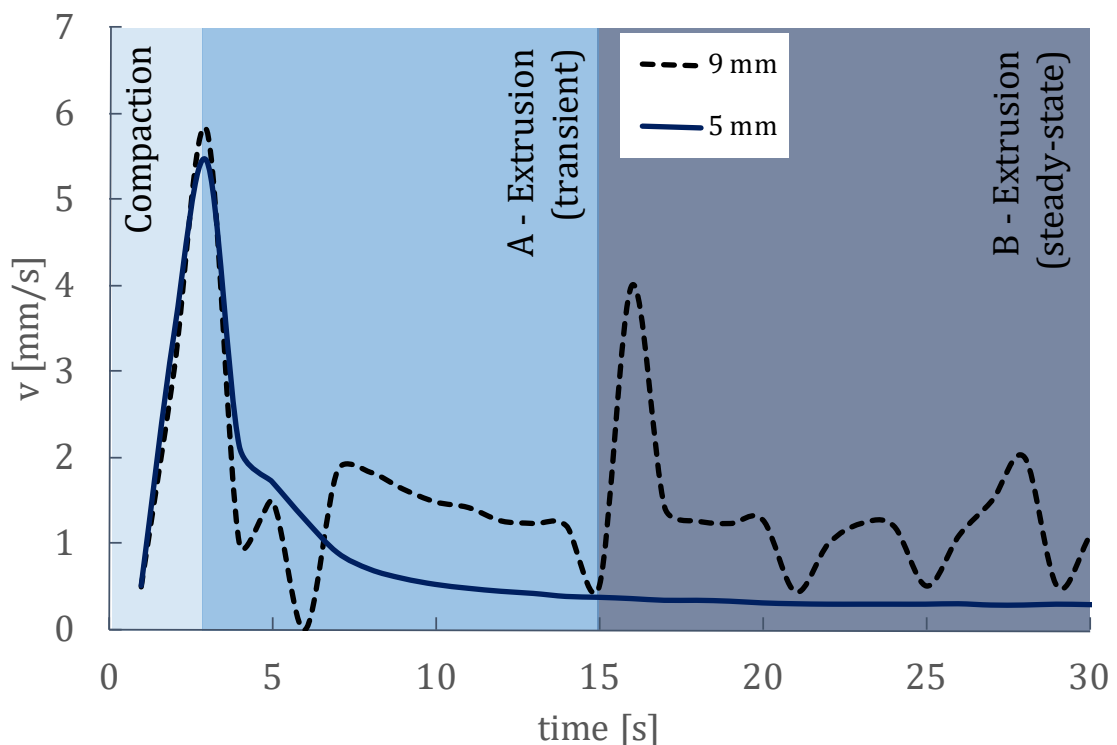


Figure 3.15. Tool velocity vs time for $d=5$ mm and $d=9$ mm - $R=900$ rpm and $F=14$ kN.

The steady state values of the tool velocity v were collected for all the case studies characterized by $d=5$ mm and $d=7$ mm, transformed in wire extrusion velocity V_{extr} through volume conservation, and reported in Figure 3.16. A few observations can be made on the data reported in the figure. First, V_{extr} obtained with $d=5$ mm is significantly larger than the one obtained with $d=7$ mm, in the same process conditions, i.e. with the same rotation and tool force. This result could be expected considering that increasing d from 5 mm to 7 mm results in an increase of the wire cross-section of nearly 100%. Then, when wire diameter and tool rotation are fixed, V_{extr} increases with extrusion force. Also, this behaviour could be expected considering the increase of the heat generated when larger force values are used. Finally, when wire diameter and extrusion force are fixed, a peculiar trend is observed for V_{extr} .

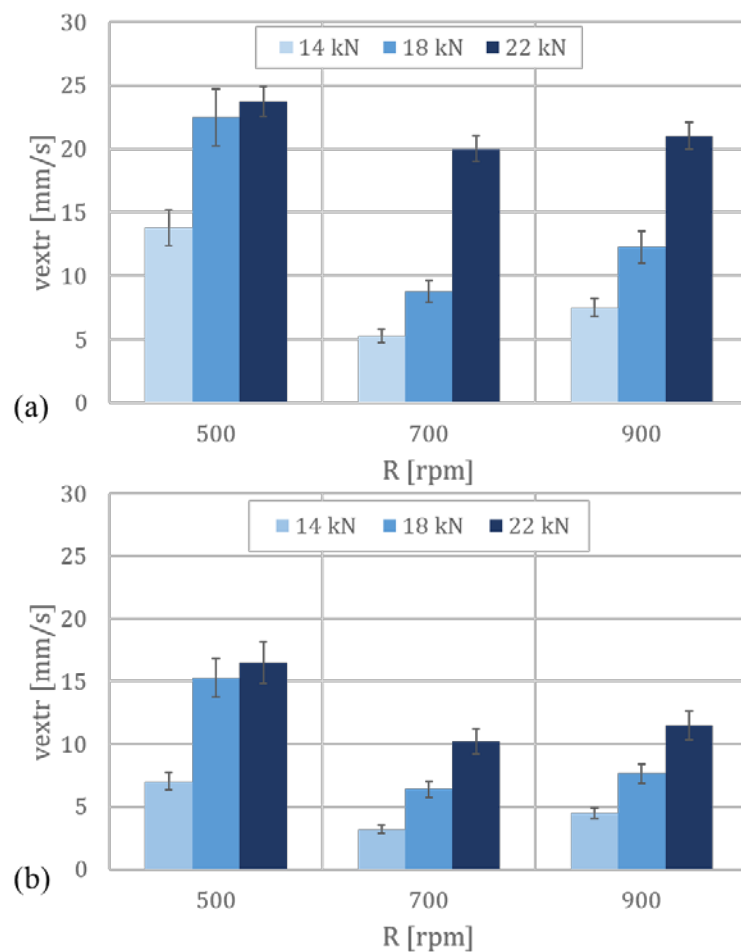


Figure 3.16. (a) Steady State value of the extrusion velocity for the considered case studies: (a) $d=5$ mm and (b) $d=7$ mm.

In particular, a minimum is observed, for all the considered case studies, corresponding to the central value of the tool rotation, i.e. $R=700$ rpm. Two concurrent phenomena take place during the process. It is easy to assume that increasing tool rotation with fixed extrusion force results in an increase of the heat input to the material and, hence, in a decrease of the material flow stress and an increase of the V_{extr} . However, previous research by some of the authors suggested that, based on the significantly distorted grain found close to the periphery of the wires cross section, material rotation may occur, during the process, also in the extrusion channel [27]. In this way, the friction between the extruded material and the extrusion channel of the tool can decrease the extrusion rate of the wire. In order to prove the latter assumption further investigations were needed.

3.4.3 Extrusion temperature

First, temperature in the extrusion chamber was studied. Figure 3.17 shows the maximum temperature acquired by the thermocouple positioned in the extrusion matrix for the case studies characterized by fixed $d=5$ mm and varying tool force and rotation. The concurrent effects of heat input and extrusion rate can be inferred from the trend obtained with varying tool rotation and extrusion force. In particular, decreasing maximum temperature is obtained with fixed tool rotation and increasing tool force, indicating that the increased extrusion velocity previously described for the same conditions plays a predominant role with respect to the increased friction forces work decaying into heat. As the variation of tool rotation is considered, again a specular trend is found with respect to the one shown for the extrusion rate in Figure 3.16a. For a given tool force, a maximum is observed for $R=700$ rpm, due to the increased process time. It is worth noticing that the thermocouple was very close to the bottom surface of the extrusion matrix. In this way, the maximum temperature is reached at the end of the process, i.e. when almost all the initial chip has been extruded.

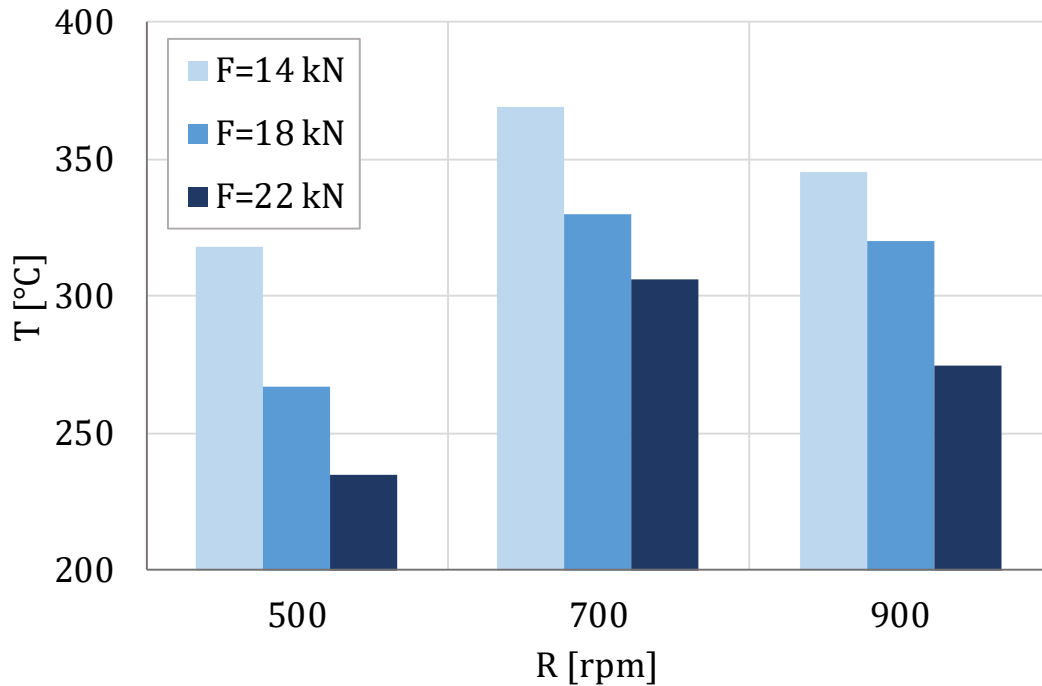


Figure 3.17. (a) Maximum acquired temperatures for the 5 mm case of study.

3.4.4 Material flow tracking

In order to further investigate the effects of the tool rotation on the material flow and the friction between the wire and the extrusion channel surface, a copper marker was embedded in the chip billet. A solid copper wire, 0.7 mm in diameter, was used as a marker and it was positioned in a diametric position with respect to the compacted chip billet (see Figure 3.18a). Several contiguous cross sections of the wire were analysed highlighting the position of the marker. Figure 3.18a shows a typical cross section obtained with $R=500$ rpm, $F=14$ kN, $d=5$ mm.

In Figure 3.18c the subsequent positions of the marker (red areas) in different cross-sections are shown. The distance between the first and the last section in the figure is 5 mm. From the figure, it arises that a helical material flow is generated in the material, which rotates inside the extrusion channel while is extruded from the bottom of the tool to its top.

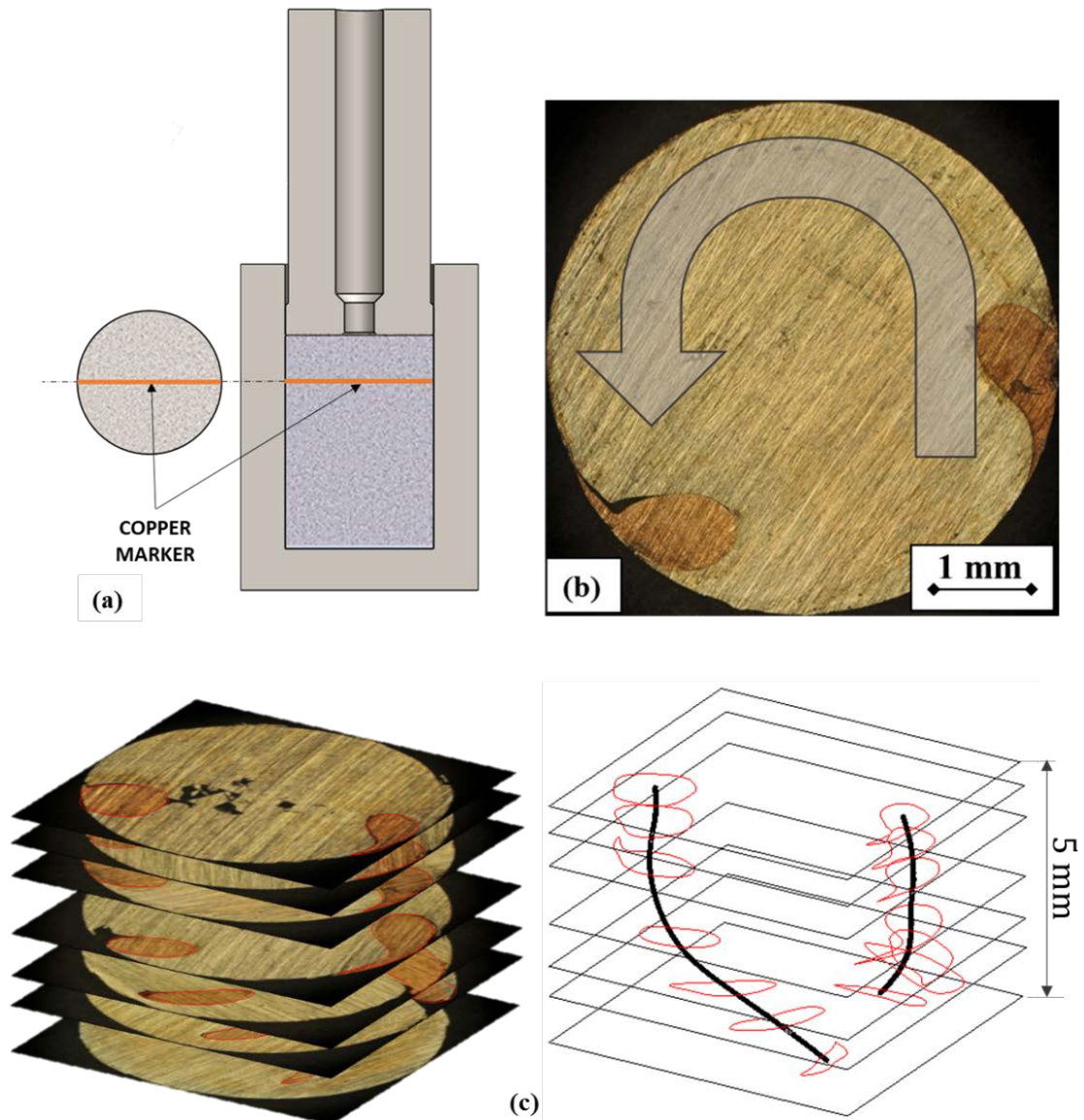


Figure 3.18. (a) Marker position. (b) Initial cross section at the beginning of extrusion channel; the position of the marker is visible. (c) Position of the marker in subsequent cross-sections - $R=500$ rpm, $F=14$ kN, $d=5$ mm.

The developed numerical model was used to quantitatively evaluate the effect of the tool rotation on the material flow and eventually on the extrusion rate. The point tracking option of the considered software was used to study the change in the material flow with varying process parameters. The evolution of the position of the considered tracking points during the process is shown in Figure 3.19 for fixed tool force $F=14$ kN and wire diameter $d=5$ mm and varying tool rotation.

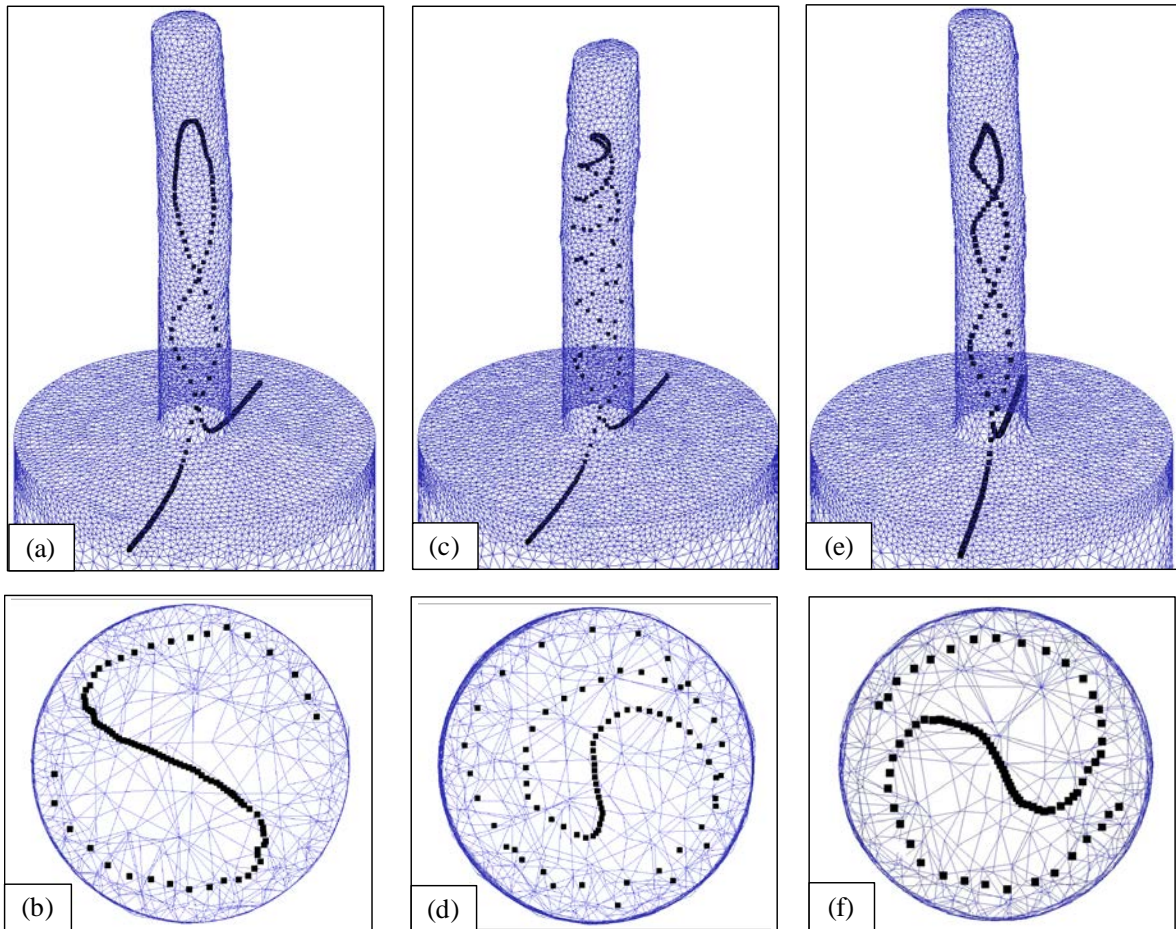


Figure 3.19. Top view and isometric view of the final position of the tracking points for the case studies characterized by (a, b) $R=500$ rpm, (c, d) $R=700$ rpm and (e, f) 900 rpm - $F=14$ kN, $d=5$ mm.

The prediction of the numerical model confirms the helical material flow inferred by experimental observation of the different cross sections of the extruded wire. Additionally, a different behaviour is calculated with varying tool rotation: the helical pitch increases when tool rotation increases from $R=500$ rpm top $R=700$ rpm while decreases when tool rotation increases from $R=700$ rpm top $R=900$ rpm. The latter phenomenon can be explained considering that minimum extrusion rate is obtained with $R=700$ rpm, resulting in increased time during which the material rotates in the extrusion channel. A quantitative analysis of the material flow was carried out tracking the displacement path of a point on the lateral surface of the wire. Figure 3.20 shows the 3D curves obtained for the same process conditions considered in Figure 3.19. The total distance covered by the point inside the extrusion channel was calculated.

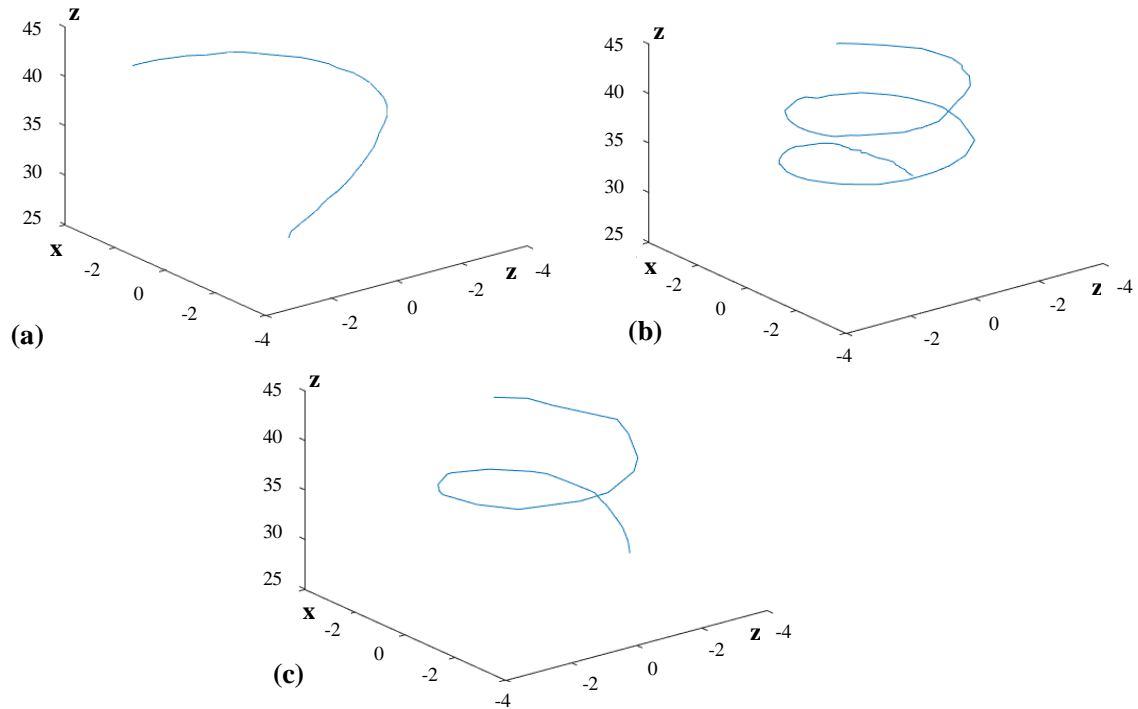


Figure 3.20. Displacement path of a point initially located on the external surface of the wire at the beginning of the extrusion channel: (a) $R=500$ rpm, (b) $R=700$ rpm and (c) 900 rpm - $F=14$ kN, $d=5$ mm.

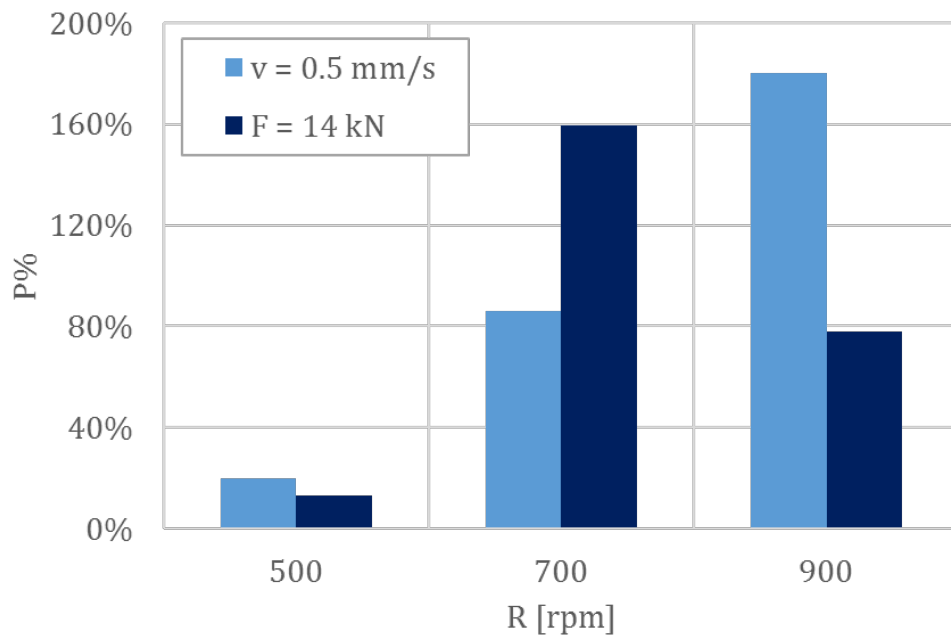


Figure 3.21. Percentage increase in the distance covered inside the extrusion channel with fixed velocity and fixed force.

Figure 3.21 shows the percentage increase (P) in the distance covered inside the extrusion channel with respect to a straight extrusion, corresponding to 14 mm, i.e. with no material rotation. Further simulations were run, with varying rotation, keeping the extrusion rate constant and equal to 0.5 mm/s, with the aim to isolate the effect of the tool rotation on the material flow inside the extrusion channel (light blue bars). It is seen that the distance covered by the tracking point is always larger than the extrusion channel length and p increases with tool rotation, reaching 178% when $R=900$ rpm. The increased distance covered inside the extrusion channel results in an increase in the energy dissipated due to the friction which can decrease the extrusion rate when force controlled process is considered. The latter statement is confirmed by the trend of p for the case of constant force (dark blue bars, $F=14$ kN, $d=5$ mm).

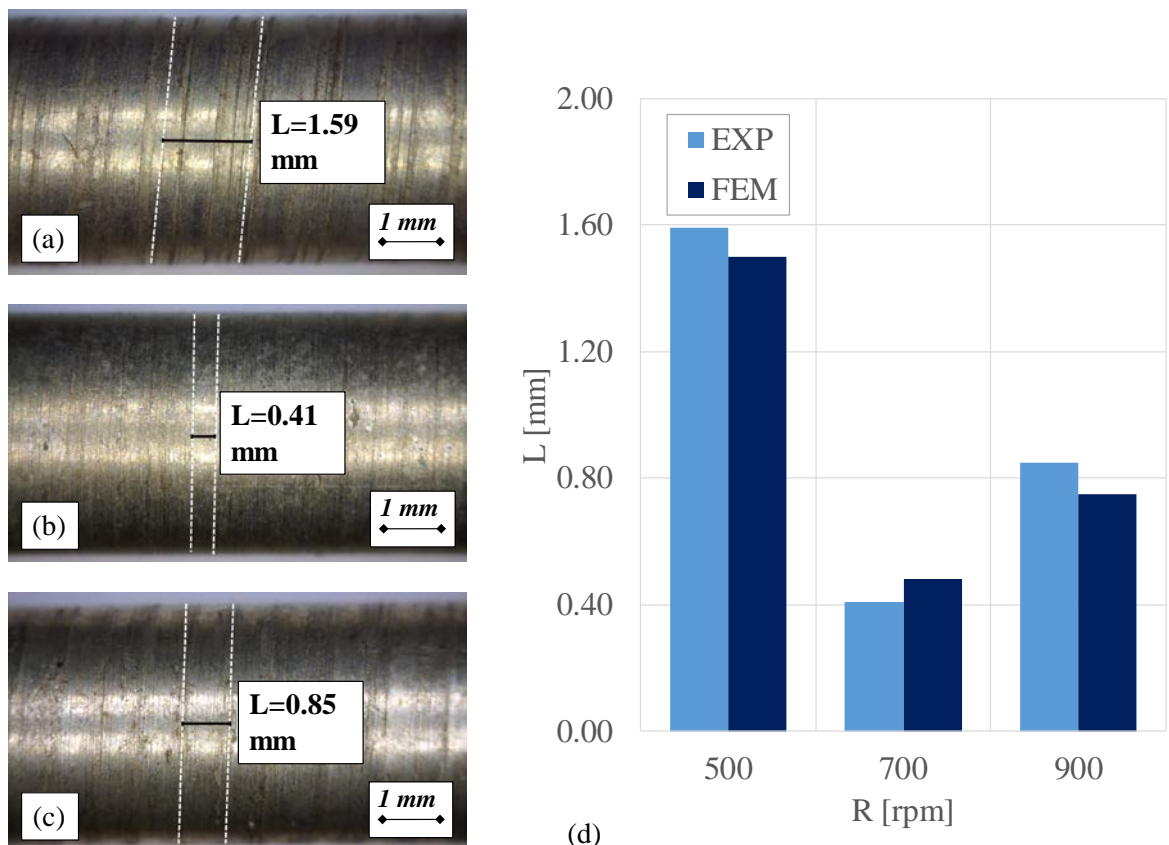


Figure 3.22. Surface macro-roughness for the (a) $R=500$ rpm, $F=14$ kN, $d=5$ mm, (b) $R=700$ rpm, $F=14$ kN, $d=5$ mm and (c) $R=900$ rpm, $F=14$ kN, $d=5$ mm, (d) comparison between experimental and numerical values.

In this conditions, the competition between heat and friction (the first increases with tool rotation while the second decreases) results in a maximum, observed for $R=700$ rpm, explaining the trends of extrusion rate and temperature in the matrix experimentally found.

Finally, the analysis of the surface macro-roughness of the specimens was carried out. A helical groove can be observed in Figure 3.22, with helical pitch (L) following a specular trend with respect to the one of the P parameter, as a function of the rotational speed. The minimum pitch, corresponding to a smoother groove and the best surface finishing, is obtained for the $R=700$ rpm, $F=14$ kN and $d=5$ mm case study. Consequently, surface roughness appears to be directly related to extrusion rate, with slower extrusion resulting in longer distance covered inside the extrusion channel and smoother and more uniform surface quality.

Summing up, the following main conclusions can be drawn:

- ✓ Extrusion rate is highly influenced by tool rotation, extrusion force and extrusion ratio: extrusion rate increases with extrusion force, for a given tool rotation, while it shows a minimum, as a function of tool rotation, when extrusion force is fixed. In-process monitoring of extrusion rate can be used for preliminary identification of incorrect process condition;
- ✓ Experimental observation of the final position of a copper marker indicated that a helical material flow occurs in the extrusion channel;
- ✓ Maximum temperature in the container matrix depends on heat input and process time i.e. extrusion rate: it decreases with constant tool rotation and increasing tool force due to predominant effect of increased extrusion rate over increased heat input. Accordingly, it has a maximum for constant extrusion force and varying tool rotation following the trend of extrusion rate;

- ✓ When constant extrusion rate is applied, the distance covered by the material in the extrusion channel increases with tool rotation; when constant force is applied, the concurrent effect of temperature increase (contributing to increase the extrusion rate) and friction losses increase (due to the covered distance increase and contributing to decrease the extrusion rate) results in a minimum in the extrusion rate;
- ✓ The extrusion rate directly influences the surface quality of extrudes, being the latter higher when lower rate is obtained through the combination of tool rotation and tool force.

3.5 Extrudates integrity and microstructure prediction

3.5.1 FEM model results

Using the experimental data obtained from the experiments on AZ31B magnesium alloy described in the previous paragraphs, the single block" 3D FEM model for FSE was used to predict extrudates integrity and microstructure on their cross section. The effect of the considered process parameters on the temperature distribution in the processed material and in the extruded product was first investigated. Figure 3.23 shows the temperature calculated with fixed tool rotation $R=900\text{rpm}$ and extrusion force $F=14\text{kN}$ and varying wire diameter, i.e. extrusion ratio. A few observations can be made on this figure. First, temperature is quite homogenous in the extruded wire, regardless of the diameter selected. Maximum value is found in the wire and in a thin layer at the contact surface between the tool and the processed material. Then, it is noted that temperature decreases with increasing wire diameter, being about 480°C for the smaller diameter and about 350°C for the larger one. Although the latter value is sufficient to enable material softening and the onset of extrusion, it will be not sufficient to assure an effective material flow, as it will be better highlighted in the following. On the other hand, the average temperature of the material in the matrix increases with increasing diameter, indicating that the extrusion process activates later when $d=9\text{mm}$ with respect to the case studies characterized by a smaller diameter and there is more time for thermal conduction.

Finally, a different distribution is observed at the entrance of the extrusion channel. In particular, a convex shape of isothermal curves is found for the case study characterized by $d=5\text{mm}$, an almost flat curve is found for $d=7\text{mm}$ and a concave shape is obtained for $d=9\text{mm}$. The presence of the colder material at the

centre of the extruded wire at the beginning of the extrusion channel, i.e. where the material solid bonding occurs and the wire integrity is determined, represents an indication of the non-favourable conditions obtained with this set of process parameters, as it will be better discussed in the following.

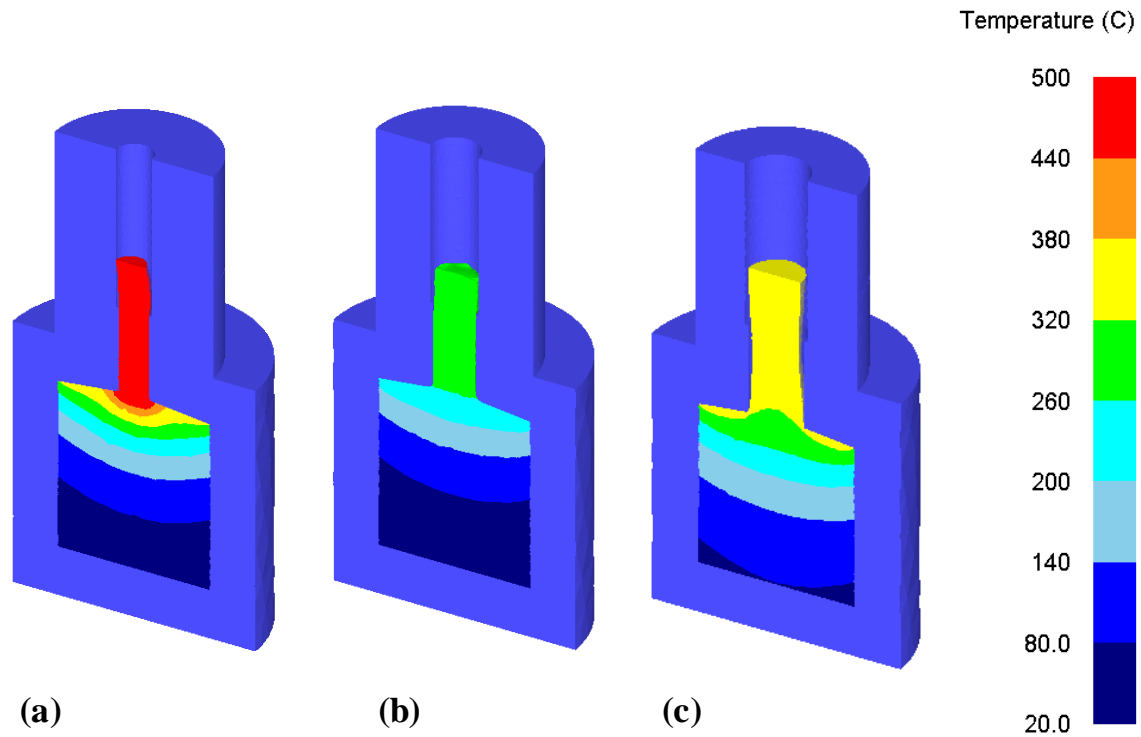


Figure 3.23. Temperature distribution for the (a) 5 mm, (b) 7 mm and (c) 9 mm case studies – R=900 rpm, F=14 kN.

The effect of the extrusion force is shown in Figure 3.24, reporting the temperature distribution calculated using fixed R=900rpm and d=5mm. Although it could be expected that increasing the force on the extruding tool would result in an increased heat due to the larger friction forces work, decreasing temperature is observed with increasing force. This is due to the shorter process time needed, with larger force values, to obtain a given extruded wire length. In particular, Figure 3.24 refers to an extruded length of about 20 mm and a process time of 2.2 sec, 6 sec and 6.2 sec for the case studies characterized by force of 22kN, 18kN and 14kN, respectively.

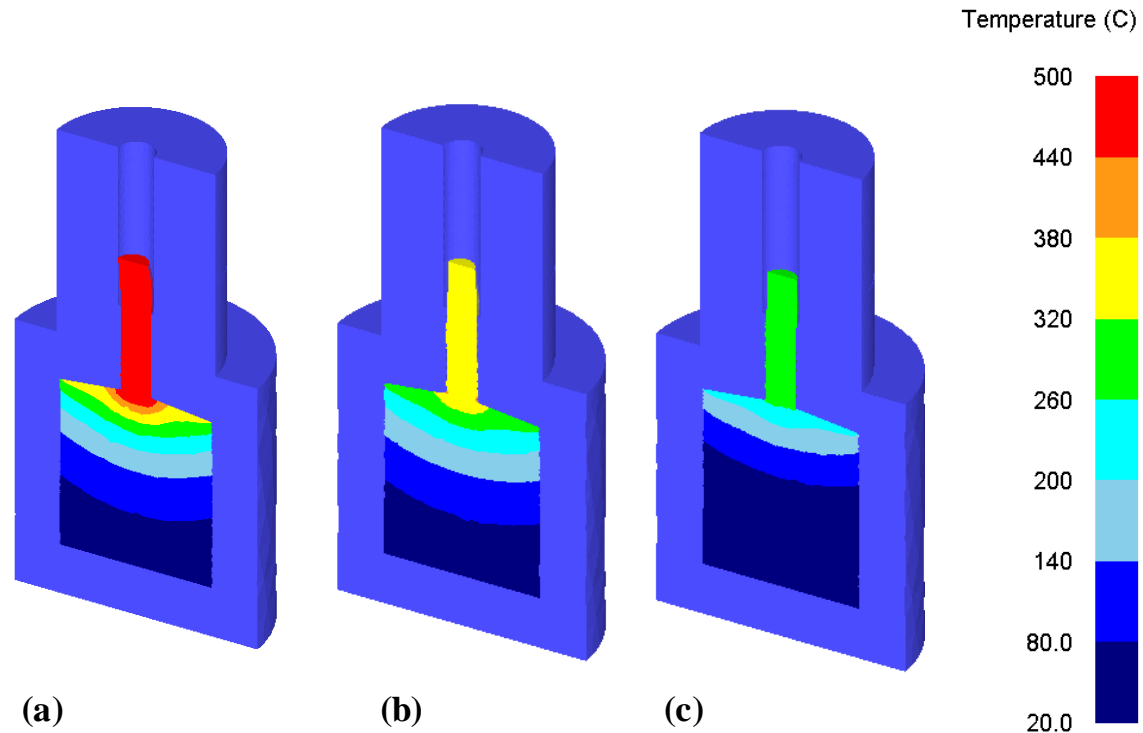


Figure 3.24. Temperature distribution for the (a) 14 kN, (b) 18 kN and (c) 22 kN case studies – R=900 rpm, d=5 mm.

This phenomenon has an impact also on the average temperature in the extrusion matrix, being less time for heat conduction when large force values are considered. Finally, the effect of the tool rotation on the temperature distribution is analysed. In Figure 3.24 the wire and processed material temperature obtained with fixed $F=14\text{ kN}$ and $d=5\text{ mm}$ is shown. From the figure, it is observed that, as expected, temperature significantly increases with increasing tool rotation. It is worth noting that for the coldest case study, shown in Figure 3.25a, the maximum temperature is below 260°C , which is lower than the one observed for the case study characterized by $R=900\text{ rpm}$, $F=14\text{ kN}$ and $d=9\text{ mm}$. However, the former process conditions resulted in a sound wire while, as already mentioned, the latter resulted in a defect wire. This observation suggests that field variables other than temperature play also a key role in the material solid bonding for the creation of solid material from chips.

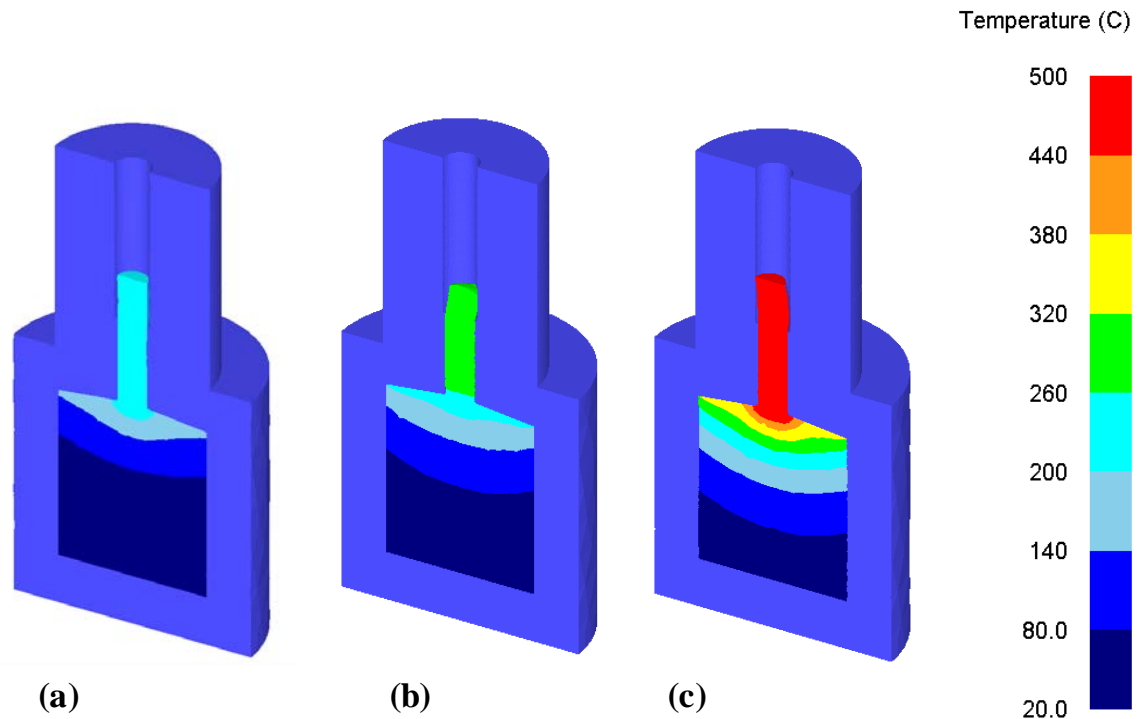


Figure 3.25. Temperature distribution for the (a) 500 rpm, (b) 700 rpm and (c) 900 rpm case studies – $F=14$ kN, $d=5$ mm.

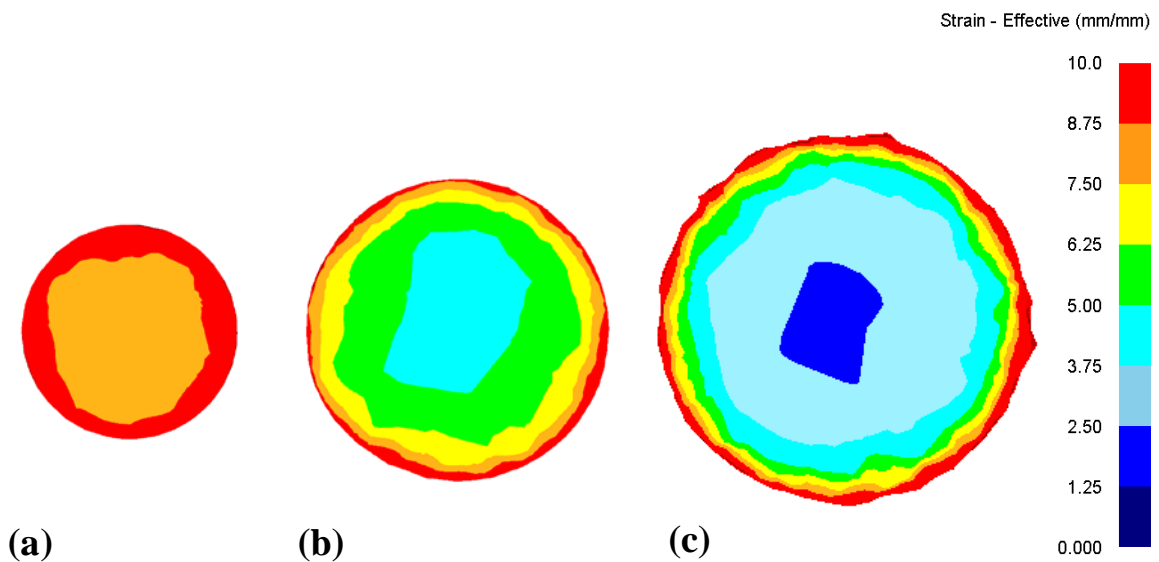


Figure 3.26. Strain distribution in a wire cross section for the (a) 5 mm, (b) 7 mm and (c) 9 mm case studies – $R=900$ rpm, $F=14$ kN.

Based on the above considerations, the calculated strain and strain rate distributions on the cross section of the extruded wire at the beginning of the extrusion channel were analysed. Figure 3.26 shows the strain profiles obtained

with varying wire diameter and fixed $R=900$ rpm and $F=14$ kN. Significantly different profiles are found. First, it is observed that the largest strain values are calculated close to the outer surface of the wire. Although strain decreases close to the wire centre, it remains quite high and close to the maximum value for the case study characterized by $d=5$ mm. On the contrary, as the wire diameter increases, the gradient between the lateral surface and the centre increases, being maximum when $d=9$ mm is considered. For these process conditions, limited accumulated strain is calculated at the centre of the wire. A trend similar to the one found for the effective strain is obtained for the effective strain rate (Figure 3.27). Looking again at the wire extruded with $d=9$ mm, it is noted that a large centre area, larger than the one for which low strain is calculated, is characterized by low values of strain rate. This indicates that material flow in this zone of the wire is less effective than the one taking place in the outer area of the same wire or in the whole cross-section of the lower diameter wires.

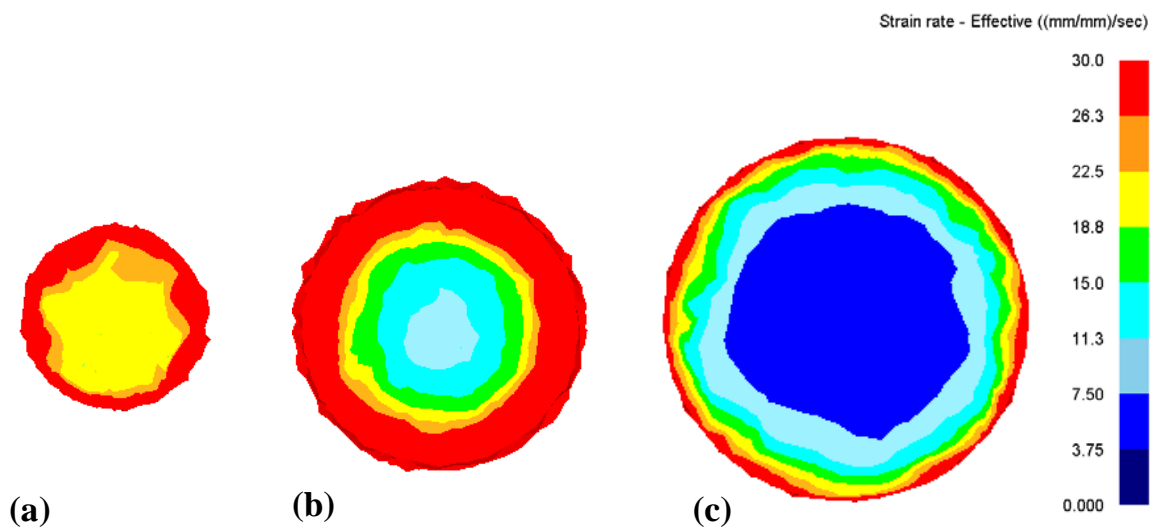


Figure 3.27. Strain rate distribution in a wire cross section for the (a) 5 mm, (b) 7 mm and (c) 9 mm case studies – $R=900$ rpm, $F=14$ kN.

3.5.2 Microstructure prediction

It is known that during solid bonding dominated phenomena the processed material undergoes high levels of strain rate and temperature which enables

microstructural modifications as Continuous Dynamic Recrystallization (CDRX) [105]. The Zener-Hollomon parameter (Equation 13), representing the temperature compensated strain rate, was calculated for the same case study reported in Fig. 9b and 10b and compared to experimental observations (Figure 3.28). Three different zones are found in the wire cross-section. First, close to the external surface of the wire, an area characterized by elongated grain is experimentally observed. It should be observed that this area, labelled as "I" in Figure 3.28, is also the one for which the highest values of strain and strain rate are found.

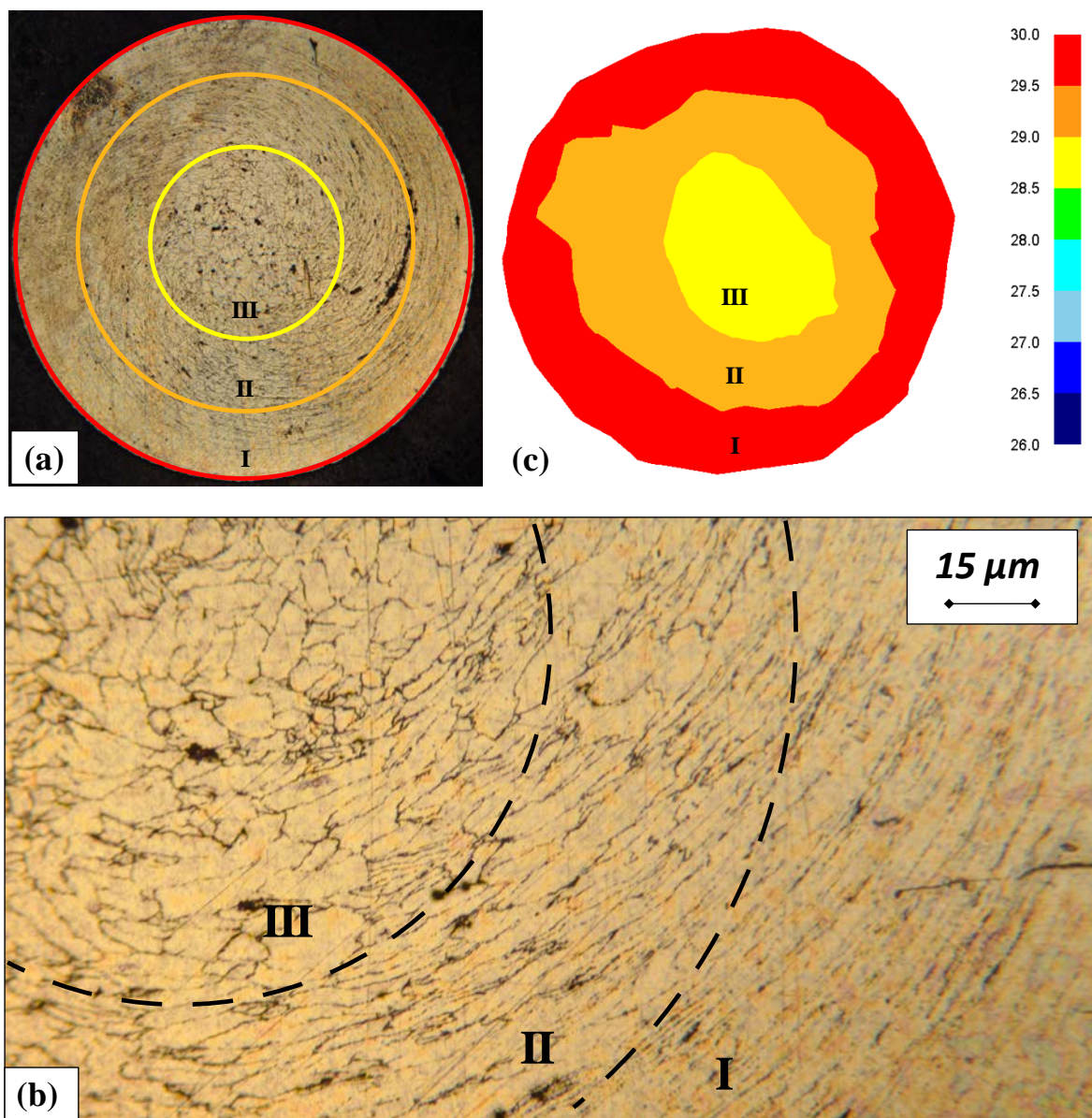


Figure 3.28. Comparison between (a) and (b) experimental micrograph and (c) Zener-Hollomon parameter ($\ln(Z)$) – R=900 rpm, F=14 kN, d=5 mm.

Hence, it can be inferred that the newly formed grains are heavily deformed along their path through the extrusion channel gaining the final morphology shown in the magnification (Figure 3.28b). Moving toward the wire centre (zone “II”), a transition area is found, characterized by less deformed grains. However, the stirring action due to the material flow still results in significant elongation. Finally, in the centre (zone “III”), approximately equiaxial grains, 10 μm in average dimension, are found. It is worth noticing that smaller grain size is obtained with increasing Zener-Hollomon parameter for the considered alloy [103]. In this case, through the gradient of Z is not big between the wire external area and the centre, it can be stated that a difference also in grain size is found between the three areas, being the smaller grain found at the wire periphery. It is worth noticing that, due to small wire diameters considered, the temperature profiles across the diameters are nearly isothermal and the variation of Z is mainly related to the strain rate variation.

3.5.3 Extrudates integrity prediction

In order to predict the extruded wires integrity, the pressure-time welding criterion (Equation 14) was implemented and embedded in the model. According to this criterion, proposed by Plata and Piwnik [106] the integral in time of the ratio between the contact pressure and the flow stress of the material is calculated. If the obtained value exceeds a critical threshold, solid bonding takes place. The criterion has been used in many solid-bonding based processes such as porthole die extrusion, roll bonding and FSW [105] obtaining satisfying results.

$$W = \int_0^t P/\sigma dt \cong \sum_j p_j/\sigma_j \Delta t_j \quad (14)$$

In order to calculate the Plata-Pivnik parameter along the diameter of the extruded wire, a dedicated post-processing routine was developed on Matlab. The routine used temperature, strain and strain rate data extracted from the simulation for a number of tracking points positioned on the diameter of the wires (with a 0.1

mm offset) at the end of the extrusion channel, i.e. when the wire is already produced. The position of these points is tracked down to the beginning of the process (Figure 3.29) allowing to evaluate the evolution of the considered field variables and of the material flow stress. The Plata-Pivnik integral is hence numerically calculated using the trapezoidal rule and considering the mean stress extracted by the previously described point tracking as the contact pressure.

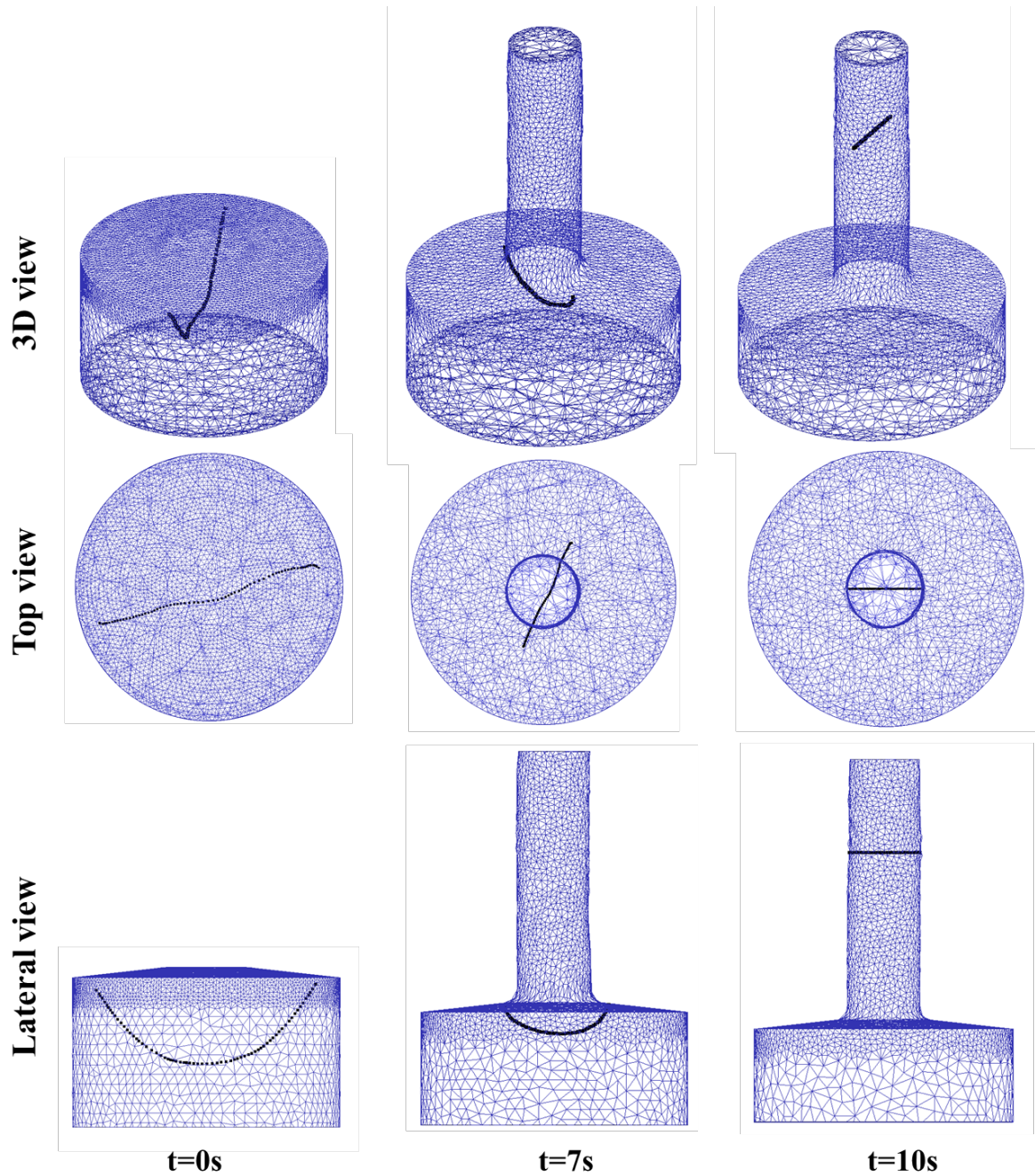


Figure 3.29. Point tracking positions in three different steps: (a) initial, (b) entering the extrusion channel, (c) out of the extrusion channel - R=900 rpm, F=14 kN, d=7 mm.

Finally, the calculated values of W are reported in Figure 3.30 for the three case studies previously taken into account, namely with fixed tool rotation $R=900\text{rpm}$ and extrusion force $F=14\text{kN}$ and varying wire diameter, together with the wire macrographs and UTS values, calculated as a percentage of the base material. In order to more directly compare the results obtained for different diameters, a normalized value was used for the abscissae axis. First, it is observed that a similar trend is obtained for the three case studies. In particular, the maximum value is reached close to the lateral surface of the wire, at a distance corresponding to a range of 70%-90% of the radius rather than on the lateral surface. Then, the W value significantly decreases till the wire centre, confirming that this is the area for which wire formation is more difficult. Looking at the wires macrographs, it is noted that a continuous cross section is obtained when $d=5\text{ mm}$ and $d=7\text{ mm}$ are used. On the other hand, only the external surface of the wire produced with $d=9\text{mm}$ is correctly produced, while in the void central area non-bonded chips can be still observed.

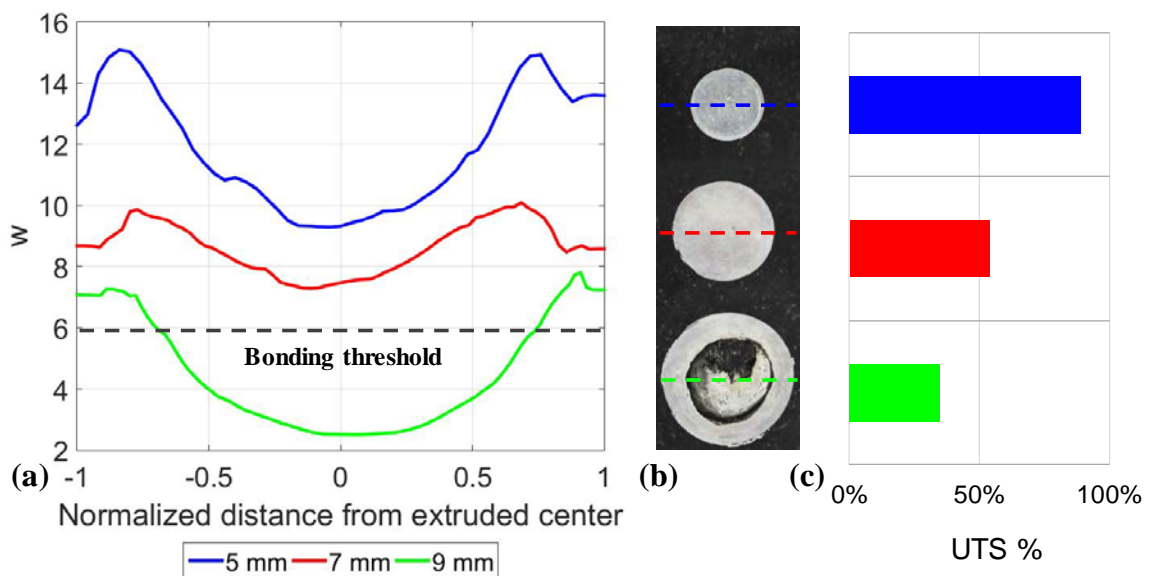


Figure 3.30. (a) W parameter as a function of the normalized diameter, (b) macrographs and (c) UTS% of the produced wires - $R=900\text{ rpm}$, $F=14\text{ kN}$.

The observed trend of the W parameter is in strict correlation with the UTS%, which decreases with increasing wire diameter from a satisfying 90% to less than 40%. The latter value is of course directly influenced by the actual wire geometry, similar to a ring more than to a solid circle. Based on these observations, a threshold value can be identified for the W parameter. Currently, no previous study in literature is known by the author dealing with the threshold values of W for the AZ31 magnesium alloys used in this study.

Hence, the obtained results can represent a first step to identify the threshold value for AZ31 corresponding to $W=6$ (Figure 3.30a). The last finding is consistent with the results obtained for the temperature distribution (Figure 3.23c) and strain distribution (Figure 3.26c). It is worth noticing that a dedicated numerical-experimental campaign is needed to extend the obtained results on the threshold values of the W parameter and quantitatively identify the variation with temperature of this parameter, similarly to what done by some of the authors for AA6061 aluminium alloys [107].

Finally, from the obtained results the following main conclusions can be drawn:

- ✓ Temperature of the extruded wire decreases with increasing diameter, i.e. extrusion ratio. With large diameter values a concave shape of the isothermal curves is found, indicating that colder material enters the extruding channel in correspondence of the wire centre;
- ✓ Wire temperature decreases also with increasing extrusion force due to the lower process time; accordingly, the average temperature in the extrusion chamber also decreases. Temperature increases with tool rotation due to the enhanced action of the friction forces;
- ✓ Strain and strain rate have maximum values in the area close to the lateral surface of the wires. However, only a small difference is observed for small diameter while a large gradient between the lateral surface and the centre is found for large diameters. Very small strain and strain rate values are

calculated at the centre of the d=9mm case study indicating that insufficient material flow took place;

- ✓ The Zener-Hollomon parameter was calculated and compared to the experimental observations allowing the identification of three distinct areas in the wire cross section: the external area, close to the lateral surface, is characterized by small and heavily deformed grains. The transition area is characterized by larger grains for which significant elongation is still visible. The central area is characterized by slightly bigger and undeformed grains, with an average dimension of about 10 μm ;
- ✓ The Plata and Pivnik criterion for solid bonding was implemented and used to predict the produced wires integrity. The results are in good agreement with the experimental observations and allowed the identification of a threshold value of the W value for the considered AZ31 magnesium alloy.

3.6 Material properties influence

An experimental campaign [108] was carried out on AA using tool set #2 in order to investigate the effect of parent material properties on the extrudates quality and on the unconstrained process variable. AA2050 aluminium alloy plate and ingot were used as starting material for FSE. This particular aluminium alloy has been relatively recently developed, offering low density, high corrosion resistance, high damage tolerance and good strength relative to other 2xxx and 7xxx alloys [109]. As cast material and three different heat-treated conditions of wrought plate, O, T3, and T8, characterized by a wide range of mechanical properties were selected for extrusion starting stock, (See Table 3.2). Extrusion billets were cut out of these starting materials using waterjet and subsequent turning in order to fit into the extrusion chamber.

Table 3.2 Chemical composition and mechanical properties of AA2050.

Heat	UTS [MPa]	YS [MPa]	Elongation	HV
Cast	360	190	28%	95
O	250	130	21%	70
T3	480	335	18%	130
T8	550	525	12%	180

Chemical composition % w/w							
Fe	Si	Cu	Mn	Mg	Zn	Li	Ag
		3.2	0.2	0.2		0.7	0.2
0.1	0.08	-	-	-	0.25	-	-
		3.9	0.5	0.6		1.3	0.7

Extrusions were carried out with varying rotational speed (100 rpm, 200 rpm, and 300 rpm) and extrusion force (26.7 kN, 35.6 kN, 44.5 kN, and 53.4 kN). Each experiment was stopped when the length of extruded wire reached about 300 mm (the entire available space to house the extrudate inside the chuck).

Table 3.3 Process parameters.

Experiment #	Material	F [kN]	R [rpm]	Extrudate Status
1	2050-T3	53.4	100	Torque limit reached
2	2050-T3	48.9	100	Sound
3	2050-T3	53.4	200	Hot cracks
4	2050-T3	44.5	100	Sound
5	2050-T3	44.5	200	Hot cracks
6	2050-T3	44.5	300	Hot cracks
7	2050-T3	35.6	100	Sound
8	2050-T3	35.6	200	Sound
9	2050-T3	35.6	300	Hot cracks
10	2050-T3	26.7	100	Sound
11	2050-T3	26.7	200	Sound
12	2050-T3	26.7	300	Sound
13	2050-T8	26.7	100	Sound
14	2050-T8	44.5	100	Sound
15	2050-O	26.7	100	Sound
16	2050-O	44.5	100	Sound
17	2050 Cast	26.7	100	Sound
18	2050 Cast	44.5	100	Sound

3.6.1 Extrudates quality

A complete series of extrusion experiments were carried out only for the T3 heat treatment, while selected case studies were repeated with the other heat treatments and the cast material to compare material behaviour. All the analysed process conditions are summarized in Table 3.3. Specimens were extracted from each extrudate in order to assess material condition through mechanical and microstructural characteristics. Observing the external surface of the extrudates it is possible to make a preliminary assessment of the product quality: higher values of force and rotational speed clearly lead to excessive heat input, causing extensive crack formation (Figure 3.31b-c). It was not possible to analyse the 53.4 kN/100 rpm case study due to excessive torque that overcame machine limits, requiring a decrease in the maximum extrusion force used to 48.9 kN for the 100 rpm case study. Analysing the cross-section of the extrudates a uniform, fine equiaxed microstructure (Figure 3.32b) can be observed in all the “sound” case studies (i.e. the ones not presenting hot cracks on the external surface). The average grain size ranges between 6 μm and 13 μm , with finer grains in the area closer to the external surface of the extrudates.

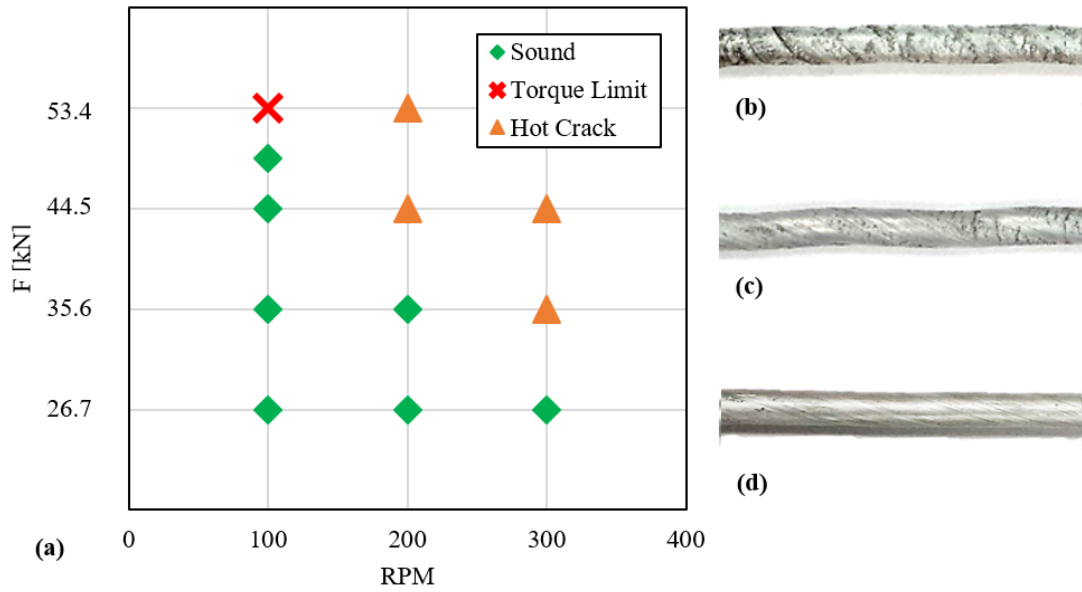


Figure 3.31. (a) Matrix of experiments for AA2050-T3, AA2050-T3 44.5 kN (b) 300 rpm, (c) 200 rpm, and (d) 100 rpm.

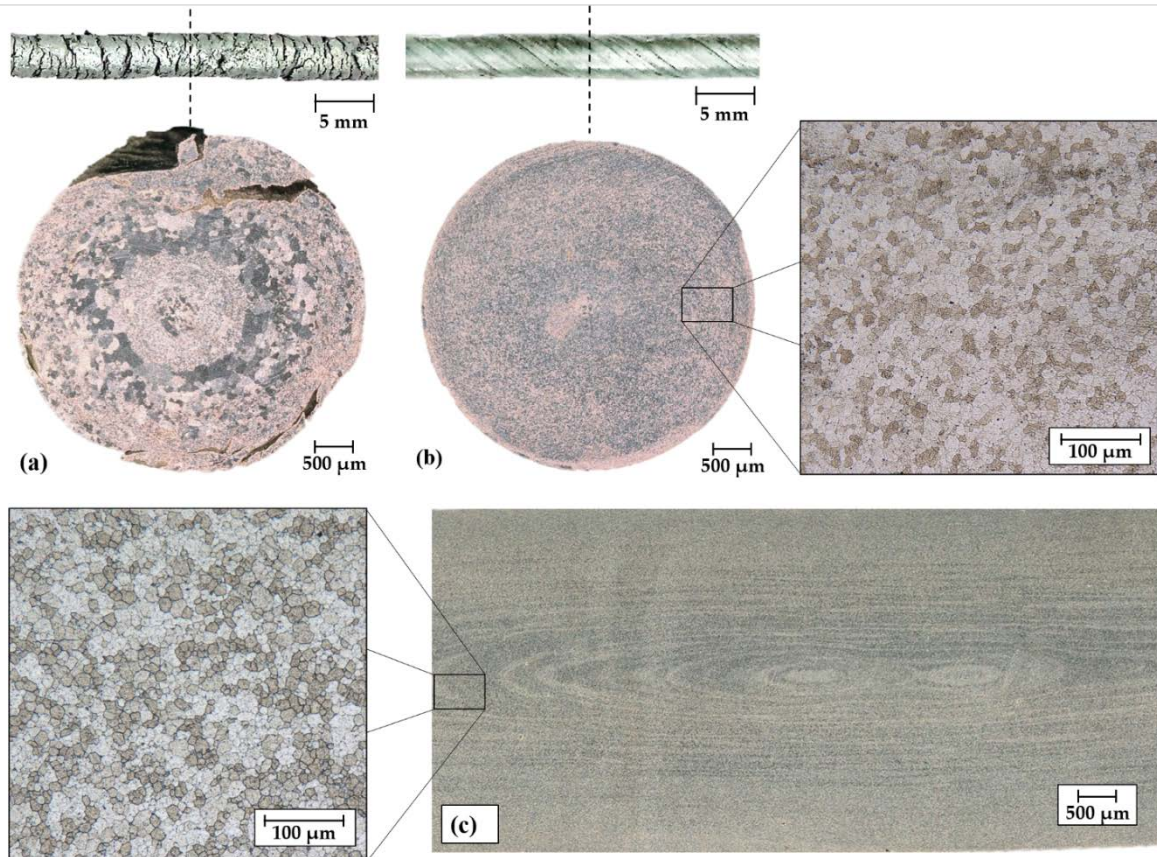


Figure 3.32. Longitudinal view and cross section for (a) AA2050-T3/53.4 kN/200 rpm, (b) AA2050-T3/53.6 kN/100 rpm, and (c) longitudinal section for AA2050-T3/35.6 kN/100 rpm case studies.

This can be explained considering the higher level of deformation to which the material closer to the wall of the extrusion channel is subjected with respect to the centre of the rod as also highlighted by Li et al.[110]. The presence of this peculiar microstructure can be explained by material recrystallization occurring after the extrusion process itself, considering that the longitudinal section of the extrudates shows no significant grain deformation in the extrusion direction (Figure 5a). In the case studies characterized by hot cracking very large grains may be observed in the external part of the samples (Figure 3.32c) with the exception of the areas adjacent to the cracks, which inhibit grain growth.

Table 3.4. Average hardness for different base materials and post-process conditions.

Material	Process parameters	Post Extrusion treatment	Average hardness
2050-T3	Base material	-	130 HV
2050-T8	Base material	-	180 HV
2050-T3	44.5 kN/100 rpm	None	80 HV
2050-T3	44.5 kN/100 rpm	Aged for 16 h at 190°C	100 HV
2050-T3	44.5 kN/100 rpm	Cold worked	120 HV
2050-T3	44.5 kN/100 rpm	Cold worked and aged for 16 h at 190 °C	160 HV

As expected for AA2050, hardness through the cross-section of the extrudates is not correlated with grain size (see Figure 3.33). Mean values of Vickers microhardness of the extrudates are lower than the plate in the T3 condition (130 HV) and no significant variation in extrudate hardness as shown in Figure 3.34a for extrudates produced using 26.7kN and 100 RPM with different starting billet conditions. The T3 condition is achieved by cold deformation after solution heat treatment, which is the likely explanation for the lower hardness in the as-extruded material. The as-extruded material is presumed to be in a nearly solution treated condition but has not been subjected to cold working. The primary reason for cold working of the solution treated material is to provide dislocations, which may act as sites for heterogeneous nucleation of the strengthening T1 phase during subsequent artificial aging: in the absence of such cold working, T1 precipitation can be very sluggish and maximum strength, corresponding to the T8 condition, cannot be achieved [109].

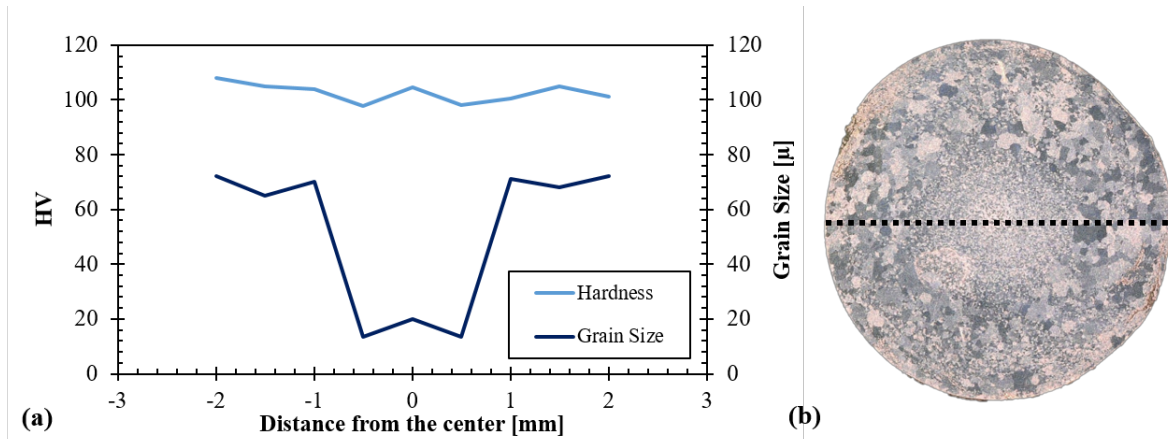


Figure 3.33. (a) Vickers microhardness and grain size measurements along the cross-section (b) of the 48.9 kN, 100 rpm case study.

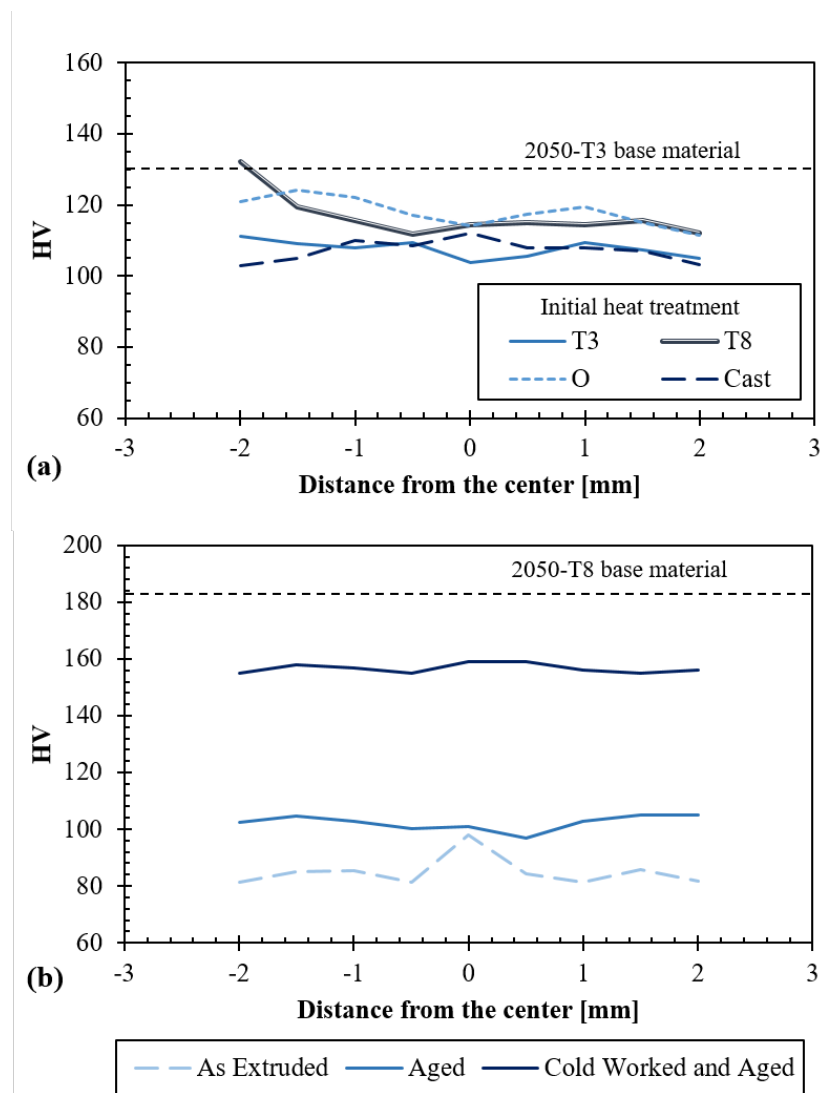


Figure 3.34. Microhardness profiles for (a) the 26.7 kN/100 rpm case studies with different initial heat treatments, and (b) for the 44.5 kN/100 rpm case study and different post-extrusion treatment.

To further understand the condition of the as-extruded 2050 alloy wires, some samples were subjected to artificial ageing both in the “as extruded” condition and after cold working (tensile deformation of about 10%). Figure 3.34b clearly shows the beneficial effect of cold work on the achievable hardness; almost reaching the 2050-T8 hardness level (180 HV).

As far as the tensile resistance is concerned, similar to the hardness, the sound extrudates (i.e. not affected by hot surface cracking) exhibited properties similar to but slightly lower than the T3 plate, (Figure 3.35). These results confirm again the solution treatment and subsequent artificial ageing that the metal undergoes during and after the extrusion process respectively allowing the extrudates to show higher mechanical resistance in comparison to the base material in the case studies characterized by processing of not solution-treated metals such as the O and the cast alloy. Nevertheless, the total elongation of the extrudates resulted to be lower than the base material, even considering the T3 temper.

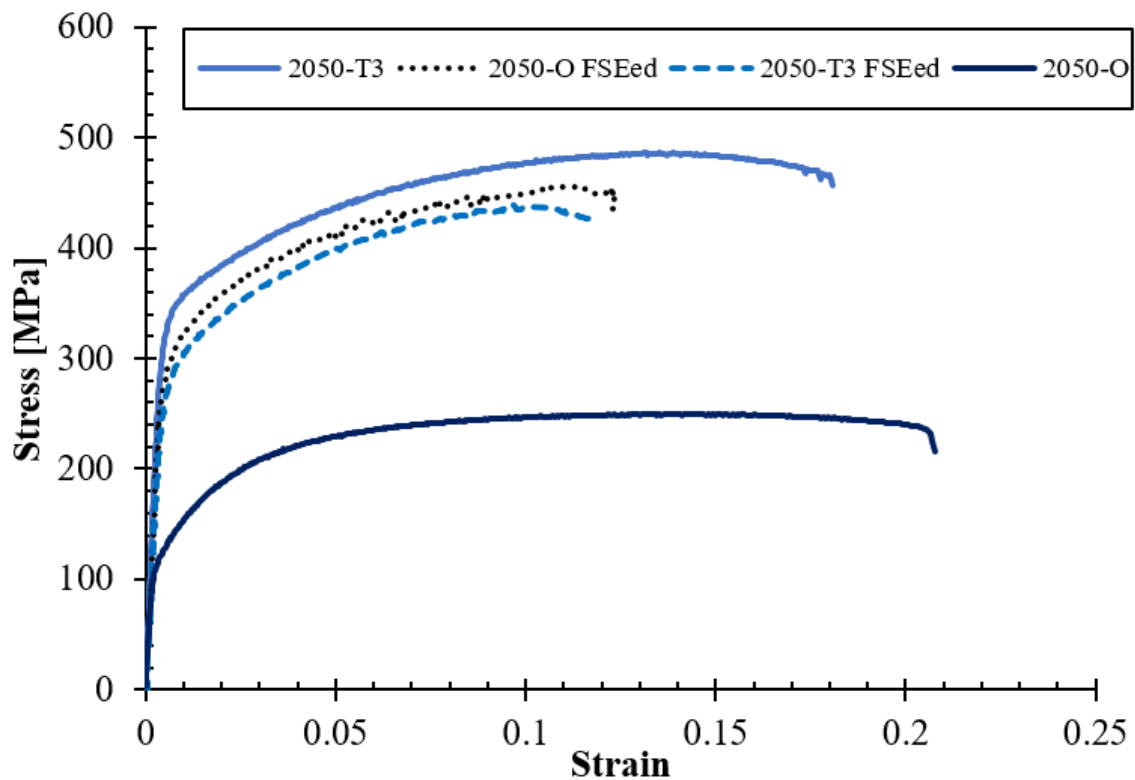


Figure 3.35. Stress-strain curves comparison between extrudates for the 26.7 kN/100 rpm case study.

This can be explained considering the precipitate formation in the recrystallized material acting as obstacles to dislocation motion, reducing the attainable deformation before failure. This effect has to be kept into account since post extrusion annealing may be needed in order to make the most of the material in terms of deformation capabilities for subsequent processing.

3.6.2 Torque analysis

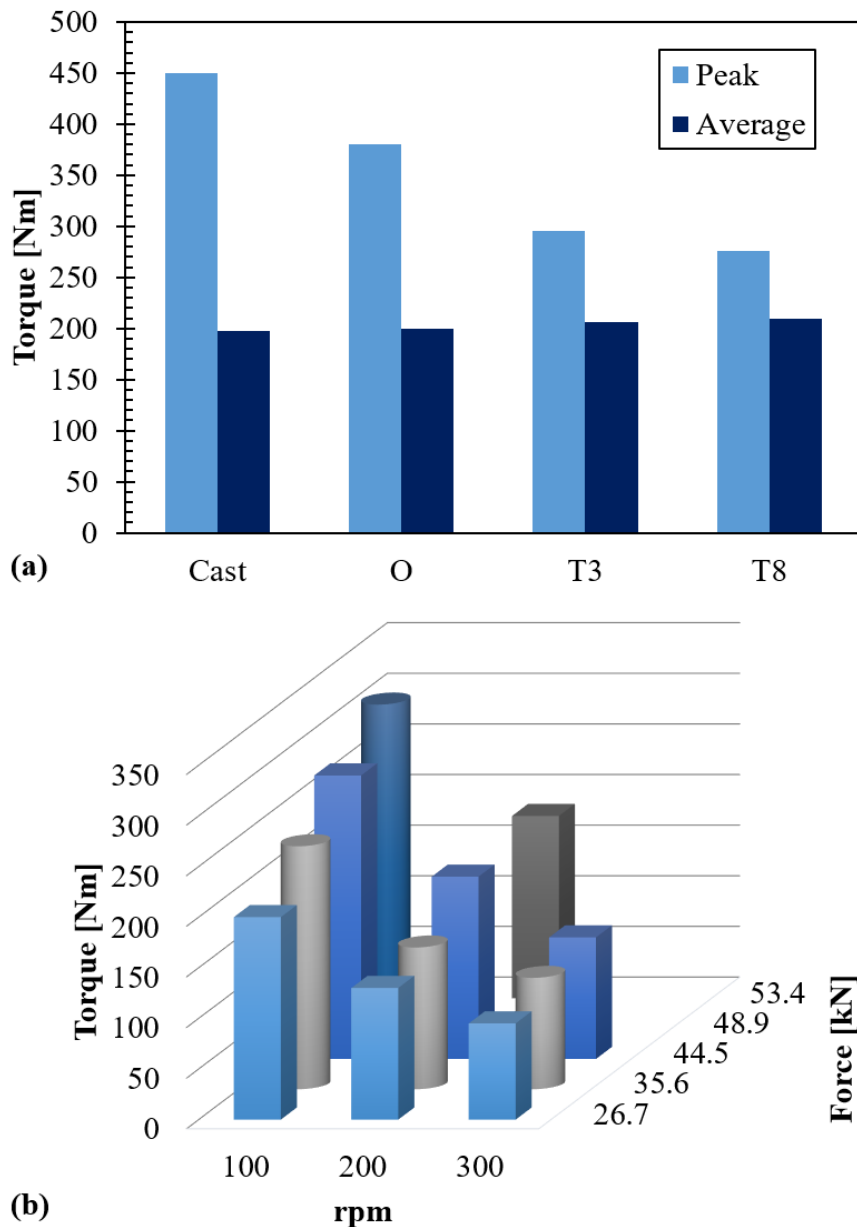


Figure 3.36. (a) Torque measurements for the 26.7 kN/100 rpm case study with different initial base material conditions, (b) torque average values with varying process parameters for AA2050-T3 case studies.

Considering that different sets of parameters allowed to obtain almost the same result in terms of extrudate “quality” and the initial treatment of the base material did not show any strong influence on the final products, it is worth analysing the effect of these variables on other, not controlled, process parameters.

As far as torque is concerned, the initial state of the base material has an important effect. Figure 3.36a shows that Cast and O conditions cause a higher peak torque and slightly lower average values in comparison with T3 and T8 for given process parameters. This can be explained considering the lower hardness of the alloy in the Cast and O conditions that cause the not yet softened material to stick to the die, increasing the torque. Figure 3.36b sum up the average torque values for the T3 case studies with varying force and rpm, showing that it increases with extrusion pressure and decreases with rotational speed. This trend is analogous to the one observed during Friction Stir Welding processes [111]; the increase of the die rotational speed causes the increase of the heat input further softening the material being processed, finally lowering the resulting torque. On the other hand, the increasing of contact pressure increases consequently the magnitude of the friction force resulting in torque.

3.6.3 Extrusion rate analysis

Extrusion Rate was calculated analysing the vertical movement of the die and calculating average material speed in the extrusion channel using volume conservation. The average values (Figure 3.37) increase with increasing rpm and force; thus can be explained considering that both parameters concur to increase the heat input, accelerating material softening and extrusion consequently whilst increased extrusion pressure would, by itself, serve to increases extrusion rate at any given temperature.

No differences were observed processing differently heat treated alloys with respect to die plunge velocity, hence extrusion rate. Process temperature, on the contrary, results to be slightly influenced by process parameters for the sound case

studies; thus can be explained considering the concurrent effect of heat flux generated by friction and the material flow exiting the chamber while extrusion occurs. The higher extrusion rate (i.e. more material being extruded for given time) prevents notable temperature increases in the case studies characterized by higher rpm and forces.

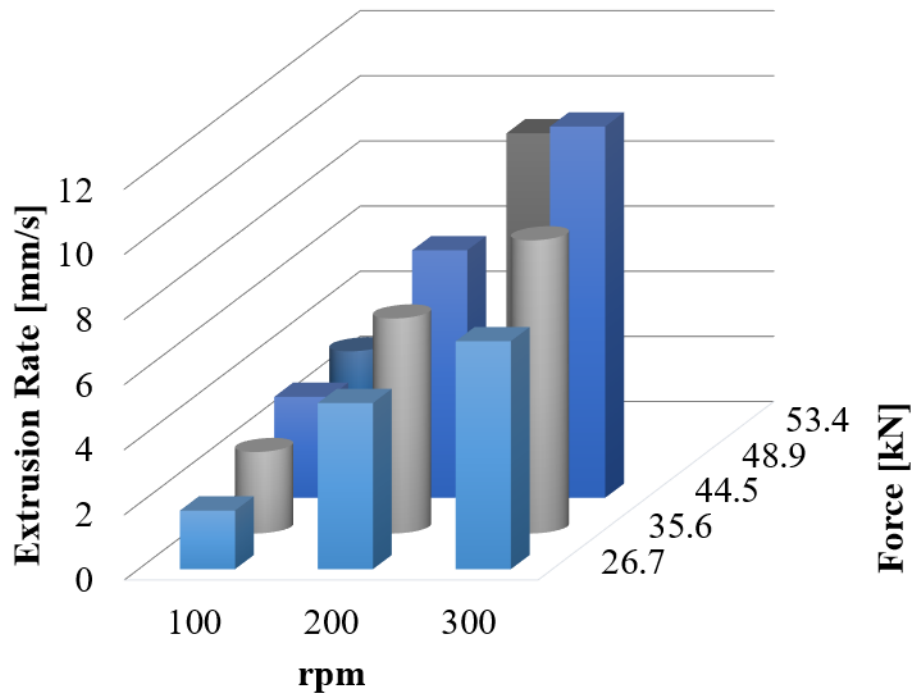


Figure 3.37. Extrusion rate average values with varying process parameters for AA2050-T3 case studies.

It is worth noticing that the low influence of initial temper on the extrudates final properties allows choosing even the cast alloy as a base material, with the only limitation of selecting the best combination of process parameters in order to reduce the peak torque (i.e. low forces and high rpm). Another strategy to reduce the initial torque consist of reducing the force application rate, thus leading the average extrusion pressure in the initial transient phase to be lower than the nominal value.

From the obtained results, the following main conclusion can be drawn:

- ✓ FSE is feasible to process any kind of heat-treated and non-heat treated AA2050 alloy producing sound wires with wide windows of workability.

- ✓ Choosing correctly the process parameters (namely the “sound” case studies), fine equiaxial recrystallized grains can be obtained in the whole cross-section of the extrudates. Excessive rpm and extrusion force cause massive grain growth and hot cracking due to the excessive thermal input;
- ✓ Material recrystallization occurs after the extrusion as evidenced by the equiaxial nature of the grain structure; i.e. no deformation occurs after the final recrystallization process.
- ✓ Microhardness in the cross section is not correlated with grain size and shows that the material being extruded undergoes a thermal treatment that leads to a final condition close to the T3. Further precipitation hardening is limited due to the lack of deformation after extrusion;
- ✓ Peak torque is highly influenced by the base material temper, being significantly higher for softer conditions, while the average torque is independent of starting temper and reaches similar values for given combination of process parameters regardless of starting temper;

3.7 MMC fabrication

As highlighted in the introduction, most solid-state technologies allow producing MMC within the recycling process [112]. In order to investigate the FSE capabilities in that area, experiments have been carried out extruding a mixture of the AA2024 chip and Silicon Carbide (SiC) micro-powder. With 2 μm average size as reinforce. Mechanical and chemical properties of the processed AA are presented in Table 3.5.

Table 3.5 Chemical composition and mechanical properties of AA2024.

YS [MPa]		UTS [MPa]		HV			
110		186		95			
<i>Chemical composition % w/w</i>							
<i>Fe</i>	<i>Si</i>	<i>Cu</i>	<i>Mn</i>	<i>Mg</i>	<i>Zn</i>	<i>Ti</i>	<i>Cr</i>
0.5	0.5	3.8-4.9	0.3-0.9	1.2-1.8	0.25	0.15	0.1

The experiments were carried out on a dedicated FSW machine ESAB LEGIO, with tool set #1 and with varying the percentage of oxide powder added to the initial load (0.5%, 0.75%, 1%, 3%, 5% and 15%). The process parameters for the extrusion (R=700 rpm F=22 kN) were selected during a preliminary campaign that also allowed to fine-tune the tool design with a particular focus on the extension in length of the extrusion channel. The specimens obtained with the different values of p were presented in Figure 3.38. It can be observed that the external surfaces of the extrudates characterized by high percentage of reinforce present deep cracks due to both the increased heat flux caused by the enhanced friction (SiC powders are known to be highly abrasive) and the ineffective dispersion of reinforce itself. The chosen process parameters were first been tested on chips without any added reinforce, to verify the effectiveness of the parameters themselves, allowing to produce a defectiveness reference sample.



Figure 3.38. (a) Extruded wire with varying the added volumetric percentage of SiC powder and (b) detail of the cracks for the $p=15\%$ case study.

The chosen process parameters were first been tested on chips without any added reinforce, to verify the effectiveness of the parameters themselves, allowing to produce a defectiveness reference sample. The whole cross-section of this sample (Figure 3.39a) is characterized by fine equiaxial grains (Figure 3.39b) produced by dynamic recrystallization typically happening during Friction Stir processes.

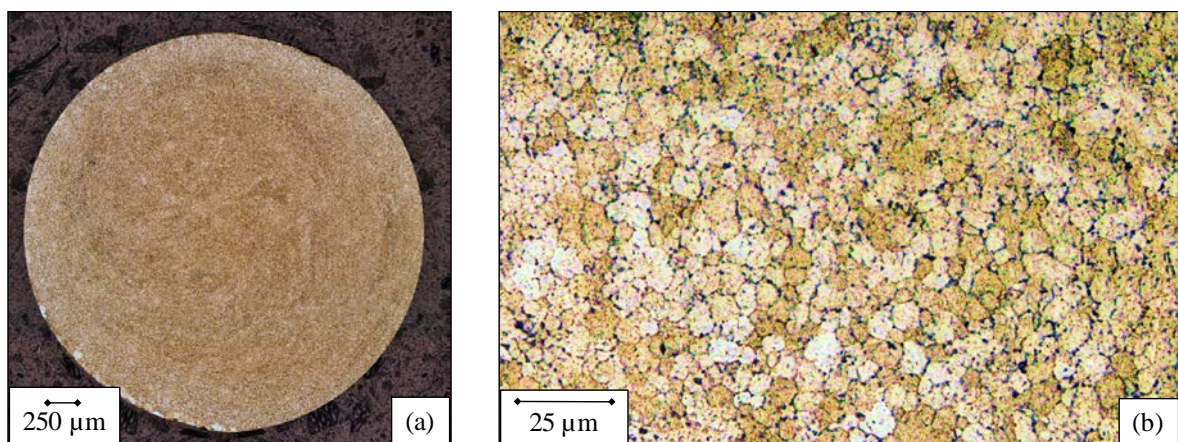


Figure 3.39. (a) Cross-section and (b) micrograph of the $p=0\%$ case study.

When a proper amount of reinforce is introduced into the plastic flow occurring during the extrusion, the carbide particles are dispersed between the grain boundaries (Figure 3.40b), the grain size slightly increase due to grain growth prompted by the higher thermal input while the microhardness sensibly increase far above the base material state (Figure 3.40c). Increasing p the carbide powder starts conglomerating themselves forming incoherent groups on grain boundaries that can become real defect (Figure 3.40d-g) causing the formation of cracks immediately after extrusion, as already observed by preliminary observation of the specimens external surface.

In the case studies characterized by $p > 1\%$, microhardness profiles result to be particularly discontinuous due to the presence of the reinforce conglomerate. It is worth noticing that the shape of this defective areas result to be caused by the helical flow inside the extrusion chamber predicted by the numerical model and visualized using the point taking option (Figure 3.41). The reinforce appears to gather itself in the boundaries of the metal flows uprising the extrusion channel, preventing an effective bonding between them

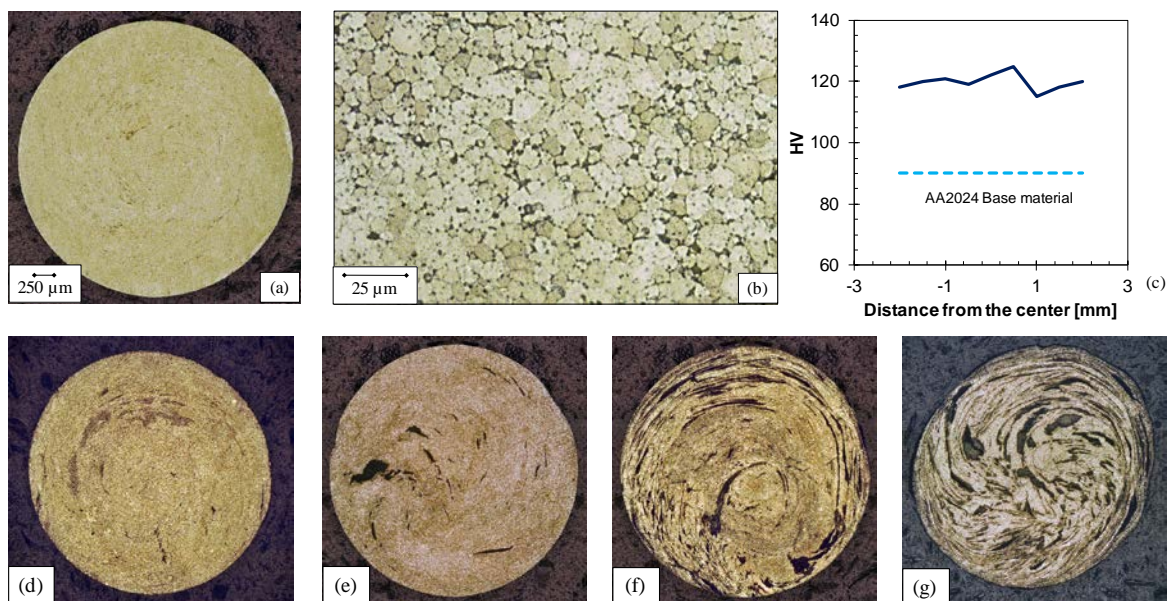


Figure 3.40. (a) Cross section, (b) micrograph and microhardness profile (c) of the $p=0.5\%$ case study, cross section of the (a) $p=1\%$, (b) $p=3\%$, (c) $p=5\%$, (d) $p=15\%$ case studies.

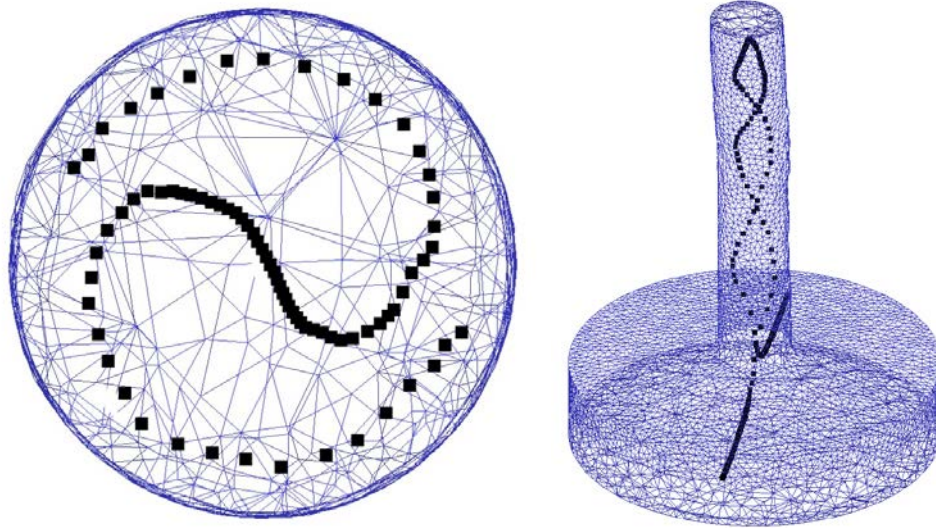


Figure 3.41. Numerical simulation of material flow during the extrusion.

Based on the obtained result, the following main conclusions can be drawn:

- ✓ Solid state recycling through Friction Stir Extrusion is feasible on aluminium alloy AA2024 chips and enables the production of defect-free extrudes;
- ✓ The introduction of SiC powders allows the production of MMC using FSE process;
- ✓ An excessive amount of reinforce ($p > 1\%$) causes the formation of big intergranular conglomerates that affects deeply extrudes quality, causing crack opening and non-uniform mechanical properties;
- ✓ A helical material flow was found through numerical simulation reflecting the spiral shape of the conglomerates of specimens' cross-sections.

Future developments include the quantitative study of the combined effects of the main process variables, i.e. tool rotation, tool force and extrusion ratio on extrudes quality and mechanical resistance. The influence of reinforce grain size and chemical composition have to be taken into account. Finally, temperature measurements should be carried out in order to evaluate the influence of reinforce powder on heat production through friction during the process.

3.8 Process Energy Demands

As already highlighted in the introduction, environmental impact characterization of most direct recycling processes is yet to be well evaluated and standardized. In order to assess the impact of the FSE process and compare it to other recycling strategies, energy consumption measurements have been carried out on the ESAB welder during FSE of AA6060 machining chips with toolset #1. It is worth pointing out that although the used machine was not specifically designed for FSE processes, it is a quite dedicated machine as both FSE and FSW processes use the same main friction based principle enabled by a tool rotating. The experimental measurements allowed to quantify the primary energy demand characterizing such recycling strategy, which was hence compared to ECAP based as well as to conventional recycling processes through LCI analysis [113].

3.8.1 System boundary and major assumptions

Three different recycling routes are considered for comparison, namely: conventional (remelting based), ECAP based and FSE based. Since FSE is particularly suitable for wire production, the production of 1 kg of AA 6060 aluminium alloy was selected as a functional unit. In the ECAP based route, chips cleaning and compaction steps are considered prior to the actual ECAP extrusion step. The severe deformation characterizing the process, enable oxides layers breaking and solid bonding activation. Concerning the remelting approach, the chips are collected and melted together to get the desired alloy, extrusion, and wire drawing steps are envisaged to get the proper workpiece.

A closed AA6060 recycling loop was considered for all the routes, avoiding down-cycling or compositional corrections during melting. The selected system boundary is depicted in Figure 3.42 where all the process steps accounted for as well

as the material flows are highlighted. It can be noticed that process scraps were taken into account and were considered as part of a new recycling phase. The impact of permanent material losses occurring during remelting was considered by adding the same amount of primary aluminium in the model. The primary energy was considered as a metric to compare the different process routes. The processes electric energy demand was converted into (primary) energy source consumption by considering an average efficiency of 34% to account for the energy generation and the transmission losses.

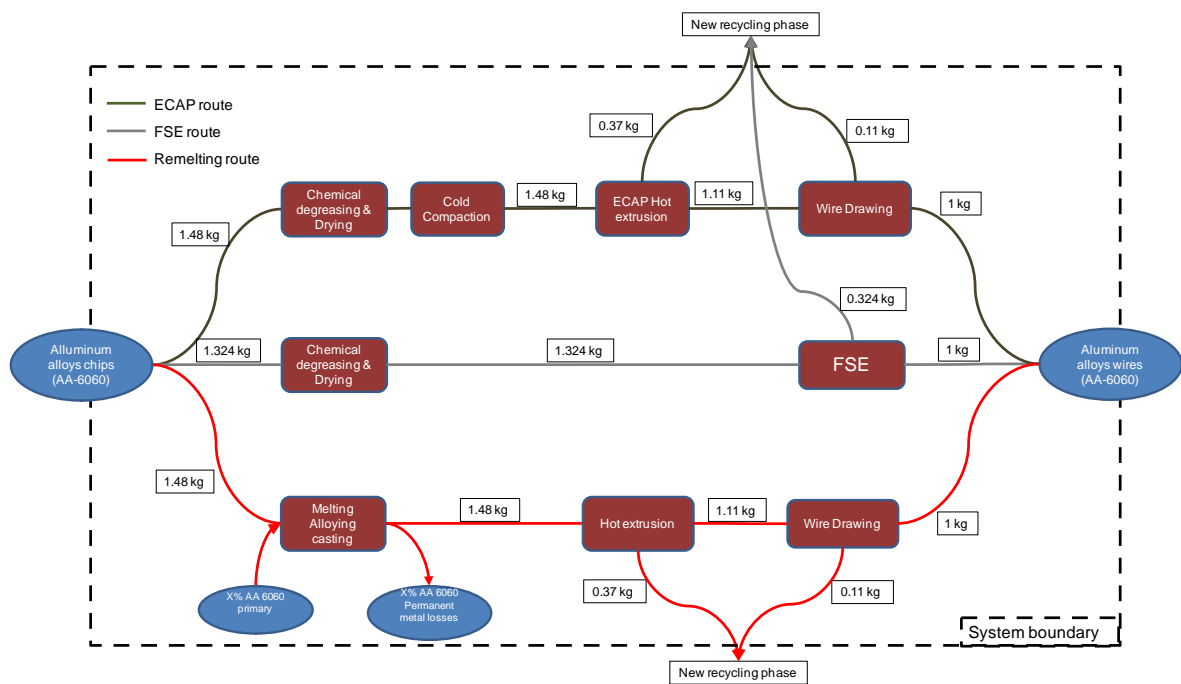


Figure 3.42. System boundary with considered processes and material flows highlighted.

3.8.2 Life Cycle Inventory

Apart from the electrical energy of the FSE process, which was experimentally quantified, the other inventory data were selected from both scientific papers and dedicated databases. The EAA environmental report [16], as well as the paper from Duflou et al. [28], were used as primary LCI sources. The process material yields were found in the EAA report and in CES Edupack [114] for the hot extrusion and the wire drawing processes, respectively. As far as the FSE is concerned, there are no available industrial data about material yield; considering the straightforward

similarity with conventional extrusion processes, the same material yield was assumed in the present study. Since the Mg content of the scrap is expected to become half or less after remelting, such loss was compensated by adding 0.3% wt of pure Mg [101]. The main LCI values alongside the consulted references are reported in Table 3.6.

Table 3.6 Main LCI data and sources.

	Primary specific energy [MJ/kg]	Reference
Cleaning	8.1	[115]
Cold Compaction	8.8	[28]
ECAP hot extrusion	12.8	[16,28]
FSE	23.5	Experimentally measured
Hot extrusion	10.7	[16]
Primary Production AA-6060	210	[114]
Wire drawing (AA-6060)	17	[114]
Melting and casting	7.6	[16]

3.8.3 Power measurements

Concerning the electric energy characterization of FSE, the Fluke 435 power quality analyser was used to measure tension, current, and power over process time. The Power profile of the whole working to produce 0.03 kg of aluminium alloy wire depicted in Figure 3.43.

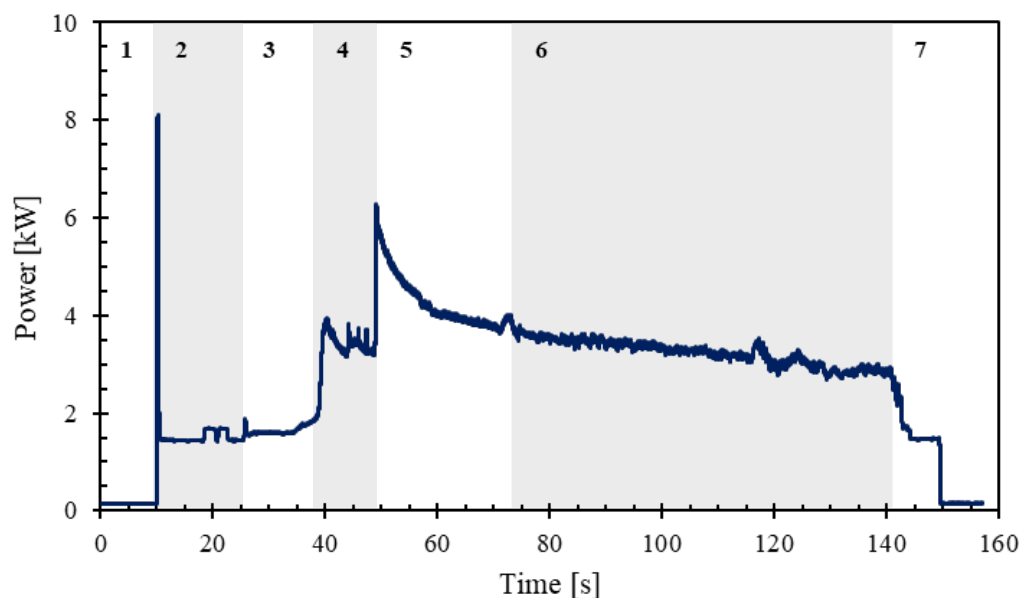


Figure 3.43. Power trend for FSE recycling.

Four different power levels can be noticed, corresponding to different production phases. In Figure 3.43 seven different production phases are highlighted, an explanation of these phases follows:

1. Machine switch/on
2. Hydraulics on/ Stand-by mode
3. Spindle on and first plunging phase (0.5 mm/s, position control)
4. Switch to force control (5 kN)
5. Force increase to extrusion value (18 kN)
6. Extrusion phase
7. Spindle stop and hydraulic off

For the present study only phase 4, 5 and 6 have been considered for quantifying the electric energy demand for wire production, other non-productive production modes were left out for lack of industrial time studies.

3.8.4 Energy demands comparison

The results of the developed comparative analysis are reported in Figure 3.44. For each analysed recycling route the contribution of each process step/factor, towards the total demand, is highlighted. An intermediate scenario with 15% material losses is reported (with the corresponding variation for the 10% and 20% losses scenarios), to get this share of permanent losses a briquetting step to compact scraps is to be implemented. It is possible to see that both SSR processes outperform conventional remelting based route. This is mainly due to the avoided permanent material losses. In fact, in terms of pure processing energy, the conventional route would demand less energy with respect to SSR processes. It is worth pointing out that FSE based route is the most energy efficient for the analysed case study; as a

matter of facts, FSE enables the primary energy demand to be reduced by 53% and by 33% with respect the remelting and the ECAP route, respectively. The energy reduction, characterizing the FSE process is due to the absence of the wire drawing step which is an energy-intensive one. In fact, if the drawing process is left out of the comparative analysis, FSE as ECAP route primary energy demands are very close to each other. In addition, the variability of the data characterizing the eco-properties (Embodied energies for material production as well as processing energies values) of materials and processes [3], does not allow a more general and clear identification of the most efficient SSR process. Is it worth noticing that the above mentioned advantage for both the SSR case studies refers to a permanent aluminium losses of about 15%. Depending on the adopted remelting strategies that value may vary from 10% to 20%, causing the overall evaluation of the primary energy to vary accordingly as shown in Figure 3.44.

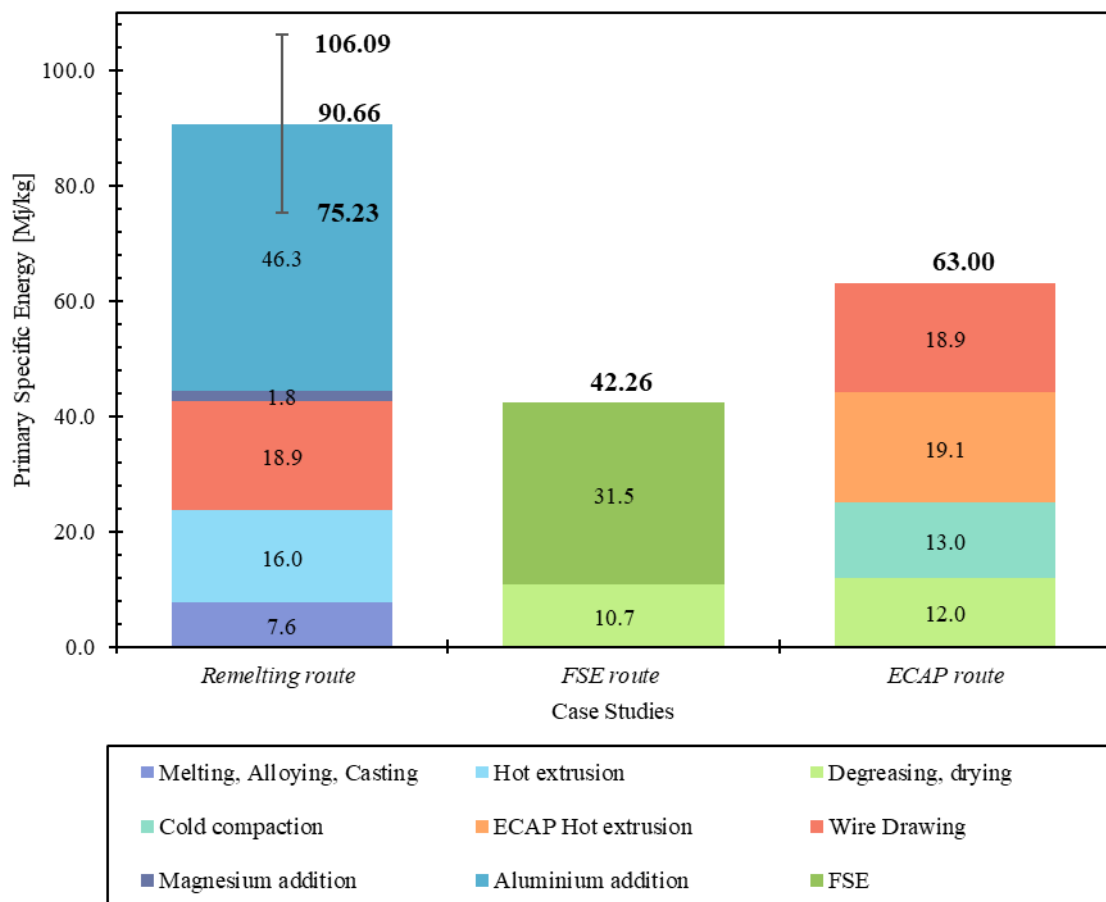


Figure 3.44. Primary specific energy demands of the analysed recycling routes.

Summing up, the obtained results show that in the case of wire production, the FSE enables a further primary energy demand reduction with respect to ECAP based route. It is worth pointing out that, at present, SSR might represent a part of the solution; in fact, such techniques do not allow composition changes (either alloying elements or primary aluminium addition) as remelting based route does. In consequence, only closed-loop recycling strategies can be applied and the big variety characterizing the aluminium demand cannot be met by SSR. On the other hand, SSR approaches are particularly suitable for in-house recycling and the supply chain could be significantly compressed enabling further energy savings.

Finally, it is worth noticing that the presented analysis and comparison was carried out using only the primary specific energy. A comprehensive LCA analysis would have probably highlighted more the advantages of SSR since that processes are certainly characterized by reduced environmental impact with respect to remelting recycling routes that are affected by fumes, slug production etc.

3.9 FSE as a primary manufacturing process

The FSE process has been developed mainly for metal chip recycling, but it has been successively applied for direct processing of, granulated materials, powders, and solid billets [110]. That last applications are fundamentally primary manufacturing processes to produce wires out of bulk or powders. The growing development of new manufacturing processes such as Wire Arc Additive Manufacturing [116] (WAAM) caused the needs for welding wire to increase in the last years.

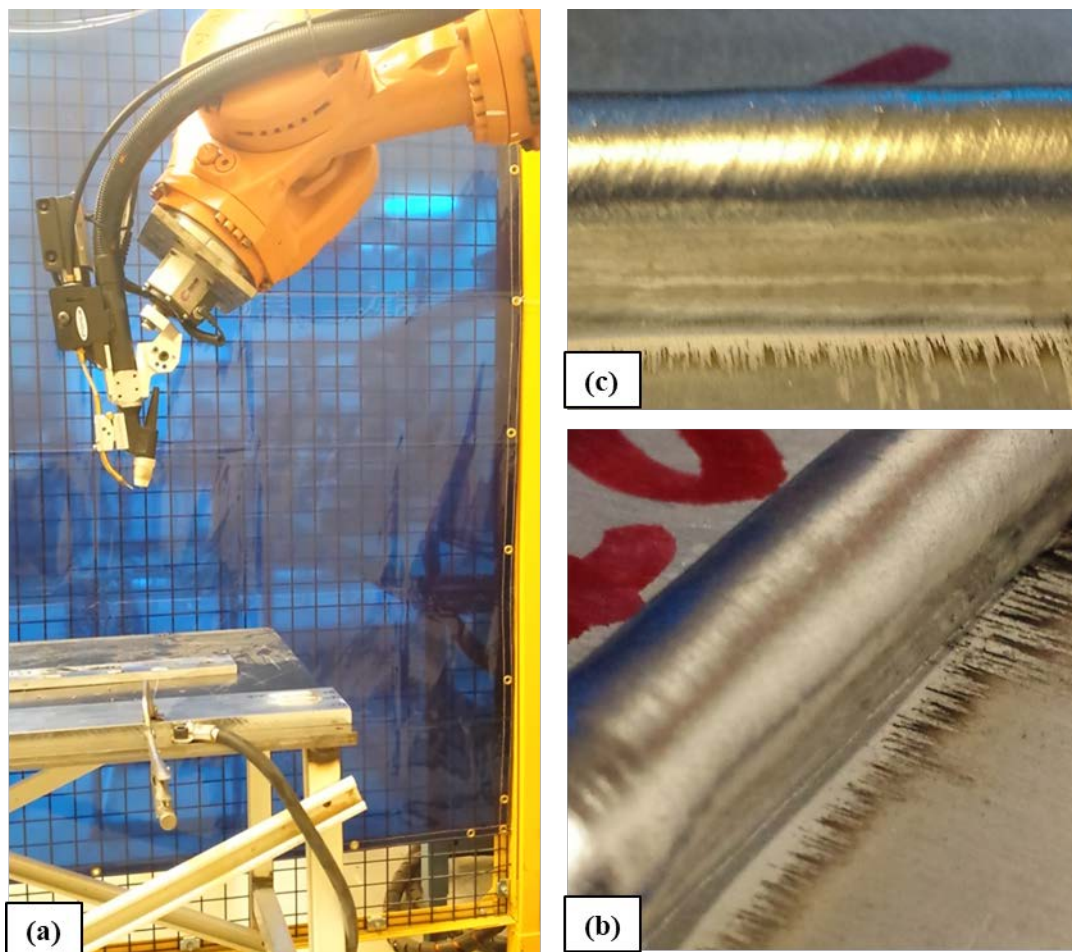


Figure 3.45. (a) WAAM setup, (b) and (c) AM wall.

In particular, the WAAM processes are being applied to a substrate of many different materials [117,118], that are often not available in as welding electrodes. These needs for small electrodes lots with peculiar composition cannot be produced effectively by conventional wire manufacturing routes. FSE is an effective solution to that requirements, allowing electrode production directly from bulk or powder. Using the latter solution, small adjustments in the final product composition can be carried out.

The feasibility of that WAAM “filler material” manufacturing strategy has been investigated producing AA 2000 series FSEed wires that have been successively deposited on a substrate using a TIG welder mounted on a KUKA industrial robot (Figure 3.45).

3.10 Process development outlook

In the previous paragraphs, the FSE process has been investigated under many different points of view and the many advantages of that technique with respect to both the conventional and other innovative recycling strategies have been highlighted. Unfortunately, some issues related to the FSE solution still needs to be addressed to prompt further process spread and development. One of the main drawbacks of the process is the limited amount of material that is possible to process because of the volume of the chamber. In particular, the chamber height is limited both by the maximum vertical stroke of the used FSW machine and the length of the die. In fact, using an excessively long die may lead to vibration due to the high compression load acting on it. Moreover, the increase of the die diameter would cause the torque and the vertical force required to carry out the process to overcome the machine limits. On the other hand, a larger die would also allow obtaining bigger wire diameter maintaining the optimal extrusion ratio.

3.10.1 Continuous machine design development

To overcome the above-described issues, a new dedicated machine for FSE has to be developed [119]. The structure of this machine was designed thanks to the expertise acquired during the previous experimental campaign. In particular, in order to maximize the frame stiffness, four columns design with horizontal axes was chosen (Figure 3.46). The machine is composed by a ram controlled by four hydraulic actuators that move against a backing basement housing the chips feeding system (Figure 3.47). This system was developed in order to make the extrusion process continuous; it is composed by a specifically designed cochlea driven by the feeding motor. The feeding system is analogous to a conventional screw extruder used for both plastics and metals [71].

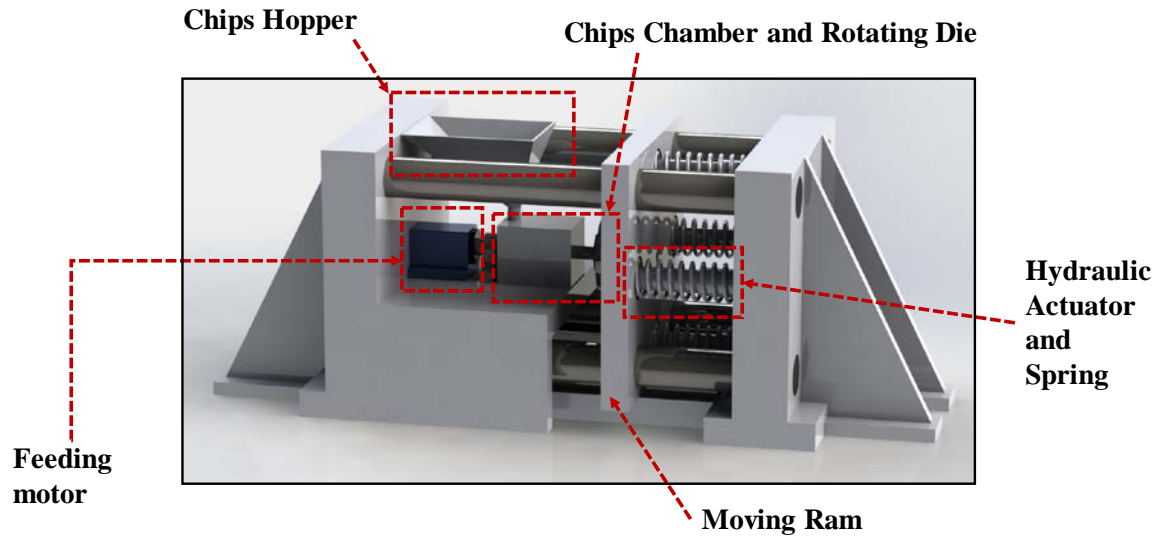


Figure 3.46. CAD of the proposed machine.

The implementation of this system together with the rotary extrusion die allows not to use any external heat source to achieve proper material softening. Metal chips are directed by a hopper toward the screw that pushes them inside the chamber against the rotary die. The die is mounted on a mandrel driven by a dedicated motor on the moving ram. The ram slides on the four main columns and on two complementary gibs in order to increase the overall stiffness. One of the main challenges undergone during the design of the machine was the cochlea geometry.

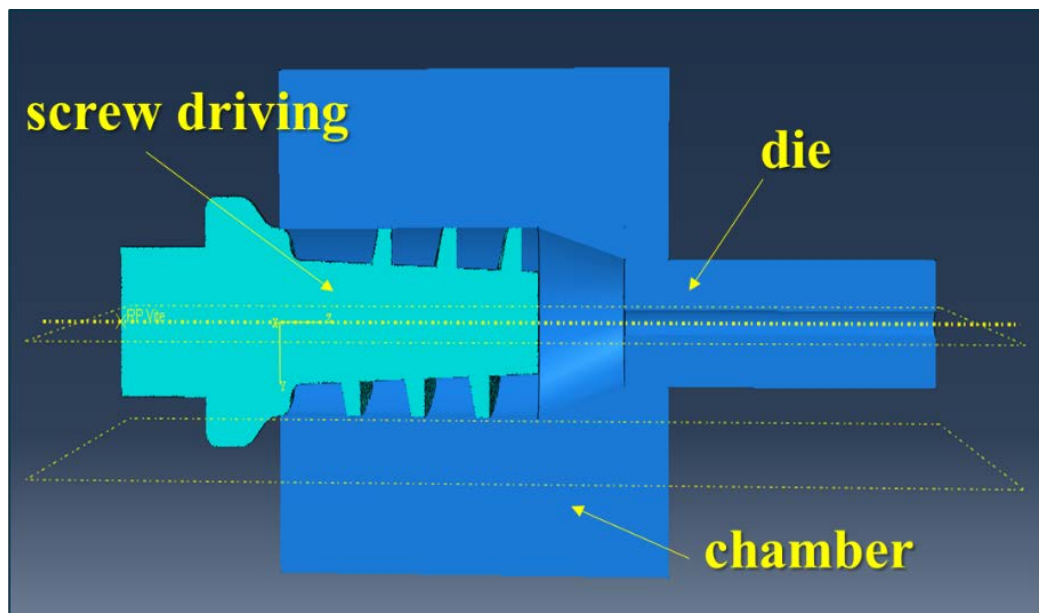


Figure 3.47. Chip feeding system.

As a matter of fact, this component of the feeding system has to ensure that new material is driven into the extrusion chamber while the process takes place in order to maintain the extrusion pressure.

Numerical simulations were carried out with varying cochlea geometry in order to minimize thread deflection during the process. Moreover, the steam geometry designed in order to guarantee an even stress distribution in the whole tool. In Figure 3.48, Von Mises stress for two different geometries are presented, showing how the optimized design (Figure 3.48b) allows to effectively reduce stress concentrations.

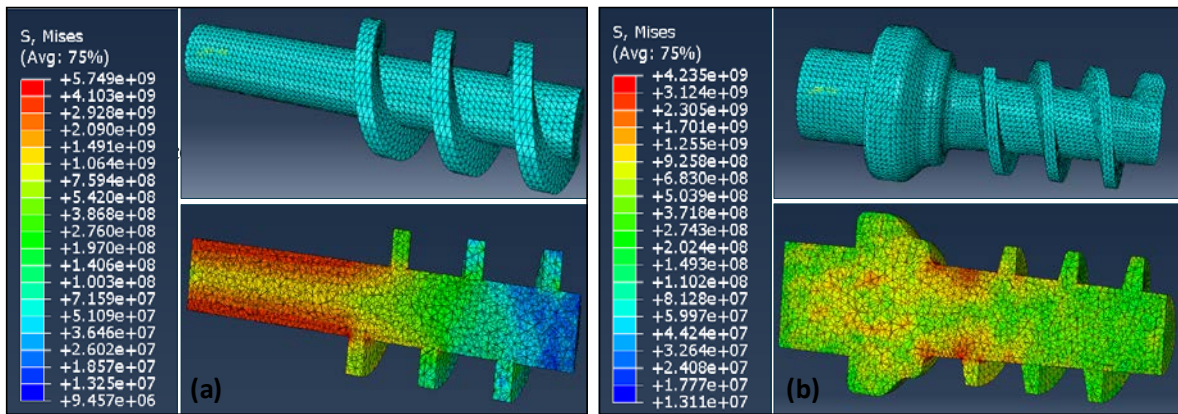


Figure 3.48. Von Mises stress distributions under 50 kN, 450 Nm for initial (a) and optimized (b) design.

The designed direct chip recycling device will be then developed with the following innovative features:

- ✓ Proper range of process parameters determined in an automatic manner by monitoring in-process the key parameters: rotation, torque, displacement, force, extrusion, temperature & extrusion rate;
- ✓ Modular tooling system for automatically changing the geometry of the die and of the friction surface according to the thermo-mechanical properties of the material used;

- ✓ In-process cooling system for the extruded wire for enhancing its microstructure;
- ✓ Dedicated feeding system for making the direct recycling process continuous, in such a way that the extruded wire will be automatically recirculated and re-added to the part being manufactured.

4. Friction Stir Consolidation

4.1 Historical background and process description

In 1975, Andrew and Gilpin [120] developed the first friction based forging process that leads to the development of the Friction Stir Extrusion process that was patented by The Welding Institute of Cambridge in 1991. Friction Stir Consolidation is a technology similar to FSE but developed to obtain bulk material from the processing of an incoherent material [93] (chips to be recycled or powders). The equipment to be utilized in this process is the same as FSE, with the only exception being that the die that does include an extrusion channel. The action of that rotating tool causes the generation of heat by friction and plastic deformation of the material in the chamber (the charge). In Figure 4.1 a sketch of the FSC process is presented.

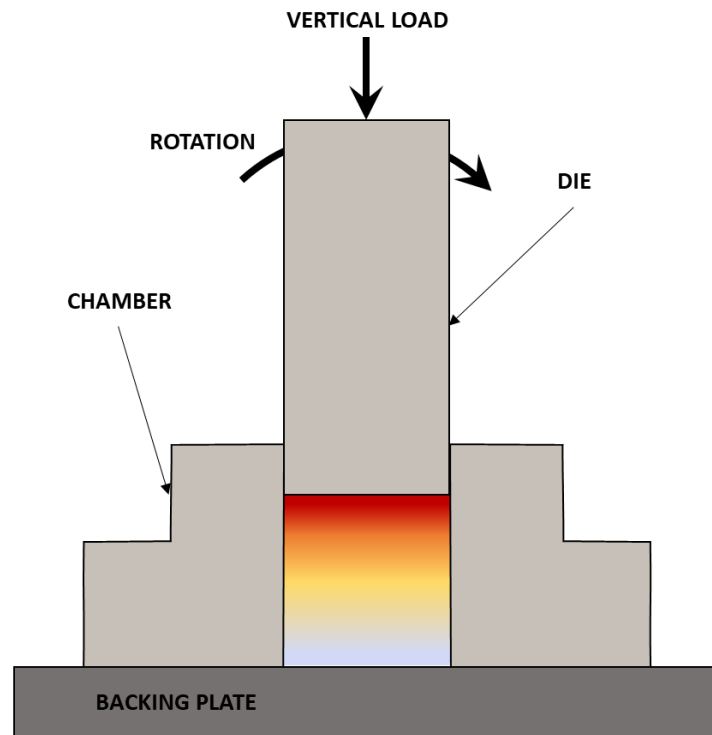


Figure 4.1. FSC process sketch.

Under the forging and stirring action of the die, the oxide layer on the particles is broken and they can bond together. Low porosity and a fine recrystallized grain structure were obtained through FSCs to produce Metal Matrix Composites [121] and thermoelectric materials [122].

4.1.1 Process parameters

Similarly to FSE, the main process parameter of FSC are the consolidation force and the die rotational speed. The concurrent effect of these parameter produces the proper heating and deformation on the material allowing solid bonding to happen. Obviously, the vertical position of the die reaches a steady state after an initial transient where the volume of the billet being processed decrease. This happens because of the progressive closing of the voids characterizing the initial texture of the compacted chips. A typical trend of these parameters during consolidation experiments is shown in Figure 4.2. Finally, the additional parameter that drastically affects the process output is time.

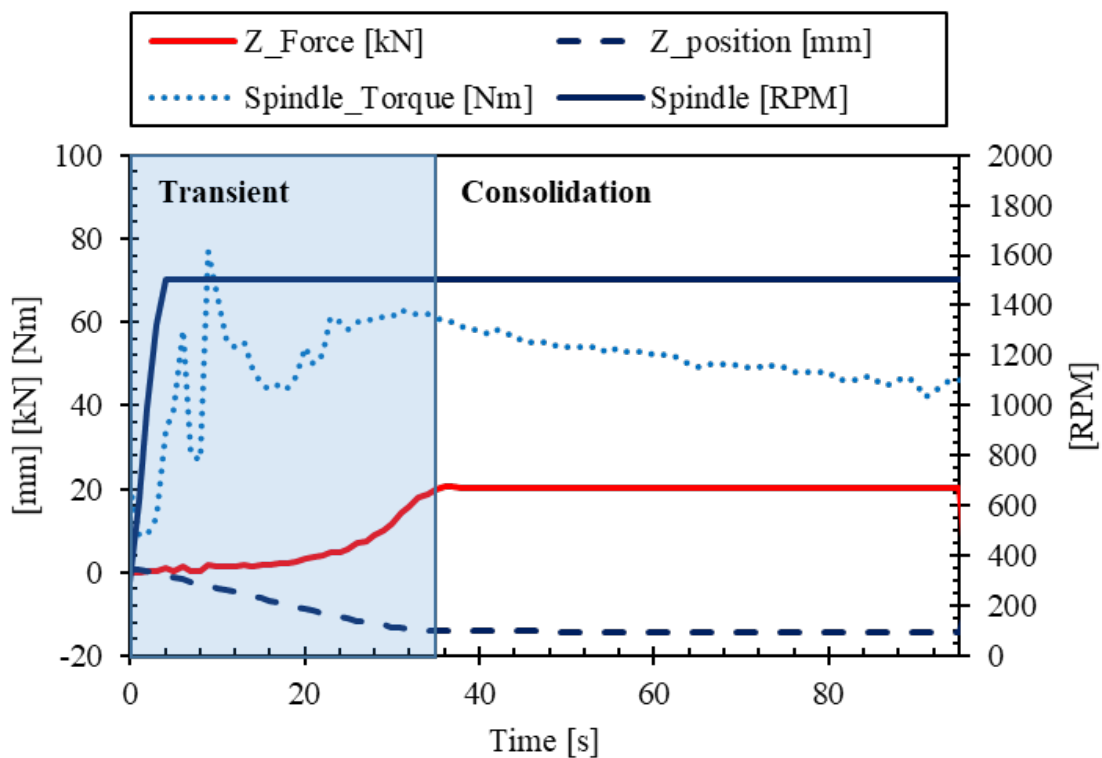


Figure 4.2. Process variable against time during FSC.

4.2 Experimental campaigns

4.2.1 Experimental setup

A dedicated fixture was designed and built for the experiments. In particular, the rotating die was made in AISI H13 with a diameter of 25 mm. The chamber was fabricated from O1 tool steel with an inner diameter of 25.4 mm and was mounted on a stainless steel backing plate. An MTS Friction Stir Welding Process Development System (FSW PDS) was used for the experiments. This machine allows the control of the applied load on the vertical axis resulting in a force-controlled consolidation. The rotation speed, die position, and Z-force were recorded during the consolidation by the FSW PDS control computer with 10 Hz sampling rate. The chips to be processed were loaded into the chamber and pre-compacted with a load of 8900 N without rotating the die. The compaction force was then adjusted to 2225 N and the spindle rotation was started. Once the die was rotating at the correct rate the compaction force was raised to the desired level and maintained for the specified time.

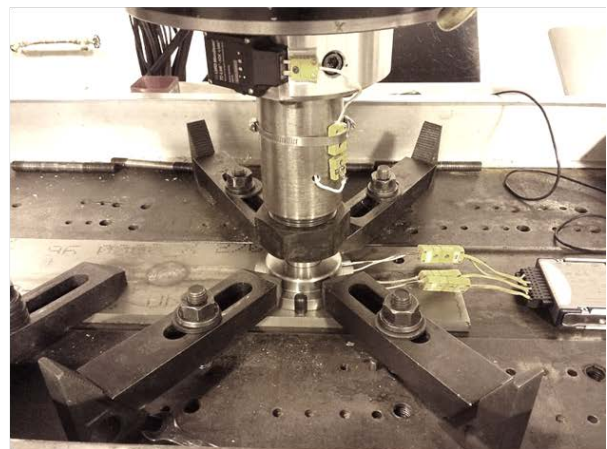
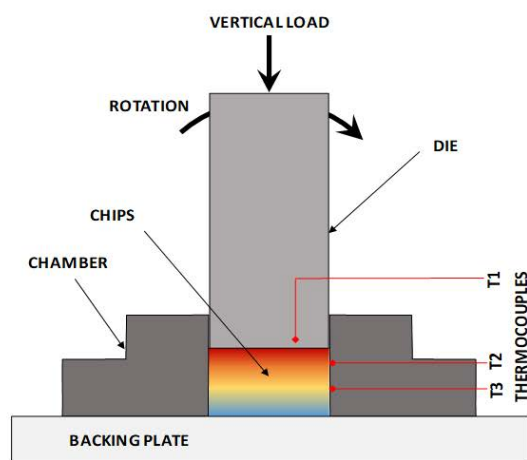


Figure 4.3. FSC experimental setup.

The temperature in the chamber's inner wall and close to the die surface was acquired through three K-type embedded thermocouples whose position is highlighted in Figure 4.3. After each consolidation experiment, the obtained billet was removed from the chamber, sectioned, ground, polished, and etched using Keller's etchant (190 ml water, 2 ml HF, 3 ml HCl, and 5 ml HNO₃) to reveal the macro and microstructure.

4.2.2 Materials

The feasibility of the FSC process has been investigated on two different kinds of processing scrap. AA2024 machining chips similar to the ones already described in the FSE section have been consolidated. Additionally, also sheet metal scrap consisting of 1 mm thick AA1050 aluminium alloy sheet chopped into irregular pieces (see Figure 4.4) with sizes ranging from 5 mm to 10 mm were processed.

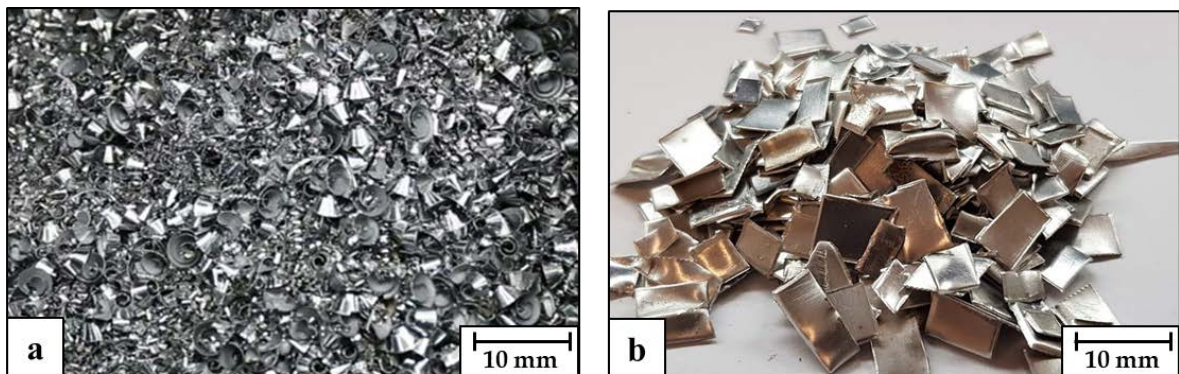


Figure 4.4. (a) Metal chip and (b) sheet metal scrap.

4.3 Process mechanics

Contrary to the FSE where steady state condition can be reached once the starting transient is reached, FSC is a time-dependent process. In fact process time drastically affects the product quality [123] since the consolidation process happens gradually. The latter assumption is clearly confirmed by Figure 4.5 where the cross sections of consolidated discs with varying process time are shown. During the first seconds of the process, a considerable amount of material at the bottom of the die chamber is still loose, unconsolidated chips (Figure 4.5a). With higher processing time an advancing front of plasticized material directly affected by the tool action gradually expands toward the bottom of the chamber with a peculiar shape (Figure 4.5d).

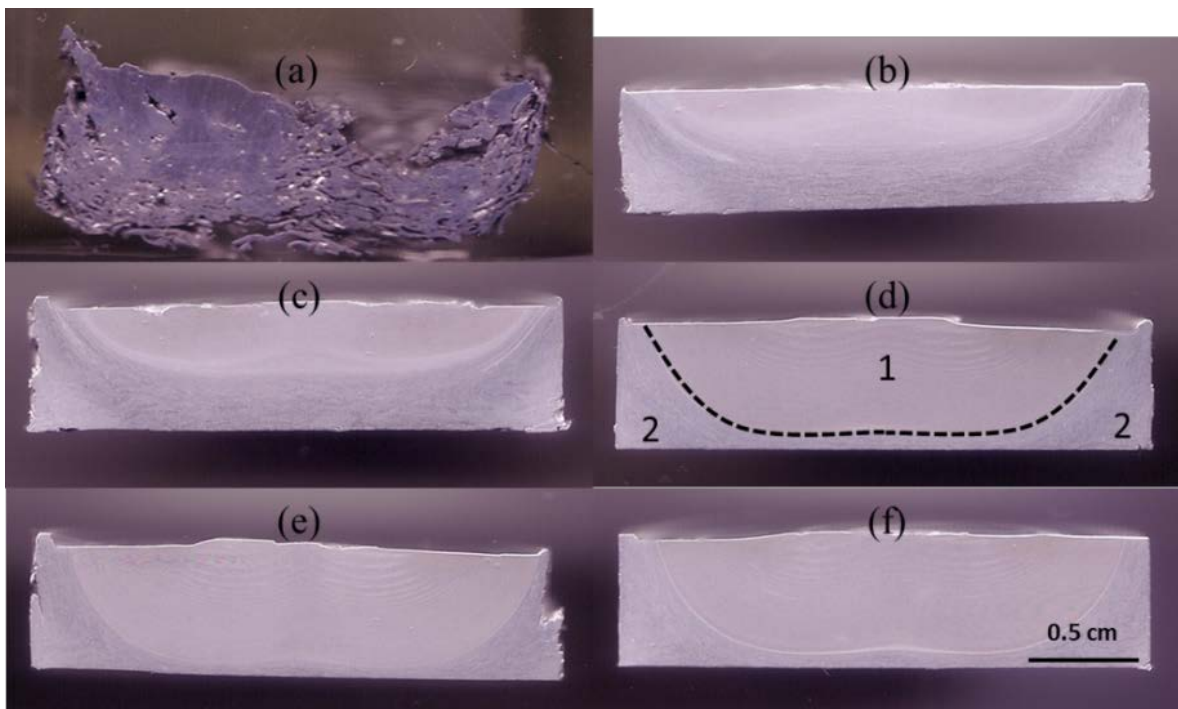


Figure 4.5. Cross-sections of series of partial consolidation discs, 300rpm and 17.8kN, from (a) to (f): 6.1s, 12.5s, 19.2s, 30.9s, 42.3s, and 45.1s processing time.

A similar morphology can be observed while processing sheet metal scrap, with better emphasis on the unconsolidated area thanks to the definite shape of the scrap being processed. Figure 4.6 shows two partial views of the section from case studies characterized with different process time. Observing the etched surfaces, three different morphologies can be identified: starting from the top of the billet (Figure 4.6c, i.e. the area closer to the die) the material appears to be highly deformed and none of the initial scraps can be observed, possibly thanks to the recrystallization happening in the area due to the die stirring action. Moving along the billet height, after a transition zone (Figure 4.6d); the material appears to be composed of the initial sheet metal pieces welded together thanks to solid bonding phenomena (Figure 4.6e). The boundaries between the particles are clearly visible and the oxides have not been dispersed since the stirring action of the tool has not reached that area.

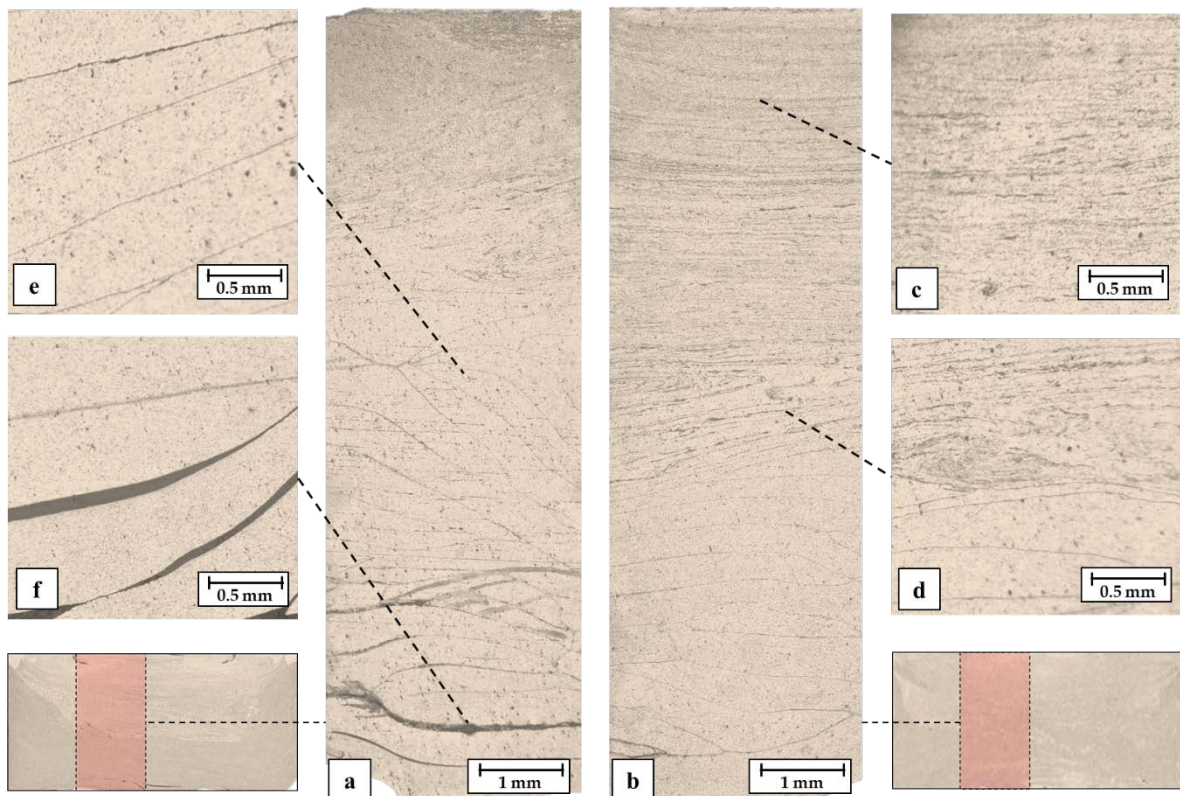


Figure 4.6. Macro and micro observation of the cross-section of FSCed sheet metal scrap disc for $t=30$ s (a) and $t=60$ s (b) case studies; (c) stirred material; (d) transition zone; (e) bounded material; (f) unbounded material.

Finally, at the very bottom of the billet (Figure 4.6f) the scarps are merely compacted, without any proper bond between each other. It is worth noticing that a longer processing time (Figure 4.6b) allows the front of stirred material to advance more in deep in the chamber resulting in a wider effectively processed. This part of the billet is characterized by uniform mechanical properties comparable to the parent material while the rest of it has certainly lower mechanical strength due to the progressively less effective bonding. That gradient in the bonding quality is confirmed by microhardness measurements in the cross-section of the same FSCed billets (Figure 4.7). The material in the upper area of the chamber (i.e. the material closer to the tool) is characterized by HV values equal to the base material while the mechanical property decays significantly moving toward the bottom of the chamber. This effect is more relevant in the case studies characterized by a minor processing time where the area of uniform and high hardness is smaller. No significant gradient is observed along the diameter of the billet (Figure 4.7b) where the hardness values match the corresponding one on the billet centre.

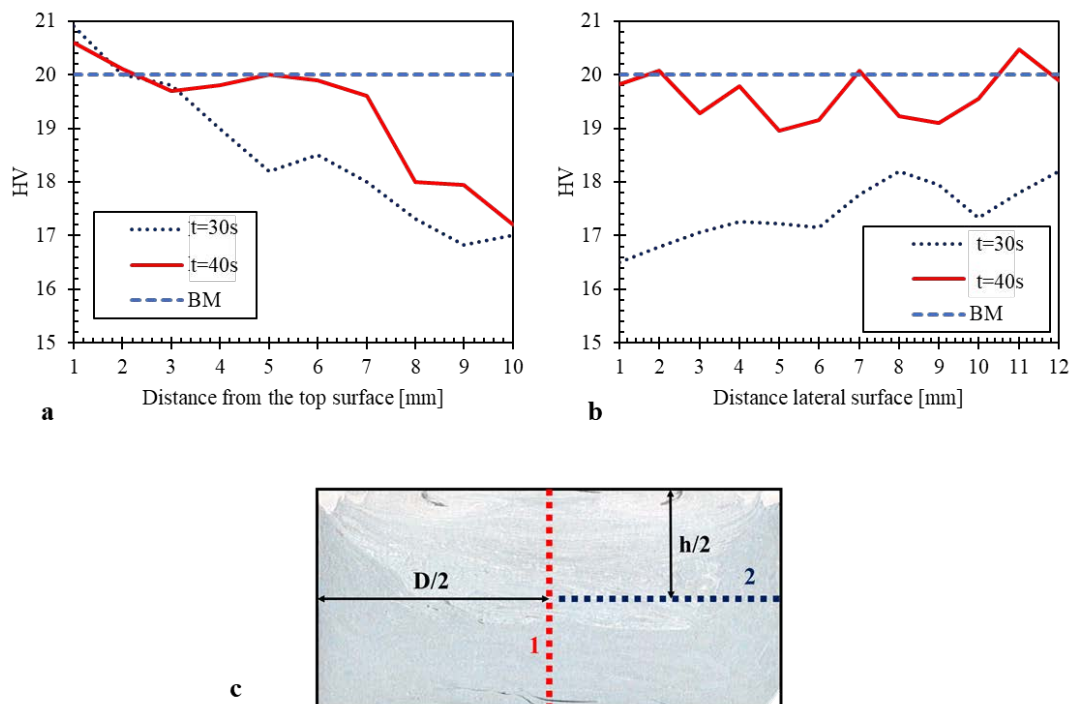


Figure 4.7. Microhardness measurements on the cross section of FSCed discs with varying process time against distance from the top (a) and lateral (b) surface compared to the base material (BM); (c) sketch of measurements lines.

Summing up the obtained results, the following main conclusion can be drawn:

- ✓ The FSC process is feasible to consolidates both metal chip and sheet metal scraps;
- ✓ During the consolidation process, the high temperature and severe plastic deformation produce a bowl shape fully consolidated region with recrystallized equiaxed grain structure at the top of billet charge. With increasing processing time, that region gradually expands from top to lower part of the billet chamber but cannot reach bottom corner even after long processing time.

4.4 Numerical FEM model

4.4.1 Governing equations

The numerical model was developed using the commercial FEA software DEFORM-3D, Lagrangian implicit code designed for metal forming processes. The implemented FEM formulation is based on the variational approach. The governing equation of the model are the same that have been elucidated for the FSE model (*Paragraph 3.3.1*).

4.4.2 Model setup and calibration

Four different objects were modeled (Figure 4.8): the chamber, the backing plate, and the rotating punch were modeled as rigid bodies and meshed with 10000 elements each in order to solve the thermal problem considering heat transfer. The workpiece, representing the compacted chips, was modeled as a unique cylinder. The chamber was fixed in space, while the die rotated around its longitudinal axis and was plunged into the chamber. The backing plate was modeled as a separate object in order to assign different tribological conditions to the bottom of the billet and the lateral surface. The sticking condition (no sliding velocity between the contact nodes) was applied between the billet and the backing plate in order to prevent the rigid rotation of the billet in the very first steps of the simulation.

The vertical movement of the die was assigned as a time-dependent law obtained from experimental measurements during force-controlled trials. It is worth noting that this expedient was needed to simulate force-controlled extrusion in order to save CPU time, which can be significantly higher when force controlled boundary conditions are assigned. In Figure 4.9a the input curve for the 300 rpm 17.8 kN case study is shown in comparison with the experimental data from the

MTS machine. The initial, linear part of the experimental curve (up to approximately 40 s) was not taken into account for the FEM input because it refers to the initial compaction before the spindle rotation starts. The “single-block” workpiece, whose geometry is shown in Figure 4.8, is characterized by a mesh of 35000 tetrahedral elements of variable size. The area of the workpiece close to the contact interface with the rotating tool meshed with elements 10 times smaller than the largest one, i.e. about 1 mm on edge.

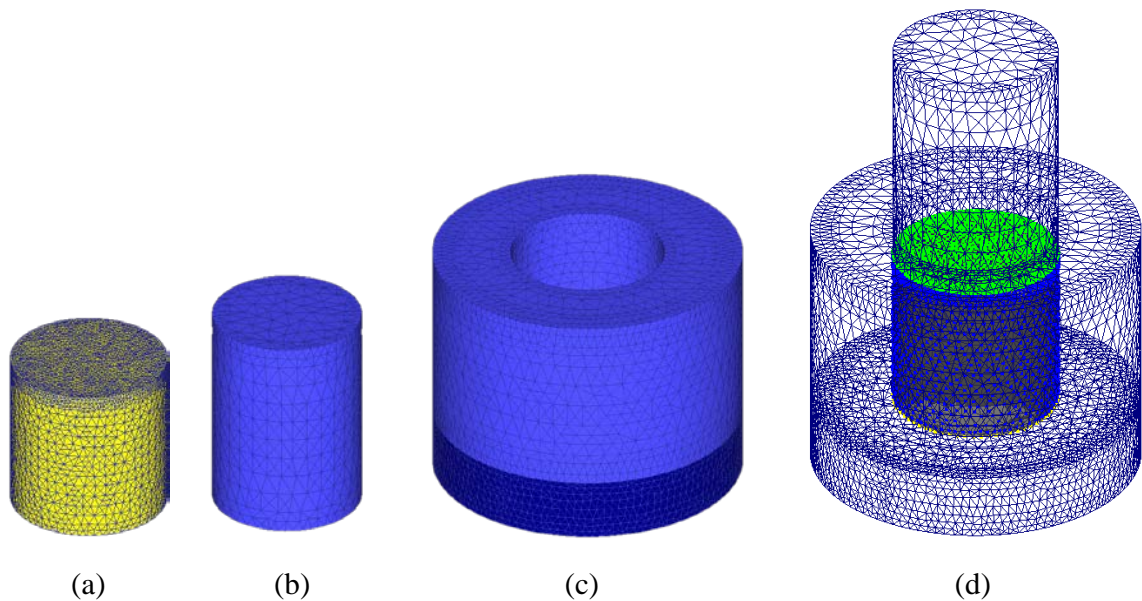


Figure 4.8. Sketch of the model: (a) compacted chips billet, (b) rotating die, (c) chamber and backing plate, (d) assembled model highlighting contact nodes.

One of the main issues to deal with during the development of this model was the definition of the material model. The model should take into account the discrete nature of metal chips, considering that it would be extremely time-consuming to correctly model them in their real form. Therefore, the Shima and Oyane formulation [124] for porous material was implemented. Metal chips are usually compacted into the matrix before the beginning of the extrusion process due to the action of the tool. This billet of compacted metal scraps can be considered a single porous object, allowing the identification of defects and voids in the extruded wires through the analysis of the relative density variation, namely the ratio between the

compacted billet density and base material density. The yield surface implemented by this model is based on a corrected Von Mises criterion that takes into account the presence of microvoids in the material matrix. The formulation is presented in Equation 10 where R_0 is the relative density of the porous material (namely of the billet of compacted chips), R is the instantaneous relative density and $\Delta\varepsilon_v$ the deformation due to volume variation of microvoids (whose number does not change according to the base hypothesis of this formulation).

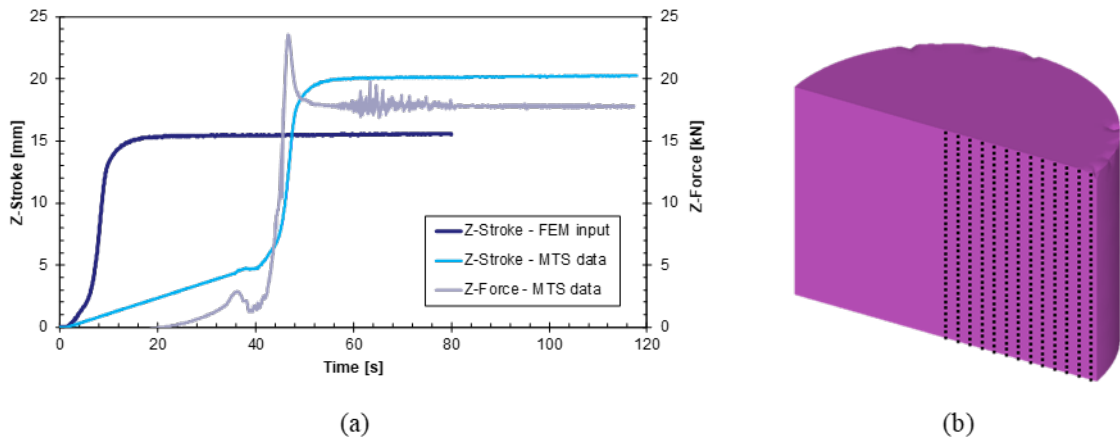


Figure 4.9. (a) Die displacement and force for the 300 rpm 17.8 kN case study and (b) point matrix for data extraction.

The initial relative density R_0 was set to 0.7. This is calculated from the known mass and the volume at zero processing time, considering the die position from experimental data. The temperature, strain and strain rate dependent material flow was obtained from the DEFORM library (Equation 15 shows the material law for AA2050).

$$\sigma = 6.78(7374.19 + \varepsilon)^{0.11} \dot{\varepsilon}^{0.044} \exp(654.8/T_{abs}) \quad (15)$$

Constant thermal conductivity and thermal capacity, equal to 180.2 N/(sK) and 2.4 N/(mm²K), respectively, were used. This assumption linearizes the thermal problem speeding up the simulation. The contact between the tool and the

workpiece was modelled through a shear model, with shear friction factor equal to 0.4 and heat exchange coefficient equal to 11 N/(mmKs). In particular, due to the significant difficulties arising in the experimental determination of the friction factor, an inverse approach was used by minimizing the error between the temperature measured by thermocouples in the experimental apparatus and those calculated by the model with varying shear factor. The final result of the calibration is shown in Figure 4.10, where an experimental temperature-time curve is compared to the numerical one obtained by tracking the corresponding location of the thermocouple in the modelled matrix. In order to extract the data from the model to calculate additional field variables (i.e. a bonding criterion) the point tracking option was used, using a matrix of 650 points equally spaced of 1 mm on one half of a longitudinal section of the billet (see Figure 4.9b) symmetric. The data were then elaborated using a dedicated Matlab post processing routine.

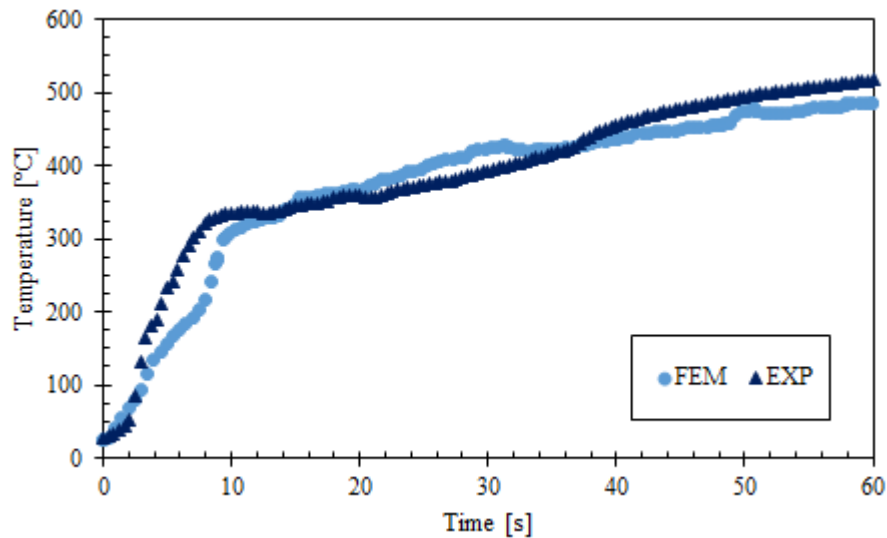


Figure 4.5. Comparison between temperatures acquired by thermocouples T1 and the numerical prediction.

4.5 Bonding Prediction

4.5.1 FEM results

The preliminary result of the numerical simulation qualitatively matches with the experimental results. Figure 4.6 shows the distribution of the relative density of the billet material during the FSC process. As the die starts rotating, the density of the peripheral region at the top of the charge starts to increase first. With further heat generation and deformation, the material in the middle and lower region are gradually densified to maximum compaction. At the bottom corner of the billet insufficient deformation is applied to produce densification.

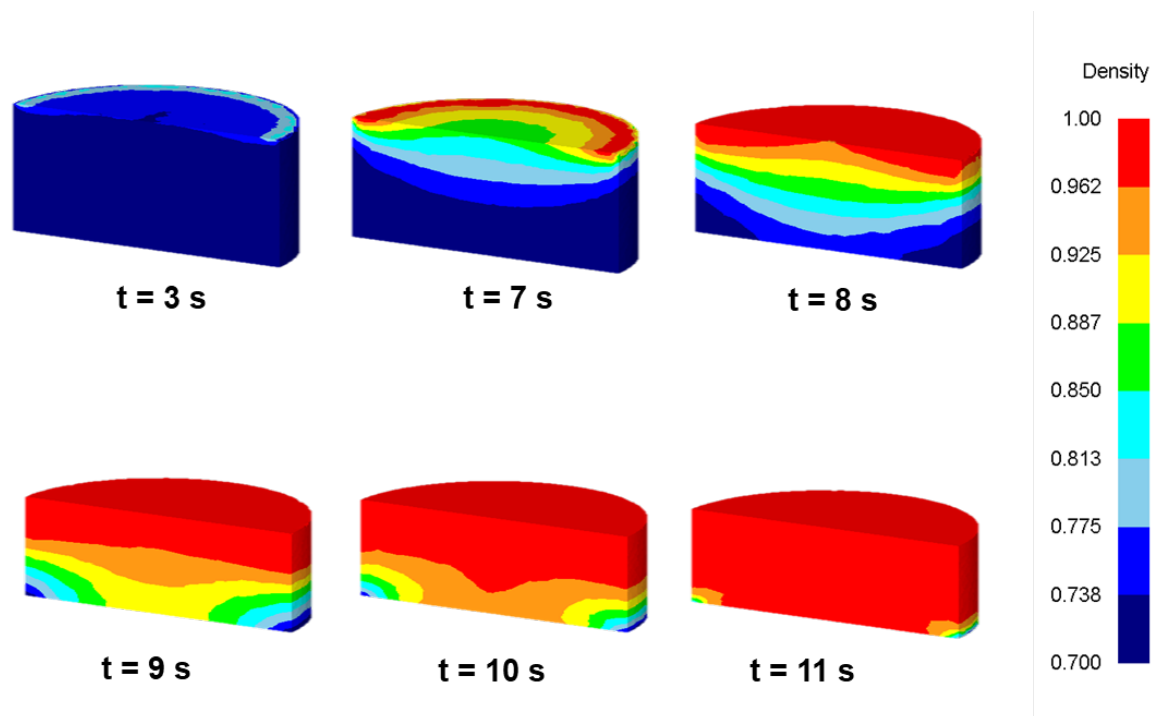


Figure 4.6. Relative density on the vertical cross-section of billet material in different stages of numerical model of friction stir consolidation: 300rpm and 17.8kN.

The bowl shape gradient of density on the vertical cross-section matches qualitatively with the metallographic result. It should be noted that, in the simulation, the region with a relative density equal to 1 may include fully

compacted but not bonded material, partially consolidated material, and fully consolidated material. In fact, fully compaction is a necessary condition to reach proper bonding but not a sufficient one. To better predict the bonding condition, the relative density, temperature and effective strain need to be considered together, since all of these parameters concur to the solid bonding of the chips to be consolidated. Figure 4.7 shows the simulated distribution of these variables compared with metallographic samples on corresponding vertical cross-sections. At 6 seconds of processing time, only a small portion at the top has reached sufficient temperature and strain for solid bonding. Therefore, the volume of consolidated material is limited and still contains voids.

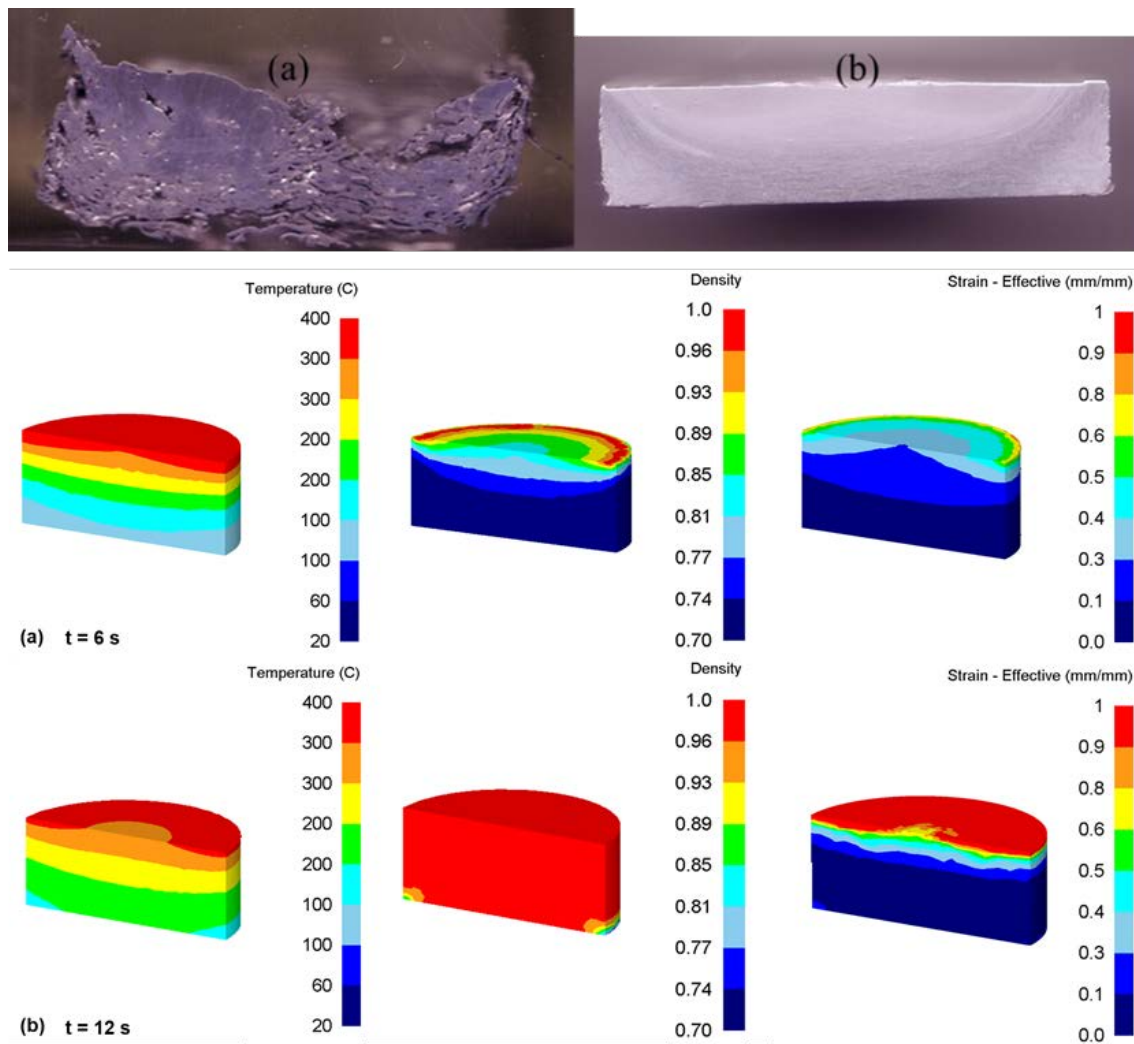


Figure 4.7. Metallographic sample and simulated temperature, density and effective strain profile at processing time in (a) 6s, (b) 12s, 300rpm and 17.8kN.

Remember, most of the billet chips are not bonded with the sample shown in this picture, which indicates the relative density remains low as predicted in the simulation.

At 12 second of processing time, both temperature and deformation increased in the lower region meanwhile the relative density reaches 1. These variables can give a hint about the consolidation state of the material for a given time of processing, but this information cannot be exhaustive on its own. For example, it is worth noting that a region with a relative density equal to one (Figure 4.8) may include partially consolidated or merely compacted material without any bond between the chips. In fact, full compaction is a necessary but insufficient condition to reach a proper state of bonding. In Figure 4.8 the evolution of relative density during the process is compared to the corresponding consolidated disc, highlighting the area that did not undergo full consolidation. To obtain a better evaluation of the bonding condition it is hence necessary to take into account at the same time the influence of multiple parameters that concur to the happening of solid bonding, such as temperature, strain etc. To merge the effect of all these variables it is possible to implement in the simulation a bonding criterion.

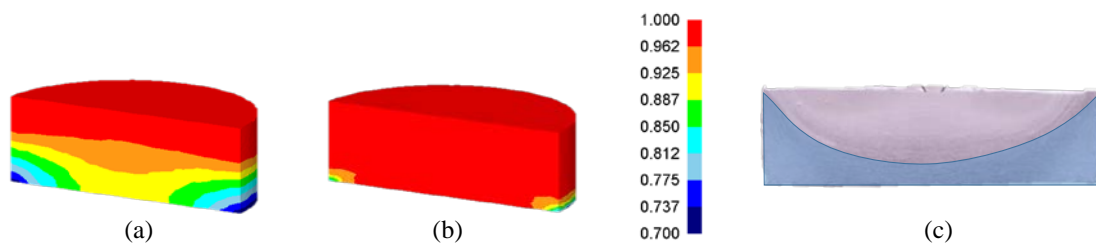


Figure 4.8. Relative density distributions for the 200 rpm 17.8 kN case study (a) 9 s, (b) 11 s, and (c) consolidated disc at 11 s.

4.5.2 Bonding criteria

To obtain a better evaluation of the bonding condition it is hence necessary to take into account at the same time the influence of multiple parameters that concur to the happening of solid bonding, such as temperature, strain etc. Analyzing Figure

4.9 it is clear, for example, that the shape of the highly deformed area closer to the die is well predicted by the model. To merge the effect of all these variables it is possible to implement in the simulation a bonding criterion.

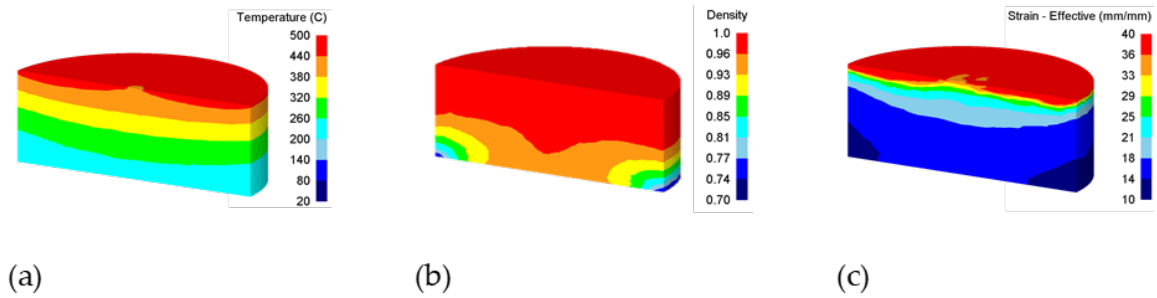


Figure 4.9. (a) Temperature, (b) relative density, and (c) strain distributions for the 300 rpm 14.7 kN 10 s case study.

Most of the criteria present in the literature are based on the pressure-time welding criterion [106] proposed by Plata and Piwnik in 2000. According to this criterion, the integral in time of the ratio between the contact pressure and the flow stress of the material is calculated (Equation 14). If this parameter exceeds a critical threshold, (dependent on the considered material or process) solid bonding occurs. Nevertheless, the use of this parameter for the FSC process gave poor results.

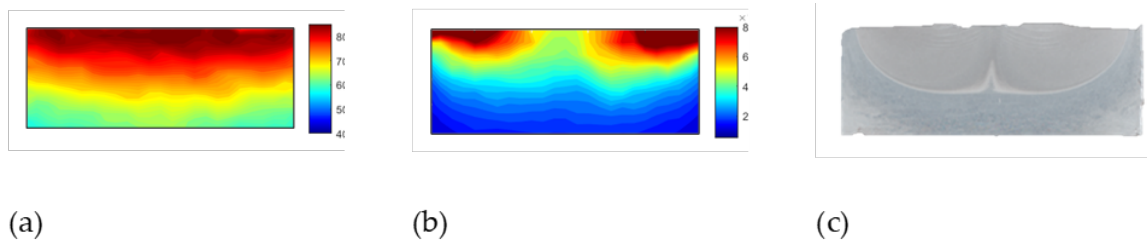


Figure 4.10. (a) w distribution, (b) w' distribution, and (c) consolidated disc for the 300 rpm 14.7 kN 45 s case study .

In Figure 4.10a the distribution of the w parameter at the end of a consolidation process is shown. It is clear from the obtained distribution, that the contact pressure between the chips to be bonded is overwhelming over the other variable concurring

to the w value. In the FSC process, there is no material exiting the chamber, causing the compression mean stress to be almost uniformly distributed in the whole consolidating billet.

$$w' = \int_0^t PR \varepsilon_e / \sigma dt \cong \sum_j p_j R_j \varepsilon_{ej} / \sigma_j \Delta t_j \quad (16)$$

To highlight the different levels of bonding reached in the different areas of the disc (as highlighted in the etched cross-section showed in Figure 4.9c) it is necessary to add some additional influencing parameter to the bonding criteria. The combination of parameters that allowed to better reproduce the consolidated area and even the highly deformed and recrystallized areas in the consolidated disk is presented in Equation 16, while Figure 4.10b shows the corresponding distribution of this new field variable. The relative density and the deformation resulted to be particularly effective to correct the w parameter to better reproduce the bonding condition in FSC. In fact, deformation has the essential effect of prompting the disruption of the oxide layer covering the chips, while the increase of relative density is, as already stated, one of the necessary conditions for an effective consolidation [125].

4.6 Process energy demands

The environmental impact of the FSC process in term of energy consumption has been evaluated and compared to other analogous recycling strategies. The adopted methodology is similar to the one already described in *Paragraph 3.8* for FSE.

4.6.1 System boundary and major assumptions

In particular, the conventional remelting route and the novel SPS based direct recycling technique have been analysed. The SPS process was selected considering the similarity with FSE in term of geometry of the secondary produced material. Both techniques allow to produce bulk billed or disk of consolidated material processing metal scrap or granulates. The main characteristics of the SPS have been described in the analysis of the state of the art for direct recycling (*Paragraph 2.2.7*).

A 10 g AA6060 billet was selected as the functional unit and it was applied to the LCI of the investigated case studies; this value corresponds to the optimal amount of material consolidable using the lab-scale fixture use for the experimental campaigns. In the SPS and FSC based route, chips cleaning and compaction steps are considered prior to the actual consolidation step. The severe deformation characterizing the process, enable oxides layers breaking and solid bonding activation. An additional old compaction stage was considered for the SPS workflow. Concerning the remelting approach, the chips are collected and melted together to get the desired alloy to be hence extruded to get the proper workpiece.

A closed AA6060 recycling loop was considered for all the routes, avoiding down-cycling or compositional corrections during melting. The selected system boundary is depicted in Figure 4.12 where all the process steps accounted for as well as the material flows are highlighted. It can be noticed that process scraps were

taken into account and were considered as part of a new recycling phase. The impact of permanent material losses occurring during remelting was considered by adding the same amount of primary aluminium in the model. The primary energy was considered as a metric to compare the different process routes. The processes electric energy demand was converted into (primary) energy source consumption by considering an average efficiency of 34% to account for the energy generation and the transmission losses.

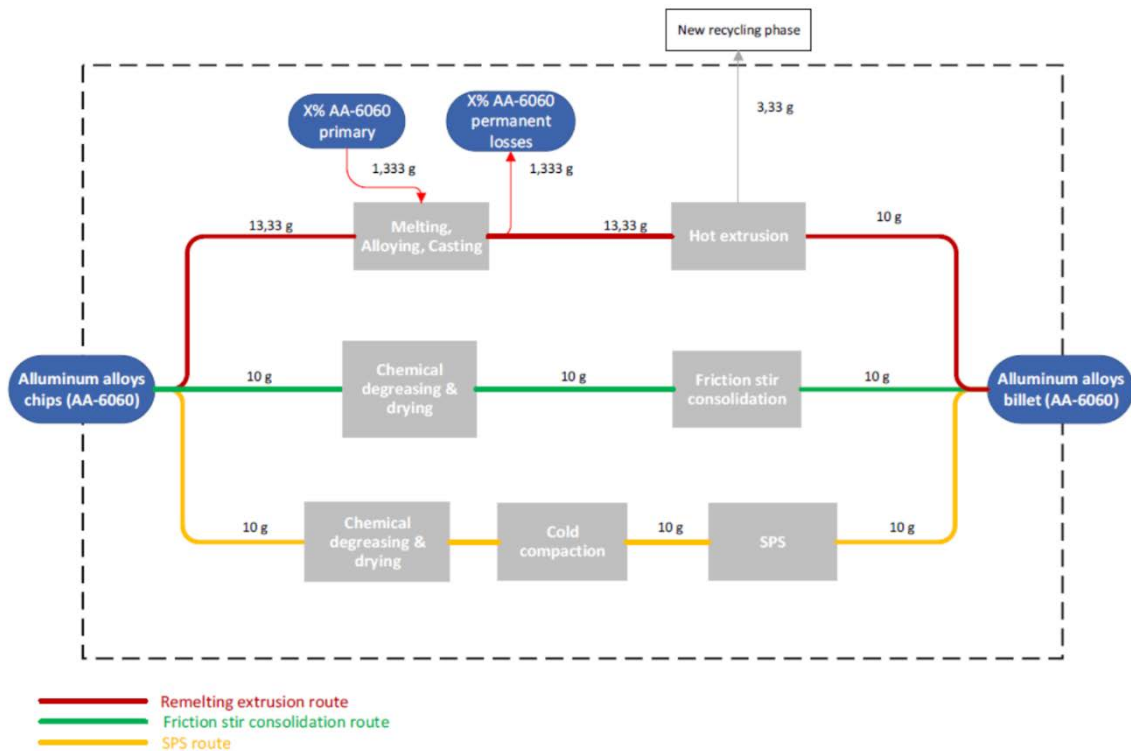


Figure 4.12. System boundary with considered processes and material flows highlighted.

4.6.2 Life Cycle Inventory

The energy demands of the FSC and the SPS process are available as results of direct measurements carried out by in-house experiments and available in literature respectively. The conventional remelting The EAA environmental report [16], as well as the paper from Duflou et al. [28], were used as primary LCI sources. The process material yields for the conventional remelting route were found in the EAA report as well. As far as the FSE and SPS are concerned, no material yield was considered since all the scraps loaded into the chambers usually undergoes

consolidation. Since the Mg content of the scrap is expected to become half or less after remelting, such loss was compensated by adding 0.3% w/w of pure Mg [101]. The main LCI values alongside the consulted references are reported in Table 4.1.

Table 4.1 Main LCI data and sources.

	Primary energy [MJ]	Reference
Cleaning	0.08	[115]
Cold Compaction	0.09	[28]
FSC	0.43	Experimentally measured
SPS	0.31	[28]
Hot extrusion	0.14	[16]
Primary Production AA-6060	2.1	[114]
Melting and casting	0.07	[16]

4.6.2 Power measurements

Concerning the electric energy characterization of FSC, the Fluke 435 power quality analyser was used to measure tension, current, and power over process time. A typical power profile is depicted in Figure 4.13

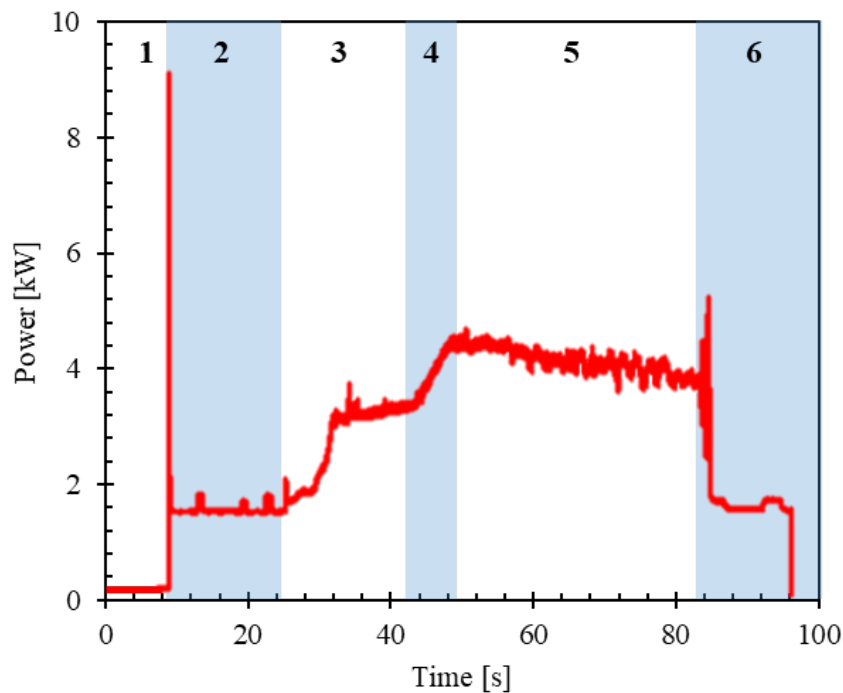


Figure 4.13. Power trend for FSC recycling.

In Figure 4.13 six different production phases are highlighted, an explanation of these phases follows:

1. Machine switch/on
2. Hydraulics on/ Stand-by mode
3. Spindle on and first plunging phase (0.5 mm/s, position control)
4. Force progressively increases to consolidation value (20 kN)
5. Consolidation phase
6. Spindle stop and hydraulic off

For the present study only phase 4 and 5 have been considered for quantifying the electric energy demand for wire production, other non-productive production modes were left out for lack of industrial time studies. It is worth noticing that the gradual increase of the consolidation force (phase 4) it is necessary only to avoid initial torque peak that would overcome the experimental machine limits. A dedicated, industrial-scale machine would not probably need such phase during the actual production process.

4.6.3 Energy demands comparison

The results of the developed comparative analysis are reported in Figure 4.14, referring to the functional unit of 10g of material. For each analysed recycling route the contribution of each process step/factor, towards the total demand, is highlighted. An intermediate scenario with 15% material losses is reported, to get this share of permanent losses a briquetting step to compact scraps is to be implemented. It is possible to see that both SSR processes outperform conventional

remelting based route. As already highlighted for the FSE processes, this is mainly due to the avoided permanent material losses. The results for both SPS and FSC are actually very close, with a slightly lower value of primary energy demand for the SPS. As a matter of facts, both strategies enables the primary energy demand to be reduced by 26% and by 26% with respect the remelting route respectively. It is worth noticing that the energy savings with respect to conventional technologies are limited if compared to the FSE case study; this is mainly caused by the absence of post-processing operations (i.e. wire drawing) affecting the remelting route. As already envisaged in the previous analysis, the absence of such step also erase the savings that the FSP based technologies have with respect to other SSR recycling strategies.

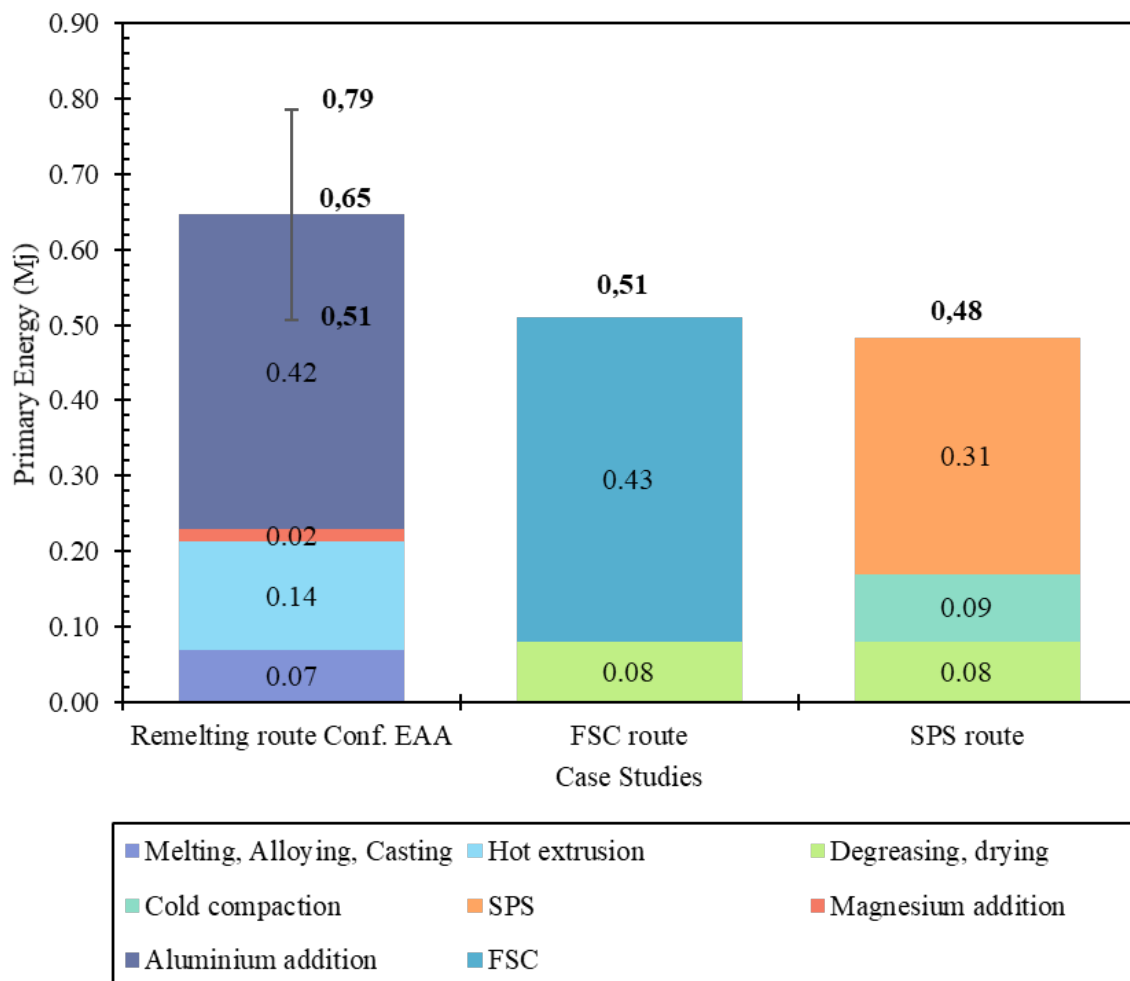


Figure 4.14. Primary energy demands of the analysed recycling routes referred to the functional unit.

In addition, the variability of the data characterizing the eco-properties (Embodied energies for material production as well as processing energies values) of materials and processes [3], does not allow a more general and clear identification of the most efficient SSR process. Furthermore, the FSC process energy consumption analysis may also be affected by the inadequacy that characterized the experimental setup and forced to introduce unnecessary intermediate phases during the scrap processing.

Summing up, the obtained results show that the SSR enables a further primary energy demand reduction with respect to remelting based route. Again, it is worth pointing out that, at present, SSR might represent a part of the solution; in fact, such techniques do not allow composition changes (either alloying elements or primary aluminium addition) as remelting based route does. In consequence, only closed-loop recycling strategies can be applied and the big variety characterizing the aluminium demand cannot be met by SSR. On the other hand, SSR approaches are particularly suitable for in-house recycling and the supply chain could be significantly compressed enabling further energy savings.

Finally, it is worth noticing that the presented analysis and comparison was carried out using only the primary specific energy. A comprehensive LCA analysis would have probably highlighted more the advantages of SSR since that processes are certainly characterized by reduced environmental impact with respect to remelting recycling routes that are affected by fumes, slug production etc.

5. Conclusions

5.1 Summary

In this dissertation, the capabilities of the FSE and FSC processes for lightweight metal chip and sheet metal scrap recycling have been investigated under different aspects. The effectiveness of these peculiar secondary production technologies has been assessed both through the evaluation of the produced material mechanical properties and by process energy measurements. Summing up, from the obtained results the following general conclusions can be drawn:

- FSE and FSC can be used effectively to process and recycle lightweight alloys scrap of different kinds. In particular, Magnesium and aluminium alloys scraps were effectively consolidated into wire or disk during distinct experimental campaigns. The mechanical properties of the obtained material are similar to the correspondent parent material being recycled.
- Both FSE and FSC based recycling routes enable primary energy savings with respect to the conventional, remelting-based secondary manufacturing processes. In the case of wire production, FSE enables a further primary energy demand reduction with respect to ECAP based route thanks to the absence of the final wire drawing steps.
- A dedicated numerical model was developed to simulate both FSE and FSC processes, giving insight on the processes mechanics and providing effective tools for products quality prediction.

- FSE is characterized by interdependent process parameters. Extrusion rate is highly influenced by tool rotation, extrusion force and extrusion ratio: extrusion rate increases with extrusion force, for a given tool rotation, while it shows a minimum, as a function of tool rotation, when extrusion force is fixed. On the other hand, peak temperature in the container matrix depends on heat input and process time i.e. extrusion rate: it decreases with constant tool rotation and increasing tool force due to predominant effect of increased extrusion rate over increased heat input. Accordingly, it has a maximum for constant extrusion force and varying tool rotation following the trend of extrusion rate. Peak torque is highly influenced by the processed material mechanical properties, being significantly higher for softer metals.
- The process monitoring of extrusion rate can be used for preliminary identification of incorrect process condition during FSE.
- Choosing correctly the process parameters, fine equiaxial recrystallized grains can be obtained in the whole cross-section of the FSEed extrudates. Excessive rpm and extrusion force cause massive grain growth and hot cracking due to the excessive thermal input. Material recrystallization occurs after the extrusion as evidenced by the equiaxial nature of the grain structure; i.e. no deformation occurs after the final recrystallization process.
- Numerical simulation results and Experimental observation of the final position of a copper marker indicated that a helical material flow occurs in the extrusion channel of an FSE die. This flow significantly affects the extrusion process. In details, when constant extrusion rate is applied, the distance covered by the material in the extrusion channel increases with tool rotation; when constant force is applied, the concurrent effect of temperature increase (contributing to increasing the extrusion rate) and friction losses increase (due to the covered distance increase and contributing to decreasing the extrusion rate) results in a minimum in the extrusion rate. Furthermore, the extrusion rate directly

influences the surface quality of extrudes, being the latter higher when lower rate is obtained through the combination of tool rotation and tool force.

- Strain and strain rate predicted by FEM simulation have maximum values in the area close to the lateral surface of the FSEed wires. However, only a small difference is observed for small diameter while a large gradient between the lateral surface and the centre is found for large diameters. Very small strain and strain rate values are calculated at the centre of the $d=9\text{mm}$ case study indicating that insufficient material flow took place. The Zener-Hollomon parameter was calculated and compared to the experimental observations allowing the identification of three distinct areas in the wire cross section: the external area, close to the lateral surface, is characterized by small and heavily deformed grains. The transition area is characterized by larger grains for which significant elongation is still visible. The central area is characterized by slightly bigger and undeformed grains, with an average dimension of about $10\ \mu\text{m}$.
- The Plata and Pivnik criterion for solid bonding was implemented and used to predict the produced FSEed wires integrity. The results are in good agreement with the experimental observations and allowed the identification of a threshold value of the W value for the considered AZ31 magnesium alloy.
- During the FSC process, time is a key factor to achieve proper consolidation. The stirring action of the tool produces a bowl shape fully consolidated region with recrystallized equiaxed grain structure at the top of billet charge. With increasing processing time, that region gradually expands from top to lower part of the billet chamber but cannot reach bottom corner even after long processing time. This cause a certain gradient in the consolidation quality moving along the billet heights, especially in low time case studies.
- A dedicated parameter for FSC was proposed correcting the Piwnik and Plata criterion with relative density and effective deformation obtaining a better prediction of the consolidating front shape.

5.2 Outlook and future developments

The results obtained by the investigations described in this dissertation and summarized in the previous chapter allowed to reduce the lack of knowledge on different aspects of the FSE and FSC process. First, the experimental campaigns allowed to find windows of workability for different materials and scrap while enabling investigation into the inner process mechanics and process parameter inter-dependence. The development of solid FEM models eased these analyses and provided effective numerical tools to predict the material processing results. Moreover, energy measurements finally enabled quantitative evaluation of the energy savings of such innovative processes, allowing direct comparison with other conventional and innovative recycling technology, also in the frame of a complete processing route through LCI analysis. Globally, both FSE and FSC resulted to be promising option for metal scrap recycling and processing, especially in the optic of in-house recycling.

Nevertheless, some aspects of both processes still need further research work to be carried out. The proposed numerical tools for integrity and bonding quality prediction needs extensive calibration in term of critical/threshold values, possibly with analytic link or comparison to other pre-existing values for different solid-state processes. The FSE process capabilities in terms of continuous production still need to be fully experimentally addressed and, generally, the SSR industrial scalability have to be properly investigated. In addition, dedicated machines should be developed for both processes. Finally, as already stated, the proposed energy consumption analysis should be integrated with a comprehensive LCA analysis, keeping into account all the aspects influencing the environmental impact of a process.

References

- [1] Worrell E, Allwood J, Gutowski T. The Role of Material Efficiency in Environmental Stewardship. *Annual Review of Environment and Resources* 2016;41:575–98. doi:10.1146/annurev-environ-110615-085737.
- [2] Gutowski TG, Sahni S, Allwood JM, Ashby MF, Worrell E. The energy required to produce materials: constraints on energy-intensity improvements, parameters of demand. *Philosophical Transactions of the Royal Society A: Mathematical, Physical and Engineering Sciences* 2013;371:20120003–20120003. doi:10.1098/rsta.2012.0003.
- [3] Ashby M. *Materials and the Environment: Eco-informed Material Choice: Second Edition*. 2012. doi:10.1016/C2010-0-66554-0.
- [4] Tolio T, Bernard A, Colledani M, Kara S, Seliger G, Duflou J, et al. Design, management and control of demanufacturing and remanufacturing systems. *CIRP Annals - Manufacturing Technology* 2017;66:585–609. doi:10.1016/j.cirp.2017.05.001.
- [5] Ingarao G. Manufacturing strategies for efficiency in energy and resources use: The role of metal shaping processes. *Journal of Cleaner Production* 2017;142:2872–86. doi:10.1016/j.jclepro.2016.10.182.
- [6] EN 12258-3:2003 Aluminium and aluminium alloys. Term and definitions. Scrap. n.d.
- [7] Xiao Y, Reuter MA. Recycling of distributed aluminium turning scrap. *Minerals Engineering* 2002;15:963–70. doi:10.1016/S0892-6875(02)00137-1.
- [8] Samuel M. A new technique for recycling aluminium scrap. *Journal of Materials Processing Technology* 2003;135:117–24. doi:10.1016/S0924-0136(02)01133-0.
- [9] Cooper DR, Song J, Gerard R. Metal recovery during melting of extruded machining chips. *Journal of Cleaner Production* 2018;200:282–92. doi:10.1016/j.jclepro.2018.07.246.
- [10] Schwarz H-G. Aluminum Production and Energy. *Encycl. Energy*, vol. 1, Elsevier; 2004, p. 81–95. doi:10.1016/B0-12-176480-X/00372-7.
- [11] Boin UMJ, Bertram M. Melting standardized aluminum scrap: A mass balance model for europe. *JOM* 2005;57:26–33. doi:10.1007/s11837-005-0164-4.

- [12] Grayson J. Reducing Melt Loss and Dross Generation. 2017.
- [13] Simon L, Moraes CAM, Modolo RCE, Vargas M, Calheiro D, Brehm FA. Recycling of contaminated metallic chip based on eco-efficiency and eco-effectiveness approaches. *Journal of Cleaner Production* 2017;153:417–24. doi:10.1016/j.jclepro.2016.11.058.
- [14] Schlesinger ME. Aluminum Recycling. Taylor & Francis; 2013.
- [15] Paraskevas D, Vanmeensel K, Vleugels J, Dewulf W, Deng Y, Duflou JR. Spark plasma sintering as a solid-state recycling technique: The case of aluminum alloy scrap consolidation. *Materials* 2014;7:5664–87. doi:10.3390/ma7085664.
- [16] EAA. Environmental Profile Report for the European Aluminium Industry. 2013.
- [17] Paraskevas D, Kellens K, Dewulf W, Duflou JR. Environmental modelling of aluminium recycling: A Life Cycle Assessment tool for sustainable metal management. *Journal of Cleaner Production* 2015;105:357–70. doi:10.1016/j.jclepro.2014.09.102.
- [18] Nakajima K, Takeda O, Miki T, Matsubae K, Nakamura S, Nagasaka T. Thermodynamic Analysis of Contamination by Alloying Elements in Aluminum Recycling. *Environmental Science & Technology* 2010;44:5594–600. doi:10.1021/es9038769.
- [19] Hiraki T, Takeda O, Nakajima K, Matsubae K, Nakamura S, Nagasaka T. Thermodynamic criteria for the removal of impurities from end-of-life magnesium alloys by evaporation and flux treatment. *Science and Technology of Advanced Materials* 2011;12. doi:10.1088/1468-6996/12/3/035003.
- [20] Lu X, Hiraki T, Nakajima K, Takeda O, Matsuabe K, Zhu HM, et al. Thermodynamic analysis of separation of alloying elements in recycling of end-of-life titanium products. *Separation and Purification Technology* 2012;89:135–41. doi:10.1016/j.seppur.2012.01.008.
- [21] Stern M. Method for treating aluminum or aluminum alloy scrap. US2391752A, 1945.
- [22] Stern M. Method for the production of shaped articles such as tubes, rods, and profiles from magnesium and magnesium alloy scrap. US2358667A, 1944.
- [23] Stern M. Direct extrusion applied to light metal scrap. *The Iron Age* 1951;28:71–3.
- [24] Sharma CS, Nakagawa T. Recent development in the recycling of machining swarfs by sintering and powder forging. *Manuf Technol, Gen Assem of CIRP, 27th 1977*;26:121–5.

- [25] Gronostajski J, Matuszak A. The recycling of metals by plastic deformation: an example of recycling of aluminium and its alloys chips. *Journal of Materials Processing Technology* 1999;92–93:35–41. doi:10.1016/S0924-0136(99)00166-1.
- [26] Baffari D, Buffa G, Campanella D, Fratini L, Micari F. Friction based Solid State Welding Techniques for Transportation Industry Applications. *Procedia CIRP* 2014;18:162–7. doi:10.1016/j.procir.2014.06.125.
- [27] Anilchandra AR, Surappa MK. Microstructure and damping behaviour of consolidated magnesium chips. *Materials Science and Engineering: A* 2012;542:94–103. doi:10.1016/j.msea.2012.02.038.
- [28] Duflou JR, Tekkaya AE, Haase M, Welo T, Vanmeensel K, Kellens K, et al. Environmental assessment of solid state recycling routes for aluminium alloys: Can solid state processes significantly reduce the environmental impact of aluminium recycling? *CIRP Annals - Manufacturing Technology* 2015;64:37–40. doi:10.1016/j.cirp.2015.04.051.
- [29] Güley V, Güzel A, Jäger A, Ben Khalifa N, Tekkaya AE, Misiolek WZ. Effect of die design on the welding quality during solid state recycling of AA6060 chips by hot extrusion. *Materials Science and Engineering: A* 2013;574:163–75. doi:10.1016/j.msea.2013.03.010.
- [30] WU S, JI Z, RONG S, HU M. Microstructure and mechanical properties of AZ31B magnesium alloy prepared by solid-state recycling process from chips. *Transactions of Nonferrous Metals Society of China* 2010;20:783–8. doi:10.1016/S1003-6326(09)60214-4.
- [31] Ji ZS, Wen LH, Li XL. Mechanical properties and fracture behavior of Mg–2.4Nd–0.6Zn–0.6Zr alloys fabricated by solid recycling process. *Journal of Materials Processing Technology* 2009;209:2128–34. doi:10.1016/j.jmatprotec.2008.05.007.
- [32] Tekkaya AE, Schikorra M, Becker D, Biermann D, Hammer N, Pantke K. Hot profile extrusion of AA-6060 aluminum chips. *Journal of Materials Processing Technology* 2009;209:3343–50. doi:10.1016/j.jmatprotec.2008.07.047.
- [33] Gronostajski J., Kaczmar J., Marciniak H, Matuszak A. Production of composites from Al and AlMg₂ alloy chips. *Journal of Materials Processing Technology* 1998;77:37–41. doi:10.1016/S0924-0136(97)00390-7.
- [34] Gronostajski JZ, Marciniak H, Matuszak A, Samuel M, Fogagnolo J. B, Ruiz-Navas E. M, et al. Recycling of aluminium alloy and aluminium matrix composite chips by pressing and hot extrusion. *Journal of Materials Processing Technology* 2003;143–144:792–5. doi:10.1016/S0924-0136(03)00380-7.

- [35] Chmura W, Gronostajski J. Mechanical and tribological properties of aluminium-base composites produced by the recycling of chips. *Journal of Materials Processing Technology* 2000;106:23–7. doi:10.1016/S0924-0136(00)00632-4.
- [36] Chmura W, Gronostajski Z. Bearing composites made from aluminium and aluminium bronze chips. *Journal of Materials Processing Technology* 2006;178:188–93. doi:10.1016/j.jmatprotec.2006.03.156.
- [37] Güley V, Ben Khalifa N, Tekkaya AE. The effect of extrusion ratio and material flow on the mechanical properties of aluminum profiles solid state recycled from 6060 aluminum alloy chips. *AIP Conference Proceedings* 2011;1353:1609–14. doi:10.1063/1.3589746.
- [38] Güley V, Ben Khalifa N, Tekkaya AE. Direct recycling of 1050 aluminum alloy scrap material mixed with 6060 aluminum alloy chips by hot extrusion. *International Journal of Material Forming* 2010;3:853–6. doi:10.1007/s12289-010-0904-z.
- [39] Ab Rahim SN, Lajis MA, Ariffin S. A review on recycling aluminum chips by hot extrusion process. *Procedia CIRP* 2015;26:761–6. doi:10.1016/j.procir.2015.01.013.
- [40] Furukawa M, Horita Z, Nemoto M, Langdon TG. Review: Processing of metals by equal-channel angular pressing. *Journal of Materials Science* 2001;36:2835–43. doi:10.1023/A:1017932417043.
- [41] Segal VM. Materials processing by simple shear. *Materials Science and Engineering A* 1995;197:157–64. doi:10.1016/0921-5093(95)09705-8.
- [42] Gudimetla K, Ramesh Kumar S, Ravisankar B, Kumaran S. Densification of Al 5083 Mechanically Alloyed Powder by Equal Channel Angular Pressing. *Transactions of the Indian Institute of Metals* 2015;68:171–6. doi:10.1007/s12666-015-0557-1.
- [43] Mani B, Jahedi M, Paydar MH. Consolidation of commercial pure aluminum powder by torsional-equal channel angular pressing (T-ECAP) at room temperature. *Powder Technology* 2012;219:1–8. doi:10.1016/j.powtec.2011.11.034.
- [44] Matsuki K, Aida T, Takeuchi T, Kusui J, Yokoe K. Microstructural characteristics and superplastic-like behavior in aluminum powder alloy consolidated by equal-channel angular pressing. *Acta Materialia* 2000;48:2625–32. doi:10.1016/S1359-6454(00)00061-6.
- [45] Kováčik J, Balog M, Emmer Š. HIP processed Cu-graphite composite transformed by ECAP. *Int. Powder Metall. Congr. Exhib. Euro PM 2013*, 2013.

- [46] Derakhshandeh. H R, Jenabali Jahromi A. An investigation on the capability of equal channel angular pressing for consolidation of aluminum and aluminum composite powder. *Materials and Design* 2011;32:3377–88. doi:10.1016/j.matdes.2011.02.015.
- [47] Haghighi RD, Jahromi SAJ, Moresedgh A, Khorshid MT. A comparison between ECAP and conventional extrusion for consolidation of aluminum metal matrix composite. *Journal of Materials Engineering and Performance* 2012;21:1885–92. doi:10.1007/s11665-011-0108-9.
- [48] Xu W, Wu X, Honma T, Ringer SP, Xia K. Nanostructured Al-Al₂O₃ composite formed in situ during consolidation of ultrafine Al particles by back pressure equal channel angular pressing. *Acta Materialia* 2009;57:4321–30. doi:10.1016/j.actamat.2009.06.010.
- [49] Haase M, Jäger A, Erman Tekkaya A. Influence of extrusion ratio on AA6060 aluminum alloy chips solid state recycled by integrated extrusion and equal channel angular pressing. *Steel Research International* 2012;SPL. ISSUE.
- [50] Haase M, Tekkaya AE. Cold extrusion of hot extruded aluminum chips. *Journal of Materials Processing Technology* 2015;217:356–67. doi:10.1016/j.jmatprotec.2014.11.028.
- [51] Misiolek WZ, Haase M, Ben Khalifa N, Tekkaya AE, Kleiner M. High quality extrudates from aluminum chips by new billet compaction and deformation routes. *CIRP Annals - Manufacturing Technology* 2012;61:239–42. doi:10.1016/j.cirp.2012.03.113.
- [52] Haase M, Ben Khalifa N, Tekkaya AE, Misiolek WZ. Improving mechanical properties of chip-based aluminum extrudates by integrated extrusion and equal channel angular pressing (iECAP). *Materials Science and Engineering: A* 2012;539:194–204. doi:10.1016/j.msea.2012.01.081.
- [53] Luo P, McDonald DT, Zhu SM, Palanisamy S, Dargusch MS, Xia K. Analysis of microstructure and strengthening in pure titanium recycled from machining chips by equal channel angular pressing using electron backscatter diffraction. *Materials Science and Engineering A* 2012;538:252–8. doi:10.1016/j.msea.2012.01.039.
- [54] McDonald DT, Davies AJ, Luo P, Zhu SM, Palanisamy S, Dargusch MS, et al. Effect of heat treatment on microstructure and mechanical properties of titanium recycled by severe plastic deformation. *Ti 2011 - Proc. 12th World Conf. Titan.*, vol. 1, 2012, p. 497–501.
- [55] Luo P, McDonald DT, Xu W, Palanisamy S, Dargusch MS, Xia K. A modified Hall-Petch relationship in ultrafine-grained titanium recycled from chips by equal channel angular pressing. *Scripta Materialia* 2012;66:785–8. doi:10.1016/j.scriptamat.2012.02.008.

- [56] Luo P, Xie H, Paladugu M, Palanisamy S, Dargusch MS, Xia K. Recycling of titanium machining chips by severe plastic deformation consolidation. *Journal of Materials Science* 2010;45:4606–12. doi:10.1007/s10853-010-4443-2.
- [57] Xia K, Wu X, Honma T, Ringer SP. Ultrafine pure aluminium through back pressure equal channel angular consolidation (BP-ECAC) of particles. *Journal of Materials Science* 2007;42:1551–60. doi:10.1007/s10853-006-0819-8.
- [58] Kang F, Liu JQ, Wang JT, Zhao X, Wu X, Xia K. The effect of back pressure on mechanical properties of an Mg-3 wt. % Al-1 wt. % Zn alloy with single pass equal channel angular pressing. *Int. J. Mater. Res.*, vol. 100, 2009, p. 1686–90. doi:10.3139/146.110238.
- [59] Kubota M, Wu X, Xu W, Xia K. Mechanical properties of bulk aluminium consolidated from mechanically milled particles by back pressure equal channel angular pressing. *Materials Science and Engineering A* 2010;527:6533–6. doi:10.1016/j.msea.2010.06.088.
- [60] Richert J, Richert M. A new method for unlimited deformation of metals and alloys. *Aluminium* 1986;62:604–7.
- [61] Richert M, Liu Q, Hansen N. Microstructural evolution over a large strain range in aluminium deformed by cyclic-extrusion-compression. *Materials Science and Engineering A* 1999;260:275–83. doi:10.1016/S0921-5093(98)00988-5.
- [62] Babaei A, Mosavi Mashadi M. Characterization of ultrafine-grained aluminum tubes processed by Tube Cyclic Extrusion-Compression (TCEC). *Materials Characterization* 2014;95:118–28. doi:10.1016/j.matchar.2014.06.013.
- [63] Chen Y, Wang Q, Lin J, Zhang L, Zhai C. Fabrication of bulk UFG magnesium alloys by cyclic extrusion compression. *Journal of Materials Science* 2007;42:7601–3. doi:10.1007/s10853-007-1889-y.
- [64] Peng T, Wang QD, Lin JB. Microstructure and mechanical properties of Mg–10Gd–2Y–0.5Zr alloy recycled by cyclic extrusion compression. *Materials Science and Engineering: A* 2009;516:23–30. doi:10.1016/j.msea.2009.04.024.
- [65] Cui J, Guo W, Roven HJ, Wang Q, Chen Y, Peng T. Recycling of aluminum scrap by Severe Plastic Deformation. vol. 667–669. 2011. doi:10.4028/www.scientific.net/MSF.667-669.1177.
- [66] Shahrom MS, Yusoff AR. Cyclic extrusion compression back pressure technique for hot forging process in direct recycling of aluminium 6061 machining chip. *Journal of Manufacturing Processes* 2017;29:1–9. doi:10.1016/j.jmapro.2017.07.003.

- [67] Wan B, Chen W, Lu T, Liu F, Jiang Z, Mao M. Review of solid state recycling of aluminum chips. *Resources, Conservation and Recycling* 2017;125:37–47. doi:10.1016/j.resconrec.2017.06.004.
- [68] Peng T, Wang Q, Lin J, Liu M, Roven HJ. Microstructure and enhanced mechanical properties of an Mg–10Gd–2Y–0.5Zr alloy processed by cyclic extrusion and compression. *Materials Science and Engineering: A* 2011;528:1143–8. doi:10.1016/j.msea.2010.09.097.
- [69] Grunschloss E. Polymer Single Screw Extrusion: Modeling. *Encycl. Mater. Sci. Technol.*, 2001, p. 7491–7504. doi:10.1016/b0-08-043152-6/01339-5.
- [70] Werenskiold JC, Auran L, Roven HJ, Ryum N, Reiso O. Screw extruder for continuous extrusion of materials with high viscosity. US12515497, 2007.
- [71] Widerøe F, Welo T. Using contrast material techniques to determine metal flow in screw extrusion of aluminium. *Journal of Materials Processing Technology* 2013;213:1007–18. doi:10.1016/j.jmatprotec.2012.11.013.
- [72] Widerøe F, Welo T, Vestøl H. A new testing machine to determine the behaviour of aluminium granulate under combined pressure and shear. *International Journal of Material Forming* 2013;6:199–208. doi:10.1007/s12289-011-1070-7.
- [73] Zhilyaev AP, Langdon TG. Using high-pressure torsion for metal processing: Fundamentals and applications. *Progress in Materials Science* 2008;53:893–979. doi:10.1016/j.pmatsci.2008.03.002.
- [74] Zhilyaev AP, McNelley TR, Langdon TG. Evolution of microstructure and microtexture in fcc metals during high-pressure torsion. *Journal of Materials Science* 2007;42:1517–28. doi:10.1007/s10853-006-0628-0.
- [75] Sakai G, Nakamura K, Horita Z, Langdon TG. Developing high-pressure torsion for use with bulk samples. *Materials Science and Engineering A* 2005;406:268–73. doi:10.1016/j.msea.2005.06.049.
- [76] Shen H, Li Z, Günther B, Korznikov A V., Valiev RZ. Influence of powder consolidation methods on the structural and thermal properties of a nanophase Cu-50wt%Ag alloy. *Nanostructured Materials* 1995;6:385–8. doi:10.1016/0965-9773(95)00077-1.
- [77] Valiev RZ, Mishral RS, Grozal J, Mukherjee AK. Processing of nanostructured nickel by severe plastic deformation consolidation of ball-milled powder. *Scripta Materialia* 1996;34:1443–8. doi:10.1016/1359-6462(95)00676-1.
- [78] Zhilyaev AP, Gimazov AA, Raab GI, Langdon TG. Using high-pressure torsion for the cold-consolidation of copper chips produced by machining. *Materials Science and Engineering A* 2008;486:123–6. doi:10.1016/j.msea.2007.08.070.

- [79] Takahashj T, Kume Y, Kobashi M, Kanetake N. Solid state recycling of aluminum machined chip wastes by compressive torsion processing. *Keikinzo*/Journal of Japan Institute of Light Metals 2009;59:354–8. doi:10.2464/jilm.59.354.
- [80] Abd El Aal MI, Yoo Yoon E, Seop Kim H. Recycling of AlSi8Cu3 alloy chips via high pressure torsion. *Materials Science and Engineering A* 2013;560:121–8. doi:10.1016/j.msea.2012.09.045.
- [81] Rashid MWA, Yacob FF, Lajis MA, Abid AMAM, Mohamad E, Ito T. A Review: The Potential of Powder Metallurgy in Recycling Aluminum Chips (Al 6061 & Al 7075). 24th Design Engineering Systems Division JSME Conference Japan Society of Mechanical Engineers 2014. doi:10.13140/2.1.2402.6887.
- [82] JENKINS I. Powder Metallurgy. *Nature* 1955;175:276–9. doi:10.1038/175276a0.
- [83] Hong SH, Kim BK. Fabrication of aluminum flake powder from foil scrap by a wet ball milling process. *Materials Letters* 2001;51:139–43. doi:10.1016/S0167-577X(01)00280-4.
- [84] Hong S-H, Lee D-W, Kim B-K. Manufacturing of aluminum flake powder from foil scrap by dry ball milling process. *Journal of Materials Processing Technology* 2000;100:105–9. doi:https://doi.org/10.1016/S0924-0136(99)00469-0.
- [85] Suśniak M, Karwan-Baczewska J, Dutkiewicz J, Actis Grande M, Rosso M. Structure investigation of ball milled composite powder based on AlSi5Cu2 alloy chips modified by SiC particles. *Archives of Metallurgy and Materials* 2013;58:437–41. doi:10.2478/amm-2013-0014.
- [86] Sherafat Z, Paydar MH, Ebrahimi R. Fabrication of Al7075/Al, two phase material, by recycling Al7075 alloy chips using powder metallurgy route. *Journal of Alloys and Compounds* 2009;487:395–9. doi:10.1016/j.jallcom.2009.07.146.
- [87] Sherafat Z, Paydar MH, Ebrahimi R, Sohrabi S. Mechanical properties and deformation behavior of Al/Al7075, two-phase material. *Journal of Alloys and Compounds* 2010;502:123–6. doi:10.1016/j.jallcom.2010.04.083.
- [88] Munir ZA, Anselmi-Tamburini U, Ohyanagi M. The effect of electric field and pressure on the synthesis and consolidation of materials: A review of the spark plasma sintering method. *Journal of Materials Science* 2006;41:763–77. doi:10.1007/s10853-006-6555-2.
- [89] Tokita M. Mechanism of Spark Plasma Sintering. *Ceramics* 2001;44:605–8. doi:10.1063/1.3622584.

- [90] Paraskevas D, Vanmeensel K, Vleugels J, Dewulf W, Duflou JR. Solid State Recycling of Aluminium Sheet Scrap by Means of Spark Plasma Sintering. *Key Engineering Materials* 2015;639:493–8. doi:10.4028/www.scientific.net/KEM.639.493.
- [91] Paraskevas D, Dadbakhsh S, Vleugels J, Vanmeensel K, Dewulf W, Duflou JR. Solid state recycling of pure Mg and AZ31 Mg machining chips via spark plasma sintering. *Materials & Design* 2016;109:520–9. doi:10.1016/j.matdes.2016.07.082.
- [92] Xu W, Wu X, Sadedin D, Xia K. Equal channel angular consolidation and deformation of titanium based alloys. *Mater. Forum*, vol. 32, 2007, p. 29–34.
- [93] Baffari D, Buffa G, Fratini L. A numerical model for Wire integrity prediction in Friction Stir Extrusion of magnesium alloys. *Journal of Materials Processing Technology* 2017;247:1–10. doi:10.1016/j.jmatprotec.2017.04.007.
- [94] Tang W, Reynolds AP. Production of wire via friction extrusion of aluminum alloy machining chips. *Journal of Materials Processing Technology* 2010;210:2231–7. doi:10.1016/j.jmatprotec.2010.08.010.
- [95] Buffa G, Campanella D, Fratini L, Micari F. AZ31 magnesium alloy recycling through friction stir extrusion process. *International Journal of Material Forming* 2016;9:613–8. doi:10.1007/s12289-015-1247-6.
- [96] McAuliffe C, Karkkainen R, Yen C, Waisman H. Numerical modeling of friction stir welded aluminum joints under high rate loading. *Finite Elements in Analysis and Design* 2014;89:8–18. doi:10.1016/j.finel.2014.04.012.
- [97] Ansari MA, Behnagh RA, Narvan M, Naeini ES, Givi MKB, Ding H. Optimization of Friction Stir Extrusion (FSE) Parameters Through Taguchi Technique. *Transactions of the Indian Institute of Metals* 2015:1–7. doi:10.1007/s12666-015-0686-6.
- [98] Behnagh RA, Shen N, Ansari MA, Narvan M, Besharati Givi MK, Ding H. Experimental Analysis and Microstructure Modeling of Friction Stir Extrusion of Magnesium Chips. *Journal of Manufacturing Science and Engineering* 2015;138:41008. doi:10.1115/1.4031281.
- [99] Zhang H, Zhao X, Deng X, Sutton MAA, Reynolds APP, McNeill SRR, et al. Investigation of material flow during friction extrusion process. *International Journal of Mechanical Sciences* 2014;85:130–41. doi:10.1016/j.ijmecsci.2014.05.011.
- [100] Zhang H, Li X, Tang W, Deng X, Reynolds AP, Sutton MA. Heat transfer modeling of the friction extrusion process. *Journal of Materials Processing Technology* 2015;221:21–30. doi:10.1016/j.jmatprotec.2015.01.032.

- [101] Baffari D, Buffa G, Campanella D, Fratini L, Reynolds AP. Process mechanics in Friction Stir Extrusion of magnesium alloys chips through experiments and numerical simulation. *Journal of Manufacturing Processes* 2017;29:41–9. doi:10.1016/j.jmapro.2017.07.010.
- [102] Buffa G, Forcellese A, Fratini L, Simoncini M. Experimental and Numerical Analysis on FSWed Magnesium Alloy Thin Sheets Obtained Using “Pin” and “Pinless” Tool. *Key Engineering Materials* 2012;504–506:747–52. doi:10.4028/www.scientific.net/KEM.504-506.747.
- [103] Chang CI, Lee CJ, Huang JC. Relationship between grain size and Zener-Holloman parameter during friction stir processing in AZ31 Mg alloys. *Scripta Materialia* 2004;51:509–14. doi:10.1016/j.scriptamat.2004.05.043.
- [104] Baffari D, Buffa G, Fratini L. Influence of Process Parameters on the Product Integrity in Friction Stir Extrusion of Magnesium Alloys. *Key Engineering Materials* 2016;716:39–48. doi:10.4028/www.scientific.net/KEM.716.39.
- [105] Buffa G, Patrinostro G, Fratini L. Using a neural network for qualitative and quantitative predictions of weld integrity in solid bonding dominated processes. *Computers & Structures* 2014;135:1–9. doi:10.1016/j.compstruc.2014.01.019.
- [106] Plata M, Piwnik J. Theoretical and Experimental Analysis of Seam Weld Formation in Hot Extrusion of Aluminum Alloys. *Seventh International Aluminum Extrusion Technology Seminar* 2000;I:205–11.
- [107] Buffa G, Pellegrino S, Fratini L. Analytical bonding criteria for joint integrity prediction in friction stir welding of aluminum alloys. *Journal of Materials Processing Technology* 2014;214:2102–11. doi:10.1016/j.jmatprotec.2014.02.014.
- [108] Baffari D, Reynolds AP, Li X, Fratini L. Influence of processing parameters and initial temper on Friction Stir Extrusion of 2050 aluminum alloy. *Journal of Manufacturing Processes* 2017;28:319–25. doi:10.1016/j.jmapro.2017.06.013.
- [109] Lequeu P, Smith KP, Daniélou A. Aluminum-copper-lithium alloy 2050 developed for medium to thick plate. *Journal of Materials Engineering and Performance* 2010;19:841–7. doi:10.1007/s11665-009-9554-z.
- [110] Li X, Tang W, Reynolds AP, Tayon WA, Brice CA. Strain and texture in friction extrusion of aluminum wire. *Journal of Materials Processing Technology* 2016;229:191–8. doi:10.1016/j.jmatprotec.2015.09.012.
- [111] Leitão C, Louro R, Rodrigues DM. Using torque sensitivity analysis in accessing Friction Stir Welding/Processing conditions. *Journal of Materials Processing Technology* 2012;212:2051–7. doi:10.1016/j.jmatprotec.2012.05.009.

- [112] Baffari D, Buffa G, Campanella D, Fratini L. Al-SiC Metal Matrix Composite production through Friction Stir Extrusion of aluminum chips. *Procedia Engineering* 2017;207:419–24. doi:10.1016/j.proeng.2017.10.798.
- [113] Ingarao G, Baffari D, Bracquene E, Fratini L, Duflou J. Energy Demand Reduction Of Aluminum Alloys Recycling Through Friction Stir Extrusion Processes Implementation. *Procedia Manufacturing* 2018;In Press.
- [114] Granta Design Limited. CES Selector 2017.
- [115] KULEUVEN, Supervisor Duflou J. Onderzoek naar het valorisatiepotentieel van smeltloze recyclageprocessen: Een economische en ecologische analyse van aluminiumrecyclage via warmextrusie en vonkplasma-sinteren. n.d.
- [116] Uriondo A, Esperon-Miguez M, Perinpanayagam S. The present and future of additive manufacturing in the aerospace sector: A review of important aspects. *Proceedings of the Institution of Mechanical Engineers, Part G: Journal of Aerospace Engineering* 2015;229:2132–47. doi:10.1177/0954410014568797.
- [117] Guo J, Zhou Y, Liu C, Wu Q, Chen X, Lu J. Wire arc additive manufacturing of AZ31 magnesium alloy: Grain refinement by adjusting pulse frequency. *Materials* 2016;9. doi:10.3390/ma9100823.
- [118] Lin JJ, Lv YH, Liu YX, Xu BS, Sun Z, Li ZG, et al. Microstructural evolution and mechanical properties of Ti-6Al-4V wall deposited by pulsed plasma arc additive manufacturing. *Materials & Design* 2016;102:30–40. doi:10.1016/j.matdes.2016.04.018.
- [119] Baffari D, Buffa G, Campanella D, Fratini L. Design of continuous Friction Stir Extrusion machines for metal chip recycling: issues and difficulties. *Procedia Manufacturing* 2018;15:280–6. doi:10.1016/j.promfg.2018.07.220.
- [120] Andrews DR, Gilpin MJ. Friction Forming - A Preliminary Study. *Metallurgist and Materials Technologist* 1975;7:355–8.
- [121] Catalini D, Kaoumi D, Reynolds AP, Grant GJ. Dispersoid Distribution and Microstructure in Fe-Cr-Al Ferritic Oxide Dispersion-Strengthened Alloy Prepared by Friction Consolidation. *Metallurgical and Materials Transactions A: Physical Metallurgy and Materials Science* 2015;46:4730–9. doi:10.1007/s11661-015-3059-1.
- [122] Catalini D, Kaoumi D, Reynolds AP, Grant GJ. Friction consolidation of MA956 powder. *Journal of Nuclear Materials* 2013;442. doi:10.1016/j.jnucmat.2012.11.054.
- [123] Li X, Baffari D, Reynolds AP. Friction stir consolidation of aluminum machining chips. *The International Journal of Advanced Manufacturing Technology* 2018;94:2031–42. doi:10.1007/s00170-017-1016-4.

- [124] Shima S, Oyane M. Plasticity theory for porous metals. *International Journal of Mechanical Sciences* 1976;18:285–91. doi:10.1016/0020-7403(76)90030-8.
- [125] Baffari D, Reynolds AP, Li X, Fratini L. Bonding prediction in friction stir consolidation of aluminum alloys: A preliminary study. *AIP Conf. Proc.*, vol. 1960, 2018. doi:10.1063/1.5034875.

Curriculum Vitae

Dario Baffari was born in Poggibonsi (Italy) on October 2nd 1991. He graduated with honours in Mechanical Engineering in 2015 from the University of Palermo and started his PhD course in the same year. He spent one year as a visiting researcher at the Department of Mechanical Engineering of the University of South Carolina (U.S.). He is currently a PhD. candidate in Innovation Technology Engineering at the University of Palermo. He is co-author of a few papers, published in peer-reviewed international journals and conference proceedings, regarding solid-state recycling and welding processes.

Publications List

Baffari D, Buffa G, Campanella D, Fratini L. Design of continuous Friction Stir Extrusion machines for metal chip recycling: issues and difficulties. *Procedia Manufacturing* 2018;15:280–6. doi:10.1016/j.promfg.2018.07.220.

Baffari D, Buffa G, Campanella D, Fratini L, Micari F. Single block 3D numerical model for linear friction welding of titanium alloy. *Science and Technology of Welding and Joining* 2018;1718:1–6. doi:10.1080/13621718.2018.1492211.

Ingarao G, Baffari D, Bracquene E, Fratini L, Duflou J. Energy Demand Reduction Of Aluminum Alloys Recycling Through Friction Stir Extrusion Processes Implementation. *Procedia Manufacturing*, 2018; In Press.

Baffari D, Reynolds AP, Li X, Fratini L. Bonding prediction in friction stir consolidation of aluminum alloys: A preliminary study. *AIP Conference Proceedings*, vol. 1960, 2018. doi:10.1063/1.5034875.

Li X, Baffari D, Reynolds AP. Friction stir consolidation of aluminum machining chips. *The International Journal of Advanced Manufacturing Technology* 2018;94:2031–42. doi:10.1007/s00170-017-1016-4.

Baffari D, Buffa G, Campanella D, Fratini L, Reynolds AP. Process mechanics in Friction Stir Extrusion of magnesium alloys chips through experiments and numerical simulation. *Journal of Manufacturing Processes* 2017;29:41–9. doi:10.1016/j.jmapro.2017.07.010.

Baffari D, Buffa G, Campanella D, Fratini L. Al-SiC Metal Matrix Composite production through Friction Stir Extrusion of aluminum chips. *Procedia Engineering* 2017;207:419–24. doi:10.1016/j.proeng.2017.10.798.

Baffari D, Reynolds AP, Li X, Fratini L. Influence of processing parameters and initial temper on Friction Stir Extrusion of 2050 aluminum alloy. *Journal of Manufacturing Processes* 2017;28:319–25. doi:10.1016/j.jmapro.2017.06.013.

Baffari D, Buffa G, Fratini L. A numerical model for Wire integrity prediction in Friction Stir Extrusion of magnesium alloys. *Journal of Material Processing Technology* 2017;247:1–10. doi:10.1016/j.jmatprotec.2017.04.007.

Baffari D, Buffa G, Fratini L. Influence of Process Parameters on the Product Integrity in Friction Stir Extrusion of Magnesium Alloys. *Key Engineering Materials* 2016;716:39–48. doi:10.4028/www.scientific.net/KEM.716.39.

Buffa G, Baffari D, Campanella D, Fratini L. An Innovative Friction Stir Welding Based Technique to Produce Dissimilar Light Alloys to Thermoplastic Matrix Composite Joints. *Procedia Manufacturing* 2016;5:319–31. doi:10.1016/j.promfg.2016.08.028.

Buffa G, Baffari D, Di Caro A, Fratini L. Friction stir welding of dissimilar aluminium– magnesium joints: Sheet mutual position effects. *Science and Technology of Welding and Joining* 2015;20:271–9. doi:10.1179/1362171815Y.0000000016.

Baffari D, Buffa G, Campanella D, Fratini L, Micari F. Friction based Solid State Welding Techniques for Transportation Industry Applications. *Procedia CIRP* 2014;18:162–7. doi:10.1016/j.procir.2014.06.125.

Baffari D, Buffa G, Ingarao G, Masnata A, Fratini L. Aluminium Sheet Metal Scrap Recycling Through Friction Consolidation. Submitted to: *Procedia Manufacturing*

Baffari D, Reynolds A R, Masnata A, Fratini L, Ingarao G. Friction Stir Extrusion To Recycle Aluminum Alloys Scraps: Energy Efficiency Characterization. Submitted to: *Journal of Manufacturing Processes*